A multipolar effective one body waveform model for spin-aligned black hole binaries.

Alessandro Nagar[1,2], Gunnar Riemenschneider[1,3], Geraint Pratten[4,5], Piero Rettegno[1,3], and Francesco Messina[6,7]
[1] *INFN Sezione di Torino, Via P. Giuria 1, 10125 Torino, Italy*
[2] *Institut des Hautes Etudes Scientifiques, 91440 Bures-sur-Yvette, France*
[3] *Dipartimento di Fisica, Università di Torino, via P. Giuria 1, 10125 Torino, Italy*
[4] *School of Physics and Astronomy and Institute for Gravitational Wave Astronomy, University of Birmingham, Edgbaston, Birmingham, B15 9TT, United Kingdom*
[5] *Departament de F´ısica, Universitat de les Illes Balears and Institut d'Estudis Espacials de Catalunya, Crta. Valldemossa km 7.5, E-07122 Palma, Spain*
[6] *Dipartimento di Fisica, Università degli studi di Milano Bicocca, Piazza della Scienza 3, 20126 Milano, Italy and*
[7] *INFN, Sezione di Milano Bicocca, Piazza della Scienza 3, 20126 Milano, Italy*

We introduce `TEOBiResumS_SM`, an improved version of the effective-one-body (EOB) waveform model `TEOBResumS` for spin-aligned, coalescing black hole binaries, that includes subdominant gravitational waveform modes completed through merger and ringdown. Beyond the dominant $(\ell, |m|) = (2, 2)$ one, the more robust multipoles all over the parameter space are: $(2, 1)$, $(3, 3)$, $(3, 2)$, $(4, 4)$ and $(5, 5)$. Modes as $(3, 1)$, $(4, 3)$ and $(4, 2)$ can also be generated, but are less robust. The multipolar ringdown EOB waveform stems from suitably fitting many numerical relativity (NR) waveform data from the Simulating eXtreme Spacetimes (SXS) collaboration together with test-mass waveform data. Mode-mixing effects are not incorporated. The orbital (nonspinning) part of the multipolar waveform amplitudes includes test-mass results up to (relative) 6PN order and, for most modes, is Padé resummed. The m=odd waveform multipoles (up to $\ell = 5$) incorporate most of the currently available spin-dependent analytical information. Each multipolar amplitude is additionally orbital-factorized and resummed. Improving on previous work, we confirm that certain $m =$ odd modes, e.g. the $(2, 1)$, and even the $(3, 1)$, may develop a zero (or a minimum) in the amplitude for nearly equal-mass binaries and for several combinations of the individual spins. A remarkable EOB/NR agreement around such zero is found for these modes. The new waveform, and radiation reaction, prompts a new NR-calibration of the spinning sector of the model, done with only 32 datasets. The maximum $(2, 2)$ EOB/NR unfaithfulness with Advanced LIGO noise against the SXS catalog (~ 473 datasets) is always below 0.5% for binaries with total mass M as $20M_\odot \leq M \leq 200M_\odot$, except for a single outlier with $\max(\bar{F}) \sim 0.7\%$. When $(2, 1)$, $(3, 3)$ and $(4, 4)$ modes are included, one finds an excellent EOB/NR agreement up to $M \sim 120M_\odot$, above which the performance degrades slightly and moves above 3% We also point out that the EOB dynamics may develop unphysical features for large, anti-aligned, spins and this may impact the correct construction of the $(2, 1)$ mode in some corners of the parameter space.

arXiv:2001.09082v1 [gr-qc] 24 Jan 2020

I. INTRODUCTION

The recent observation made by LIGO [1] and Virgo [2] of gravitational wave (GW) signals from twelve coalescing compact binaries marked the beginning of the era of gravitational wave astronomy. Of these detections, ten were associated to coalescing binary black holes (BBHs) [3–8] and two to a binary neutron star (BNS) [9, 10].

Up to recent times, gravitational waveform models used on LIGO and Virgo data only incorporated the dominant ($\ell = 2, m = 2$) mode. This may be sufficient when the binary system is highly symmetric (e.g nearly equal masses and nearly equal spins), but for binaries when one object is more massive than the other, or when the spins are very different, modeling the subdominant multipoles becomes an absolute necessity to avoid potential biases in the parameters [11, 12]. Similarly, at large inclinations, the modeling of gravitational wave modes beyond the dominant mode becomes increasingly important as higher modes are geometrically suppressed in the face-on/off limit. For this reason, there were recent efforts in building waveform models that incorporate the subdominant modes. This was the case for phenomenological models, both in the spinning [13] or nonspinning case [14], or for effective-one-body (EOB) models [15] for spin aligned black hole binaries. In addition, Ref. [16] took advantage of a huge number of high-quality numerical relativity simulations from the SXS collaboration to construct a numerical relativity (NR) surrogate model with as many modes as possible (also including the $m = 0$ ones).

Within the effective-one-body framework [17–21] for coalescing black-hole binaries, the `SEOBNRv4HM` model introduced in Ref. [15] is the higher-mode version of the `SEOBNRv4` [22] spin-aligned model, calibrated to NR simulations, while `SEOBNRv4HMP` is its precessing version [23] and represents current state of the art. Alternatively to `SEOBNRv4`, a different spin-aligned EOB model, informed by NR simulations, is `TEOBResumS`. This model was introduced in [24], and used to independently infer the parameters of GW150914 [3]. Although this waveform model is limited to the $\ell = m = 2$ dominant mode, is publicly available either as a stand-alone C code based on the

GSL library or through the LIGO `LALSuite` [25] library. One of the advantages of this model is that it implements the description of the inspiral dynamics based on the (high-order) post-adiabatic (PA) approximation [26–28]. This allows one to generate long-inspiral waveforms so efficiently to be of direct use for parameter estimation purposes (see also Ref. [29] where the same approach is applied to the `SEOBNRv4` Hamiltonian).

Recently, in a companion paper [30], hereafter Paper I, the nonspinning sector of `TEOBResumS`, was augmented with all subdominant waveform modes, completed through merger and ringdown, up to $\ell = m = 5$ included. This defined the `TEOBiResumMultipoles` model. In doing so, the EOB orbital interaction potential was improved thanks to a more stringent comparison with state-of-the-art NR simulations with small uncertainties. This led us to construct a multipolar model with EOB/NR unfaithfulness at most of the order of 2% (and typically well below 1%) for total mass up to $200M_\odot$ and mass ratio in the range $1 \leq q \leq 10$. It was also possible to verify that the model performs excellently up to $q = 18$, that is the NR dataset with the largest mass ratio currently available to us.

The purpose of the present work is to generalize the results of Paper I to the case of spin-aligned black-hole binaries. To improve the robustness of the multipolar waveform amplitudes towards merger, we build upon Refs. [31, 32], implementing the corresponding orbital factorization and resummation paradigm, though limited to the m =odd waveform modes. Together with the changes in the nonspinning part of the dynamics discussed in Paper I, this led us to a new determination of the next-to-next-to-next-to-leading (NNNLO) spin-orbit effective parameter c_3 introduced long ago [33, 34]. The construction of the multipolar waveform around the amplitude peak of each multipole (e.g. around merger), of the next-to-quasi-circular (NQC) corrections and of the postpeak-ringdown phase follows the procedure discussed, multipole by multipole, for the nonspinning case in Paper I. The only difference is that some of the NR-informed fits incorporate now a suitable spin-dependence. Ther reader should be aware that this paper stems from Refs. [24, 31, 33–37] and it is essentially the follow up of Refs. [24, 30]. As such, it adopts the same notations and conventions. For this reason, we shall assume the reader to be familiar with the notation and language of those papers, that might not be reintroduced if not absolutely necessary.

The paper is organized as follows. In Sec. II we review the elements of the EOB dynamics that remained unchanged with respect to [24] and Paper I; we discuss the structure of the new multipolar waveform and the related new determination of c_3. Section III probes the $(2, 2)$ mode all over the current release of the SXS catalog. Section IV focuses on the behavior of higher multipolar modes, highlighting several aspects related to their accurate modelization. In particular, it is pointed out, and explained, the peculiar behavior of some $m = 1$ modes. The important EOB/NR unfaithfulness computations with higher modes are also performed there. Our concluding remarks are then collected in Sec. V. The bulk of the text is complemented by several Appendixes. Appendix A specifically discusses EOB/NR comparisons with extremely long SXS waveforms; Appendix B summarizes the SXS data used in this work, either to inform the model or just to check it; and Appendix D reports all the NR-informed fits that are needed to accurately build the merger and ringdown part of the multipolar waveform.

If not otherwise specified, we use natural units with $c = G = 1$. Our notations are as follows: we denote with (m_1, m_2) the individual masses, while the mass ratio is $q \equiv m_1/m_2 \geq 1$. The total mass and symmetric mass ratio are then $M \equiv m_1 + m_2$ and $\nu = m_1 m_2/M$. We also use the mass fractions $X_{1,2} \equiv m_{1,2}/M$ and $X_{12} \equiv X_1 - X_2 = \sqrt{1 - 4\nu}$. We address with (S_1, S_2) the individual, dimensionful, spin components along the direction of the orbital angular momentum. The dimensionless spin variables are denoted as $\chi_{1,2} \equiv S_{1,2}/(m_{1,2})^2$. We also use $\tilde{a}_{1,2} \equiv X_{1,2}\chi_{1,2}$, the effective spin $\tilde{a}_0 = \tilde{a}_1 - \tilde{a}_2$ and $\tilde{a}_{12} \equiv \tilde{a}_1 - \tilde{a}_2$.

II. THE MODEL: RELATIVE DYNAMICS AND MULTIPOLAR WAVEFORM

In this Section we collect the analytical elements of `TEOBiResumS_SM` that change with respect to the original implementation of `TEOBResumS` of [24] or that stems from results of Paper I. The modifications regard all building blocks of the model: the Hamiltonian, the inspiral, EOB-resummed, waveform as well as the merger-ringdown part. However, the structure of the Hamiltonian is precisely the same of `TEOBResumS`: there is thus no need to describe it here in detail and we address the reader to Sec. II of Ref. [24]. The modifications are limited to the NR-informed effective 5PN coefficient $a_6^c(\nu)$ (that coincides with the function determined in Paper I) as well as the effective NNNLO spin-orbit parameter $c_3(\nu, \tilde{a}_1, \tilde{a}_2)$. This one needs to be redetermined, by phasing comparison with NR simulations, because of both the new $a_6^c(\nu)$, that has changed with respect to Ref. [24], and the new analytical choice for the factorized (and resummed) multipolar waveform taken from Ref. [32]. In addition, we also present here a new, spin-dependent, description of the multipolar merger and ringdown waveform, that is based on fits informed by NR simulations. These fits incorporate some, but not all, spin dependence for all modes up to $\ell = m = 5$, as we detail in Appendix D. We start by discussing the structure of the resummed waveform.

TABLE I. Resummation choices used to build our multipolar EOB waveform. The bar denotes resummation using the inverse Taylor expansion, as described by Eq. (5) of Ref. [31]. The PN-order should be intended relative to the leading-order term and also indicates the order of the additional (spinning) test-particle terms. For example, 3.5PN means that we take a polynomial of the form $1+x^{3/2}+x^2+x^{5/2}+...+x^{7/2}$, with the known ν dependence in the coefficients. Instead, 1.5^{+1}PN means that we add to the ν-dependent 1.5PN-accurate polynomial an additional term proportional to $x^{5/2}$ obtained by suitably incorporating spinning p article terms as illustrated in Sec. VB of Ref. [32]. We denote Padé resummation by P^n_d, where $N=n+d$ is the PN order.

(ℓ,m)	Resummation choices		Relative PN order	
	orbital	spin	orbital	spin
$(2,2)$	$P^5_0[\rho^{\rm orb}_{22}]$	$T[\rho^{\rm S}_{22}]$	3^{+2}PN	3.5PN without NNLO SO term
$(2,1)$	$P^5_1[\rho_{21}]$	$\hat{f}^{\rm S}_{21}=X_{12}\overline{\hat{f}^{\rm S_{(0)}}_{21}}-\frac{3}{2}\tilde{a}_{12}x^{1/2}\overline{\hat{f}^{\rm S_{(1)}}_{21}}$	3^{+3}PN	2.5PN
$(3,3)$	$P^4_2[\rho_{33}]$	$\hat{f}^{\rm S}_{33}=X_{12}\overline{\hat{f}^{\rm S_{(0)}}_{33}}+\left(-\frac{1}{4}+\frac{5}{2}\nu\right)\tilde{a}_{12}x^{3/2}\hat{f}^{\rm S_{(1)}}_{33}$	3^{+3}PN	2.5PN
$(3,2)$	$P^4_2[\rho_{32}]$	$T[\rho^{\rm S}_{32}]$	2^{+2}PN	1.5^{+1}PN (SO only)
$(3,1)$	$P^3_2[\rho^{\rm orb}_{31}]$	$\hat{f}^{\rm S}_{31}=X_{12}\overline{\hat{f}^{\rm S_{(0)}}_{31}}+\left(-\frac{9}{4}+\frac{13}{2}\nu\right)\tilde{a}_{12}x^{3/2}\hat{f}^{\rm S_{(1)}}_{31}$	3^{+2}PN	2.5PN
$(4,4)$	$P^6_0[\rho^{\rm orb}_{44}]$	$T[\rho^{\rm S}_{44}]$	2^{+4}PN	1.5^{+2}PN (SO only)
$(4,3)$	$P^4_2[\rho^{\rm orb}_{43}]$	$\hat{f}^{\rm S}_{43}=X_{12}\hat{f}^{\rm S_{(0)}}_{43}-\frac{5}{4}\tilde{a}_{12}x^{1/2}$	1^{+5}PN	0.5PN (SO only)
$(4,2)$	$P^6_0[\rho^{\rm orb}_{42}]$	$T[\rho^{\rm S}_{42}]$	2^{+4}PN	1.5^{+3}PN (SO only)
$(4,1)$	$P^4_2[\rho^{\rm orb}_{41}]$	$\hat{f}^{\rm S}_{41}=X_{12}\hat{f}^{\rm S_{(0)}}_{41}-\frac{5}{4}\tilde{a}_{12}x^{1/2}$	1^{+5}PN	0.5PN (SO only)
$(5,5)$	$P^6_0[\rho^{\rm orb}_{55}]$	$\hat{f}^{\rm S}_{55}=X_{12}\overline{\hat{f}^{\rm S_{(0)}}_{55}}+10\nu\frac{(1-3\nu)}{3-6\nu}\tilde{a}_{12}x^{3/2}$	1^{+5}PN	2PN

A. Inspiral multipolar waveform

The waveform amplitudes we use here incorporate several factorization and resummation procedures that have been discussed in previous literature [31, 32, 38, 39]. One should be warned that there are not ubiquitous recipes for what concerns the choice of resummation and/or the multipolar order to use: each multipolar amplitude can, in principle, be treated separately from the others. In practice, following Paper I, we attempt to comply at the idea of using 6PN-accurate hybrid orbital (i.e. nonspinning) amplitudes that are, whenever possible, resummed using Padé approximants. By "hybrid" we mean that the ν-dependent terms, analytically known up to 3PN accuracy, are augmented by test-particle terms up to getting a relative 6PN order in all the residual waveform amplitudes. The spin sector takes advantage of some of, but not all, the new PN information at next-to-next-to-leading-order (NNLO) that was recently presented in Ref. [15] adapting (yet unpublished) results of S. Marsat and A. Bohé. Practically all the structure of the waveform was discussed in Sec. IIIB, IIIC and IIID and of Paper I. Since we are adopting the same notation and nomenclature introduced there, it is not worth to repeat it here. We only recall that the acronym NQC stands for "next-to-quasi-circular" and that $f_{\ell m}$'s or $\rho_{\ell m}\equiv(f_{\ell m})^{1/\ell}$ functions are the residual waveform amplitudes. For resumming the $m=$ odd mode waveform amplitudes we implement the orbital-factorization and resummation scheme of Ref. [32]. In brief, following the notation of this latter reference, our analytical choices for the waveform amplitudes are listed in Table I. We give below more details, discussing explicitly, and separately, the orbital and spin sectors.

1. *Orbital sector*

All ν-dependent terms in the multipolar amplitudes up to $\ell=6$ are augmented with test-particle terms up to relative (hybrid) order 6PN *except* for the $(2,2)$ and $(3,1)$ modes, that rely on 3^{+2} PN information, consistently with previous work. For most of the modes, such 6PN-accurate, hybridized, amplitudes are additionally

Padé resummed consistently with the choice made in the extreme-mass-ratio limit in Ref. [32]. Note however that some multipoles actually behave *better* (when compared with test-mass numerical data) when they are left in non-resummed form. Table I lists, in the second column, the analytical representation chosen for the orbital factors up to $\ell = m = 5$. We address the Padé approximant of order (n, d) with the usual notation P^n_d, where n is the polynomial order of the numerator and d the one of the denominator. For notational consistency, we also indicate with P^n_0 the Taylor-expanded form of the functions. The subdominant modes that do not contain spin information are not reported in the table. The $(5, 1)$, $(6, 1)$, $\ell = 7$ and $\ell = 8$ modes are kept in Taylor-expanded form at (global) 3^{+2} PN order for simplicity, consistently with previous work. All other $\rho^{\rm orb}_{\ell m}$'s with $\ell = 5$ and $\ell = 6$ are resummed as $P^4_2\left(\rho^{\rm orb}_{\ell m}\right)$ approximants.

2. Spin sector

The spin-dependent terms in the waveform amplitudes are incorporated only in those multipoles where the ν-dependence beyond the leading order is analytically known, i.e. up to $\ell = m = 5$, as illustrated in Table I. For some modes, the ν-dependent information is augmented with spinning-particle terms, according to the hybridization procedure discussed in Ref. [32]. Note that the analytical resummation of the residual waveform amplitudes to improve their robustness in the strong-field, fast-velocity regime when $m =$ even is not the same as when $m =$ odd. For the $m =$ even modes, the residual amplitudes are written as

$$P^n_d\left[\rho^{\rm orb}_{\ell m}\right] + \rho^{\rm S}_{\ell m}, \tag{1}$$

where we explicitly indicate the fact that the orbital part is Padé resummed (including in this nomenclature also the plain Taylor-expansion) according to Table I. By contrast, the spin-dependent part is kept in Taylor-expanded form, with the (relative) PN order given in Table I. Here, the notation $T[\rho^{\rm S}_{\ell m}]$ is an explicit reminder that we are using the $\rho^{\rm S}_{\ell m}$ in Taylor-expanded form. The amount of analytical information used in each mode is listed in the fifth column of the table. First of all, note that we *do not* include the NNLO spin-orbit term in $\rho^{\rm S}_{22}$ that was recently computed and is part of either `SEOBNRv4` [22] and `SEOBNRv4HM` [15]. As it was pointed out already in Ref. [31], this term has a large impact on the EOB waveform towards merger for large, positive, spins, so that the EOB/NR difference is *larger* with this term than without it (see Fig. 6 of [31]). By contrast, the NLO-accurate amplitude alone already delivers an excellent representation of the corresponding NR amplitude and thus gives a more robust starting point for the action of the NQC factor. We do, however, include the LO cubic-in-spin term in $\rho^{\rm S}_{22}$. Browsing the fifth column of Table I the notation adopted indicates that the ν-dependent terms in $(\rho^{\rm S}_{32}, \rho^{\rm S}_{44}, \rho^{\rm S}_{42})$ were *hybridized* with some of the higher-order, spin-orbit, terms obtained in the limit of a spinning particle on a Schwarzschild black hole in Ref. [40]. The rational behind such hybridization procedure is discussed in Sec. VB of Ref. [32] and allows one to incorporate some of the leading-in-ν-dependence by suitably "dressing" the $\nu = 0$ information. One finds that the additional terms are such to increase the EOB/NR waveform ampltiude agreement towards merger in a natural way. To be explicit, we have

$$\rho^{\rm S}_{32} = c^{\rm SO_{lo}} x^{1/2} + c^{\rm SO_{nlo}}_{32} x^{3/2} + c^{\rm SO_{nnlo}}_{32} x^{5/2}, \tag{2}$$

where $(c^{\rm SO_{lo}}, c^{\rm SO_{nlo}})$ are the usual known terms with the full ν dependence (see e.g. [32] for their explicit form), while

$$c^{\rm SO_{nnlo}}_{32} = -\frac{2571199}{1924560}\tilde{a}_0 - \frac{1844993}{1924560}\tilde{a}_{12}X_{12}, \tag{3}$$

that reduces to the known spinning test-particle terms when $\nu \to 0$. Similarly, $\rho^{\rm S}_{44}$ reads

$$\rho^{\rm S}_{44} = c^{\rm SO_{lo}}_{44} x^{3/2} + c^{\rm SO_{nlo}}_{44} x^{5/2} + c^{\rm SO_{nnlo}}_{44} x^{7/2}, \tag{4}$$

where

$$c^{\rm SO_{nlo}}_{44} = -\frac{199}{550}\tilde{a}_0 - \frac{491}{550}\tilde{a}_{12}X_{12}, \tag{5}$$

$$c^{\rm SO_{nnlo}}_{44} = \frac{527001653}{264264000}\tilde{a}_0 + \frac{3208967}{264264000}\tilde{a}_{12}X_{12}, \tag{6}$$

For $\rho^{\rm S}_{42}$ we have

$$\rho^{\rm S}_{42} = c^{\rm SO_{lo}}_{42} x^{3/2} + c^{\rm SO_{nlo}}_{42} x^{5/2} + c^{\rm SO_{nnlo}}_{42} x^{7/2} + c^{\rm SO_{nnnlo}}_{42} x^{9/2}, \tag{7}$$

where the ν-dressed spinning particle coefficients read

$$c^{\rm SO_{nlo}}_{42} = -\frac{219}{550}\tilde{a}_0 + \frac{92}{275}\tilde{a}_{12}X_{12}, \tag{8}$$

$$c^{\rm SO_{nnlo}}_{42} = -\frac{329051729}{264264000}\tilde{a}_0 + \frac{169512229}{264264000}\tilde{a}_{12}X_{12}, \tag{9}$$

$$\begin{aligned} c^{\rm SO_{nnnlo}}_{42} = &-\left(\frac{32079746680643}{16482145680000} + \frac{17581}{51975}{\rm eulerlog}(x,2)\right)\tilde{a}_0 \\ &-\left(\frac{28943192016227}{16482145680000} - \frac{10697}{51975}{\rm eulerlog}(x,2)\right)\tilde{a}_{12}X_{12}. \end{aligned} \tag{10}$$

For the $m =$ odd modes, we apply in full the factorization of the orbital term and subsequent resummation of the spin factor with its inverse Taylor representation as illustrated in Ref. [32]. Recalling the notation therein, each m-odd waveform mode is written as

$$h^{(\epsilon)}_{\ell m} = h^{N,(\epsilon)'}_{\ell m}\tilde{h}^{(\epsilon)}_{\ell m}, \tag{11}$$

where $h^{N,(\epsilon)'}_{\ell m}$ is the usual Newtonian prefactor [38] with the overall factor X_{12} factorized out, while

$$\tilde{h}^{(\epsilon)}_{\ell m} \equiv X_{12}\hat{h}^{(\epsilon)}_{\ell m}, \tag{12}$$

and $\hat{h}^{(\epsilon)}_{\ell m}$ is the usual relativistic correction [38]. The m-odd relativistic waveform correction is then factorized as

$$\tilde{h}^{(\epsilon)}_{\ell m} = \hat{S}^{(\epsilon)}_{\rm eff}\hat{h}^{\rm tail}_{\ell m}e^{{\rm i}\delta_{\ell m}}\left[P^n_d\left(\rho^{\rm orb}_{\ell m}\right)\right]^{\ell}\hat{f}^{\rm S}_{\ell m}, \tag{13}$$

where $(\hat{h}^{\rm tail}_{\ell m},\delta_{\ell m})$ are the usual, well known, tail factor and residual phase correction [38]. The spin-dependent $\hat{f}^{\rm S}_{\ell m}$ functions that we use are summarized in Table I. The same table also lists the Padé approximants $P^n_d[\rho^{\rm orb}_{\ell m}]$ adopted for the orbital factors. For the spin factors, we take advantage of the new NNLO results of Ref. [15], in particular those concerning the $\ell = m = 5$ mode. This multipole is also resummed consistently with the others. In particular, it also includes the 2PN-accurate (or relative LO) spin-square term. The inverse-resummed factor $\overline{\hat{f}^{S_{(0)}}_{55}}$ explicitly reads

$$\overline{\hat{f}^{S_{(0)}}_{55}} = \left(1+\frac{10}{3}\tilde{a}_0x^{3/2}-\frac{5}{2}\tilde{a}_0^2x^2\right)^{-1}. \tag{14}$$

The global structure of the spin factors is illustrated in Table I and we do not discuss here any further as it is a straightforward application of the procedure of Ref. [32] once modified with the new PN terms published in Ref. [15] and the spinning-particle terms of Ref. [40].

3. *Residual phase corrections $\delta_{\ell m}$*

Let us finally detail the expression of the $\delta_{\ell m}$ we use. Following Ref. [41], we mostly use them in Padé resummed form, augmenting, for some modes, the 3.5PN, ν-dependent terms with the next, 4.5PN-accurate, contribution in the test-particle limit [42]. In addition, we only rely on *nonspinning* information, although spin-dependent terms are available [15]. Explicitly, the expressions we use read

$$\delta_{22} = \frac{7}{3}y^{\frac{3}{2}}\frac{808920\nu\pi\sqrt{y}+137388\pi^2y+35\nu^2\left(136080+(154975-1359276\nu)y\right)}{808920\nu\pi\sqrt{y}+137388\pi^2y+35\nu^2\left(136080+(154975+40404\nu)y\right)}, \tag{15}$$

$$\delta_{21} = \frac{2}{3}y^{\frac{3}{2}}\frac{5992\pi\sqrt{y}+2465\nu(28-493\nu y)}{69020\nu+5992\pi\sqrt{y}}, \tag{16}$$

$$\delta_{33} = \frac{13}{10}y^{\frac{3}{2}}\frac{1+\frac{94770\pi}{566279\nu}\sqrt{y}}{1+\frac{94770\pi}{566279\nu}\sqrt{y}+\frac{80897}{3159}\nu y}, \tag{17}$$

$$\delta_{32} = \frac{10+33\nu}{15(1-3\nu)}y^{\frac{3}{2}}\frac{1}{1-\frac{260(1-3\nu)}{7(10+33\nu)}\pi y^{\frac{3}{2}}+\frac{1}{(10+33\nu)^2}\left(\frac{91120}{27}+\frac{9112}{9}\nu-\frac{100232}{3}\nu^2+\frac{130000}{147}\pi^2-\frac{412880}{49}\nu\pi^2+\frac{848640}{49}\nu^2\pi^2\right)y^3}, \tag{18}$$

$$\delta_{31} = \frac{13}{30}y^{\frac{3}{2}}\frac{4641\nu+1690\pi\sqrt{y}}{4641\nu+1690\pi\sqrt{y}+18207\nu^2y}, \tag{19}$$

$$\delta_{44} = \frac{112+219\nu}{120(1-3\nu)}y^{\frac{3}{2}}\frac{1}{1-\frac{201088(1-3\nu)}{231(112+219\nu)}\pi y^{\frac{3}{2}}-\frac{1-3\nu}{(112+219\nu)^2}\left(\frac{49409024}{25}+\frac{96612288}{25}\nu+\frac{8854306816}{17787}\pi^2-\frac{49478908928}{17787}\nu\pi^2\right)y^3}, \tag{20}$$

$$\delta_{43} = \frac{486+4961\nu}{810(1-2\nu)}y^{\frac{3}{2}}\left[1-\frac{254502(1-2\nu)}{77(486+4961\nu)}\pi y^{\frac{3}{2}}+\frac{1}{(486+4961\nu)^2}\Big(\frac{122106771}{5}+\frac{2004460533}{10}\nu+\right. \tag{21}$$
$$\left.-\frac{2492887617}{5}\nu^2+\frac{45723320316}{5929}\pi^2-\frac{415427177628}{5929}\nu\pi^2+\frac{647961073992}{5929}\nu^2\pi^2\Big)y^3\right]^{-1},$$

$$\delta_{42} = \frac{7(1+6\nu)}{15(1-3\nu)}y^{\frac{3}{2}}\frac{1}{1-\frac{6284(1-3\nu)}{1617(1+6\nu)}\pi y^{\frac{3}{2}}+\frac{1-3\nu}{(1+6\nu)^2}\left(\frac{6893}{175}+\frac{41358}{175}\nu+\frac{8646784}{871563}\pi^2-\frac{22195088}{290521}\nu\pi^2\right)y^3}, \tag{22}$$

$$\delta_{41} = \frac{2+507\nu}{10(1-2\nu)}y^{\frac{3}{2}}+\frac{1571}{3465}\pi^3y^3, \tag{23}$$

$$\delta_{55} = \frac{96875+857528\nu}{131250(1-2\nu)}y^{\frac{3}{2}}, \tag{24}$$

where $y = \hat{H}_{\rm EOB}\Omega$, with $\hat{H}_{\rm EOB}$ and Ω being the energy and orbital frequency of the binary system respectively. For completeness, let us also list the original Taylor expanded functions that are then resummed using the Padé approximants explicitly written above.

$$\delta_{22}^{\rm Taylor} = \frac{7}{3}y^{\frac{3}{2}} - 24\nu y^{\frac{5}{2}} + \frac{428}{105}\pi y^3 + \left(\frac{30995}{42} + \frac{962}{5}\nu\right)\frac{\nu}{27}y^{\frac{7}{2}}, \tag{25}$$

$$\delta_{21}^{\rm Taylor} = \frac{2}{3}y^{\frac{3}{2}} - \frac{493}{42}\nu y^{\frac{5}{2}} + \frac{107}{105}\pi y^3, \tag{26}$$

$$\delta_{33}^{\rm Taylor} = \frac{13}{10}y^{\frac{3}{2}} - \frac{80897}{2430}\nu y^{\frac{5}{2}} + \frac{39}{7}\pi y^3 \ , \tag{27}$$

$$\delta_{31}^{\rm Taylor} = \frac{13}{30}y^{\frac{3}{2}} - \frac{17}{10}\nu y^{\frac{5}{2}} + \frac{13}{21}\pi y^3 \ , \tag{28}$$

$$\delta_{32}^{\rm Taylor} = \frac{10+33\nu}{15(1-3\nu)}y^{\frac{3}{2}} + \frac{52}{21}\pi y^3 + \left(\frac{208}{63}\pi^2 - \frac{9112}{405}\right)y^{9/2} \ , \tag{29}$$

$$\delta_{44}^{\rm Taylor} = \frac{112+219\nu}{120\,(1-3\nu)}y^{\frac{3}{2}} + \frac{25136}{3465}\pi y^3 + \left(\frac{201088}{10395}\pi^2 - \frac{55144}{375}\right)y^{9/2}, \tag{30}$$

$$\delta_{43}^{\rm Taylor} = \frac{486+4961\nu}{810(1-2\nu)}y^{3/2} + \frac{1571}{385}\pi y^3 + \left(-\frac{18611}{300} + \frac{3142}{385}\pi^2\right)y^{9/2}, \tag{31}$$

$$\delta_{42}^{\rm Taylor} = \frac{7(1+6\nu)}{15(1-3\nu)}y^{3/2} + \frac{6284}{3465}\pi y^3 + \left(\frac{25136}{10395}\pi^2 - \frac{6893}{375}\right)y^{9/2} \ . \tag{32}$$

Comparing with Appendix D of Ref. [41], we are here explicitly using 4.5PN terms in some of the higher modes, since we found that they improve the EOB/NR frequency agreement close to merger. In practice, after factorizing the leading contribution following [41] , the approximants we use for each mode are: $\delta_{22} \to P_2^2$; $\delta_{21} \to P_1^2$; $\delta_{33} \to P_2^1$; $\delta_{32} \to P_2^0$; $\delta_{31} \to P_2^1$; $\delta_{44} \to P_2^0$ and $\delta_{43} \to P_2^0$.

B. Multipolar peak, ringdown and next-to-quasi-circular corrections

The modelization of the peak and postpeak waveform multipole by multipole is done following precisely the same procedure adopted in the nonspinning case, but incorporating spin dependence (whenever possible) in all fits. As we detail in Appendix D, in practice we include: (i) complete spin-dependence for what concerns peak quantities and postpeak fits in all $\ell = m$ modes up to $\ell = 5$; (ii) modes like $(2,1)$, $(3,2)$, $(4,3)$ and $(4,2)$ include spin dependence for peak frequency and amplitude, but they adopt the simpler nonspinning fits for the parameters entering the postpeak waveform description; (iii) the $(3,1)$ and $(4,1)$ mode only rely on nonspinning information. The values at the NQC determination points are either obtained with dedicated fits of the corresponding NR quantities, or directly from the postpeak behavior. All considered, this approach allows one to obtain a rather robust description of the ringdown waveform all over the parameter space.

C. NR-informed EOB functions: a_6^c and c_3

Finally, we discuss the NR-informed functions that enter the EOB dynamics. For $a_6^c(\nu)$, we use the function determined in Paper I. Note that this was obtained using the Padé resummed $P_2^4[\rho_{22}^{\rm orb}]$ description of the residual $\ell = m = 2$ waveform amplitude hybridized with test-particle terms up to 6PN. For simplicity, we adopt it here *even if* we are here using $\rho_{22}^{\rm orb}$ at 3^{+2} PN accuracy. The differences in the dynamics, at the nonspinning level, are consistent with the NR uncertainty, so it is not worth to proceed with a new, more consistent, determination of this function. The expression adopted from Paper I is

$$a_6^c = n_0\frac{1+n_1\nu+n_2\nu^2+n_3\nu^3}{1+d_1\nu}, \tag{33}$$

where

$$n_0 = 5.9951, \tag{34}$$
$$n_1 = -34.4844, \tag{35}$$
$$n_2 = -79.2997, \tag{36}$$
$$n_3 = 713.4451, \tag{37}$$
$$d_1 = -3.167. \tag{38}$$

This, together with the new analytical description of the spin-sector of the waveform (and radiation reaction) calls for a new determination of c_3. This is obtained precisely following Sec. IIB.2 of Ref. [24], i.e. by determining the good values of c_3 such that the EOB/NR dephasing is within the nominal NR phase uncertainty at NR merger. This is done using 32 NR datasets, 30 from SXS and 2 from the BAM code. The configurations used are listed in Table II, together with the value of c_3 that assures an EOB/NR phasing at merger that is smaller than (or comparable with) the nominal numerical uncertainty (see [24]. Note also that these values are such to assure that the EOB frequency evolution towards merger is correctly reproducing the corresponding NR one. The data of Table II are fitted with a global function as $c_3(\nu, \tilde{a}_0, \tilde{a}_{12})$ that is actually simplified with respect to previous work. The fit template reads

$$c_3(\tilde{a}_1,\tilde{a}_2,\nu) = p_0\frac{1+n_1\tilde{a}_0+n_2\tilde{a}_0^2+n_3\tilde{a}_0^3+n_4\tilde{a}_0^4}{1+d_1\tilde{a}_0} + p_1\tilde{a}_0\nu\sqrt{1-4\nu} + p_2\left(\tilde{a}_1-\tilde{a}_2\right)\nu^2, \tag{39}$$

TABLE II. Binary configurations, first-guess values of c_3 used to inform the global interpolating fit given in Eq. (39), and the corresponding $c_3^{\rm fit}$ values.

#	ID	(q,χ_1,χ_2)	$c_3^{\rm first\ guess}$	$c_3^{\rm fit}$
1	SXS:BBH:0156	$(1,-0.95,-0.95)$	88	87.87
2	SXS:BBH:0159	$(1,-0.90,-0.90)$	85.5	85.54
3	SXS:BBH:0154	$(1,-0.80,-0.80)$	81	80.90
4	SXS:BBH:0215	$(1,-0.60,-0.60)$	71.5	71.72
5	SXS:BBH:0150	$(1,+0.20,+0.20)$	38.0	36.92
6	SXS:BBH:0228	$(1,+0.60,+0.60)$	22.0	21.94
7	SXS:BBH:0230	$(1,+0.80,+0.80)$	15.5	16.25
8	SXS:BBH:0153	$(1,+0.85,+0.85)$	14.5	15.25
9	SXS:BBH:0160	$(1,+0.90,+0.90)$	14.9	14.53
10	SXS:BBH:0157	$(1,+0.95,+0.95)$	14.3	14.20
11	SXS:BBH:0177	$(1,+0.99,+0.99)$	14.2	14.32
12	SXS:BBH:0004	$(1,-0.50,0)$	54.5	56.61
13	SXS:BBH:0231	$(1,+0.90,0)$	27.0	26.18
14	SXS:BBH:0232	$(1,+0.90,+0.50)$	19.0	18.38
15	SXS:BBH:0005	$(1,+0.50,0)$	34.3	34.34
16	SXS:BBH:0016	$(1.5,-0.50,0)$	57.0	58.19
17	SXS:BBH:0255	$(2,+0.60,0)$	29.0	29.75
18	SXS:BBH:0256	$(2,+0.60,+0.60)$	22.8	23.68
19	SXS:BBH:0257	$(2,+0.85,+0.85)$	15.7	17.73
20	SXS:BBH:0036	$(3,-0.50,0)$	60.0	60.39
21	SXS:BBH:0267	$(3,-0.50,-0.50)$	69.5	65.28
22	SXS:BBH:0174	$(3,+0.50,0)$	30.0	31.20
23	SXS:BBH:0286	$(3,+0.50,+0.50)$	26.0	27.28
24	SXS:BBH:0291	$(3,+0.60,+0.60)$	23.4	24.22
25	SXS:BBH:0293	$(3,+0.85,+0.85)$	16.2	18.48
26	SXS:BBH:0060	$(5,-0.50,0)$	62.0	61.91
27	SXS:BBH:0110	$(5,+0.50,0)$	31.0	29.97
28	SXS:BBH:1375	$(8,-0.90,0)$	64.0	78.27
29	SXS:BBH:0064	$(8,-0.50,0)$	57.0	63.23
30	SXS:BBH:0065	$(8,+0.50,0)$	28.5	28.86
31	BAM	$(8,+0.80,0)$	24.5	20.85
32	BAM	$(8,+0.85,+0.85)$	16.3	18.11

where the parameters are

$$p_0 = \ \ 45.235903, \tag{40}$$
$$n_1 = -1.688708, \tag{41}$$
$$n_2 = \ \ 0.787959, \tag{42}$$
$$n_3 = -0.018080, \tag{43}$$
$$n_4 = -0.001906, \tag{44}$$
$$d_1 = -0.751479, \tag{45}$$
$$p_1 = \ \ 47.3756, \tag{46}$$
$$p_2 = -36.1964. \tag{47}$$

Figure 1 highlights that the span of the "best" (first-guess) values of c_3 is rather limited (especially for positively aligned spins) around the equal-mass, equal-spin case. At a practical level, this eases up the fitting procedure, that, following Ref. [24], is performed in two steps. First, one fits the equal-mass, equal-spin data with a quasi-linear function of $\tilde{a}_0 = \tilde{a}_1 + \tilde{a}_2$ with $\tilde{a}_1 = \tilde{a}_2$. This delivers the six parameters $(p_0, n_1, n_2, n_3, n_4, d_1)$. Note that the analytical structure of the fitting function was chosen in order to accurately capture the nonlinear behavior of c_3 for $\tilde{a}_0 \to 1$. In the second step one subtracts this fit, computed for the unequal-mass, unequal-spin data, from the corresponding $c_3^{\rm first-guess}$ values and fits the residual. This gives the parameters (p_1, p_2). The novelty with respect to Ref. [24] is that, thanks to the new analytical improvements, one finds that the unequal-spin and unequal-mass correction can be represented, in Eq. (39), with acceptable accuracy, only with the two parameters (p_1, p_2), as we shall illustrate quantitatively below.

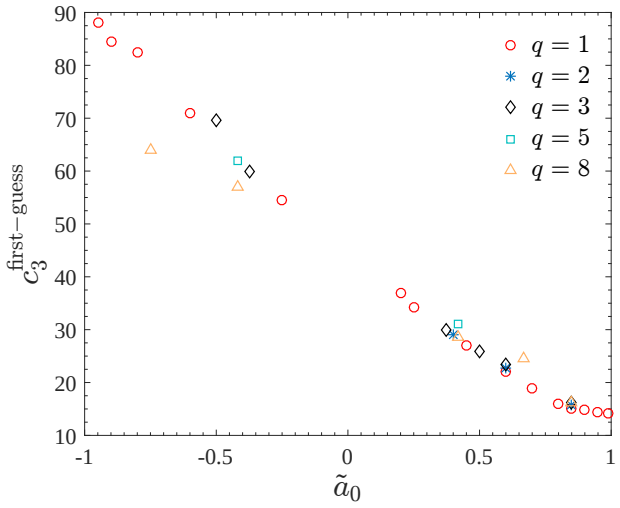

FIG. 1. The first-guess c_3 values of Table II versus the spin variable $\tilde{a}_0 \equiv S_1/(m_1 M) + S_2/(m_2 M)$. The unequal-spin and unequal-mass points can be essentially seen as a correction to the equal-mass, equal-spin values.

III. THE $\ell = m = 2$ MODE: EOB/NR UNFAITHFULNESS

We start discussing the performance of the model in terms of EOB/NR unfaithfulnesses plots for the $\ell = m = 2$ mode. The EOB/NR unfaithfulness (as function of the total mass M of the binary) is defined as

$$\bar{F}(M) \equiv 1 - F = 1 - \max_{t_0,\phi_0} \frac{\langle h_{22}^{\rm EOB}, h_{22}^{\rm NR}\rangle}{||h_{22}^{\rm EOB}||||h_{22}^{\rm NR}||}, \tag{48}$$

where (t_0, ϕ_0) are the initial time and phase, $||h|| \equiv \sqrt{\langle h, h\rangle}$, and the inner product between two waveforms is defined as $\langle h_1, h_2\rangle \equiv 4\Re \int_{f_{\rm min}^{\rm NR}(M)}^{\infty} \tilde{h}_1(f)\tilde{h}_2^*(f)/S_n(f)\, df$,

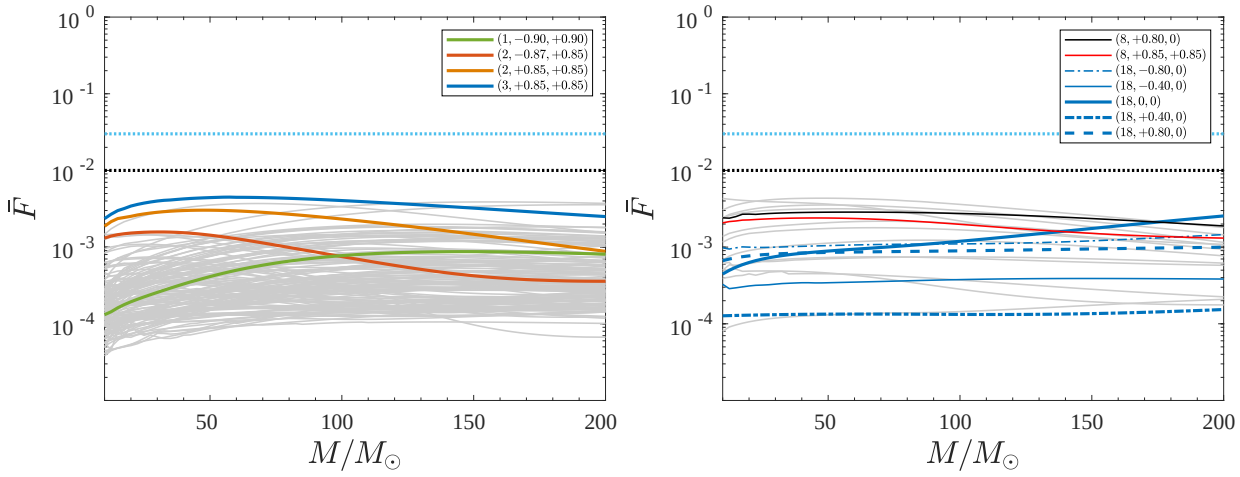

FIG. 2. EOB/NR unfaithfulness, Eq. (48), for the $\ell = m = 2$ mode. Left panel: computation using SXS waveforms publicly released before February 3, 2019. Right panel: same computation done with BAM waveform data. A subset of all this data is used to inform the (a_6^c, c_3) EOB functions. Comparison with Figs. 1 and 3 of Ref. [24] allows to appreciate the improvement with respect to the original implementation of `TEOBResumS`.

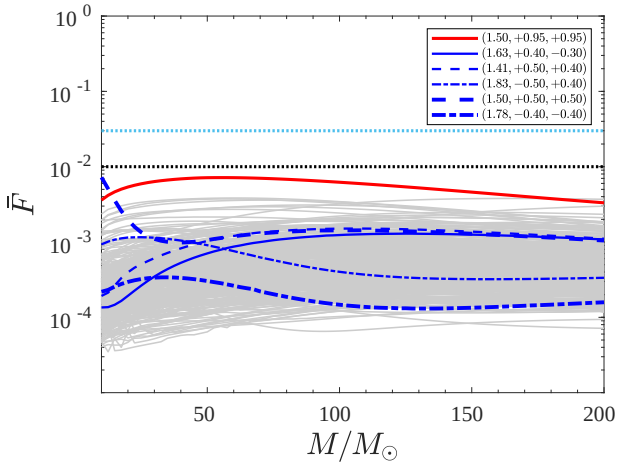

FIG. 3. EOB/NR $\ell = m = 2$ unfaithfulness computation with SXS waveform data publicly released after February 3, 2019. None of these datasets was used to inform the model, in the dynamical EOB functions (a_6^c, c_3), though several were used for the postmerger waveform part. It is remarkable that $\max(\bar{F})$ is always below 0.4% except for two outliers (one in red and one in dashed thick blue online), that however never exceed 0.7%. The plot includes five exceptionally long waveforms, each one developing more than 139 GW cycles before merger, SXS:BBH:1412, 1413, 1414, 1415 and 1416, that are depicted in blue. The function $\bar{F}$ for $(1.50, +0.50, +0.50)$, labeled as SXS:BBH:1415, shows a rather unusual behavior for low masses. See Fig. 4 and related text for discussion.

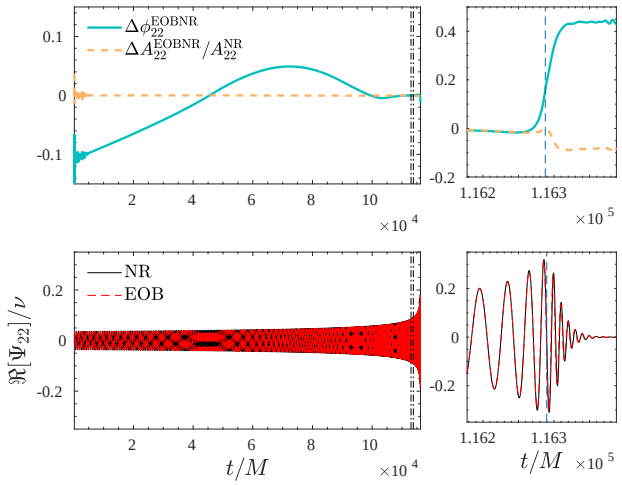

FIG. 4. EOB/NR phasing comparison for SXS:BBH:1415, $(1.5, +0.5, +0.5)$. Note that it doesn't seem possible to flatten the phase difference up to $t/M \simeq 1 \times 10^5$. The vertical lines indicate the alignment frequency region $[M\omega_L, M\omega_R] = [0.038, 0.042]$. This explains the corresponding behavior of $\bar{F}$ in Fig. 3 and suggests that the waveform behavior might be influenced by some systematic effect plaguing the NR data.

where $\tilde{h}(f)$ denotes the Fourier transform of $h(t)$, $S_n(f)$ is the zero-detuned, high-power noise spectral density of Advanced LIGO [43] and $f_{\rm min}^{\rm NR}(M) = \hat{f}_{\rm min}^{\rm NR}/M$ is the *starting frequency of the NR waveform* (after the junk radiation initial transient). Both EOB and NR waveforms are tapered in the time-domain so as to reduce high-frequency oscillations in the corresponding Fourier transforms. Figure 2 illustrates $\bar{F}$ versus M evaluated over the same NR waveform data used in Ref. [24], with the SXS data in the left panel and the BAM data in the right panel. As mentioned above, a subset of this data, listed in Table II, (both SXS and BAM) was used to inform the $c_3(\nu, \tilde{a}_1, \tilde{a}_2)$ function. The global performance of the model is largely improved with respect to Ref. [24]

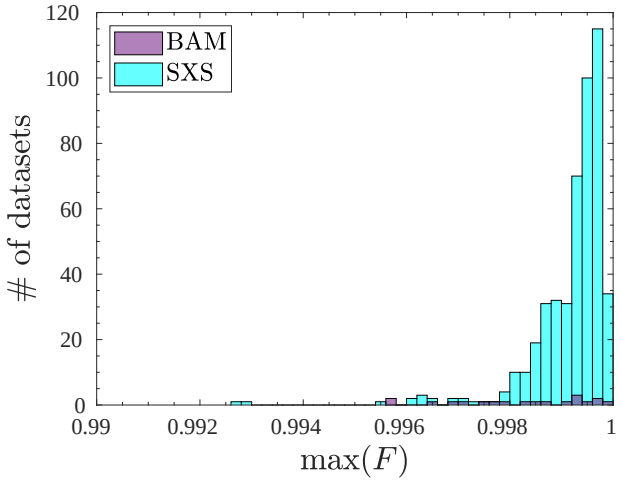

FIG. 5. Maximal EOB/NR faithfulness F, Eq. (48), all over the SXS (473) and BAM (19) NR simulations considered. Note that this plot incorporates 338 new SXS waveforms that were not included in Fig. 6 of [24].

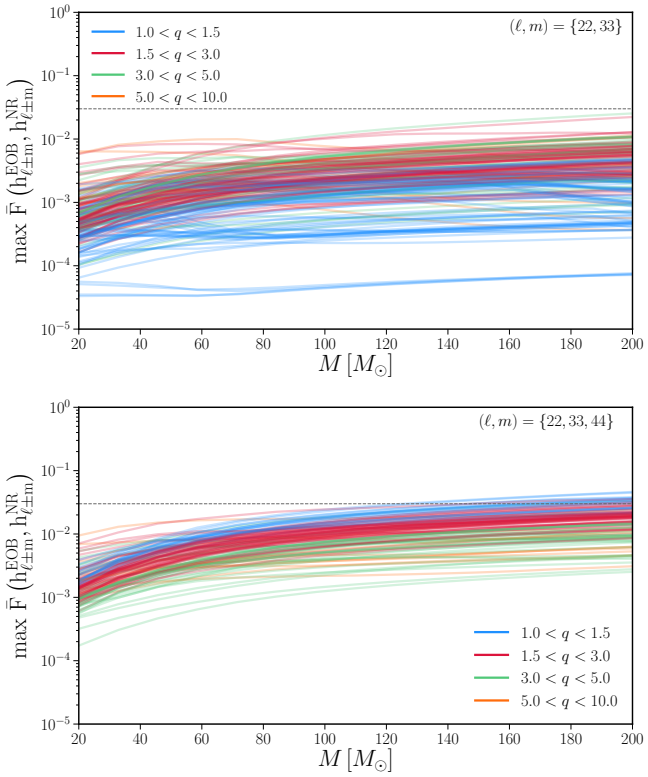

FIG. 6. EOB/NR unfaithfulness computation putting together all $\ell = m$ modes up to $\ell = 4$. Plotted is the worst-case performance maximing the unfaithfulness over the sky, Eq.(49). The worst-case mismatches arise from near edge-on configurations, when the power emitted in the $(2, 2)$ mode is minimized.

(see Fig. 1 there[1]. Remarkably, the model performs excellently also for large mass ratios and large spins, without any outlier above the 1% threshold, but $\max(\bar{F}) \lesssim 0.5\%$ all over.

After February 3, the SXS collaboration publicly released another 338 new simulations at an improved accuracy[2]. This part of the catalog mostly covers the same region of parameter space of the previous data, except for a few waveforms spanning mass ratios between 4 and 8, with spins higher than what considered before. The catalog also includes a few extremely long waveforms, with more than 100 orbits. As an additional cross check of the robustness and accuracy of our model, we compute $\bar{F}$ all over this new set of NR waveforms. The result is displayed in Fig. 3. We find that $\max(\bar{F})$ always remains *below* 0.7%, with actually only one outlier, $(1.5, +0.95, +0.95)$ `SXS:BBH:1146`[3], above 0.4%. This is not surprising since the set of NR waveforms used to inform c_3 does not cover, except for one single simulation, the part of the parameter space with $1 < q < 2$. Yet, this results highlights the robustness of our model: without any additional input from NR simulations to determine c_3, it is able to deliver rather accurate waveforms even in a region of the parameter space previously not covered by NR data. The model performance is summarized in Fig. 5, with an histogram showing all the maximum values of the *faithfulness*, $\max(F)$, from Figs. 2 and 3. Thanks to the additional analytical information incorporated and to the improved waveform resummation, `TEOBiResumS_SM` is currently the EOB model that exhibits the highest EOB/NR faithfulness for the $\ell = m = 2$ mode.

IV. HIGHER MULTIPOLAR MODES

A. Multipoles $(2, 2)$, $(3, 3)$ and $(4, 4)$

Let us move now to discussing the quality of the higher modes. For illustrative purposes, we consider explicitly four configurations with $q = 3$, with equal spins, both aligned or anti-aligned to the orbital angu-

[1] In this respect, it is interesting to note that $\bar{F}$ for $(2, +0.85, +0.85)$ is now around the 10^{-3} level, while in Fig. 1 of [24] is around 10^{-4}. This happens because the difference between $c_3^{\rm fit}$ and $c_3^{\rm first-guess}$ is now larger than what it was in [24], see Table I there. A priori, a more flexible fitting function for c_3 would allow one to obtain even smaller values of $\bar{F}$. Since the EOB/NR performance of the model is already rather good, we content ourselves of the current, simple, analytical representation of c_3.

[2] There are also 6 more, very long (> 100 GW cycles) simulations that we do not include here due to possible systematics, as we discuss in Appendix A.

[3] We excluded `SXS:BBH:1415` $(1.5, +0.50, +0.50)$ from this list. Computing the mismatch between the two highest levels of resolution publicly available one finds a large uncertainty for low masses. For further discussion see Appendix A.

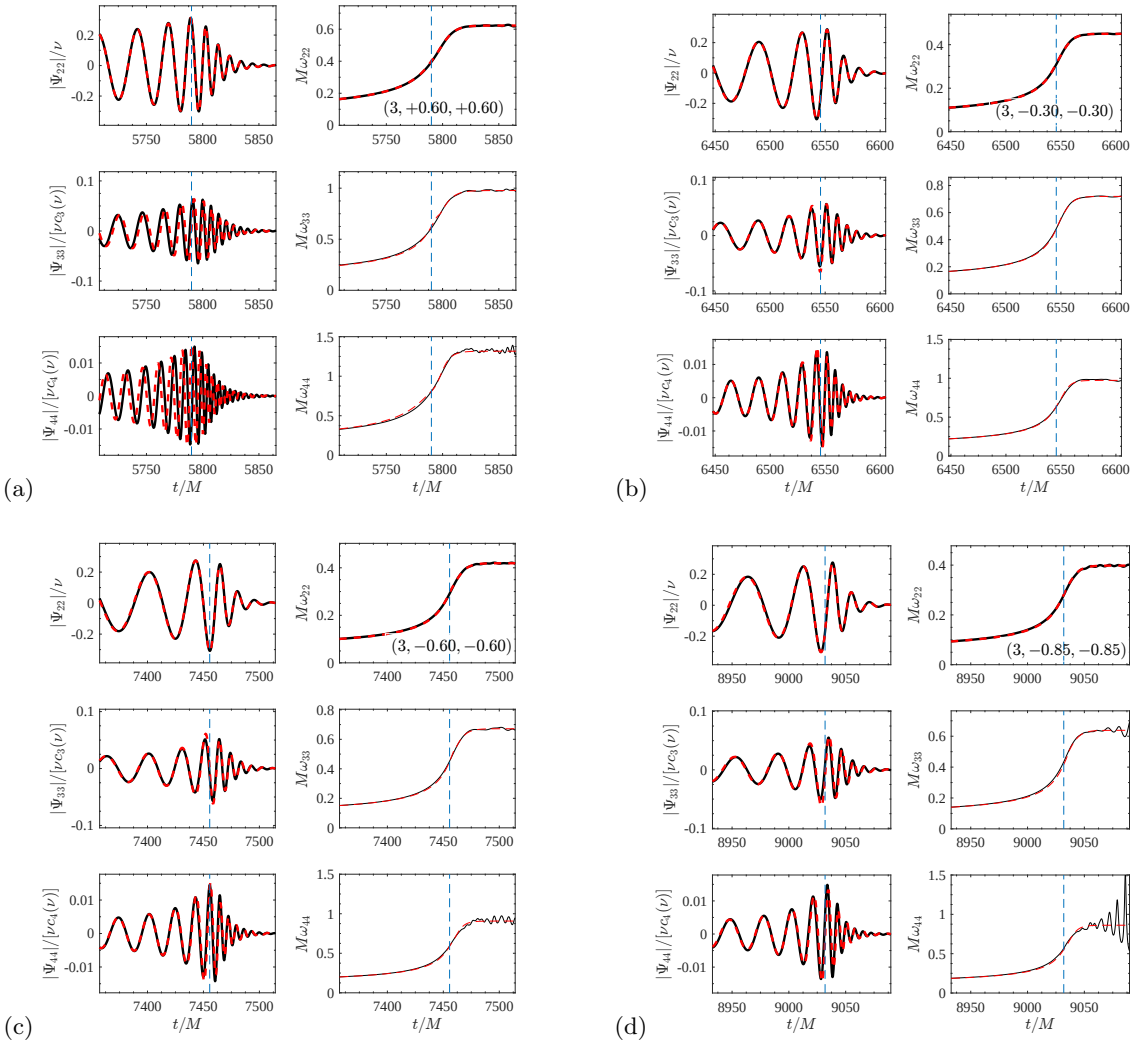

FIG. 7. Behavior of $(2,2)$, $(3,3)$ and $(4,4)$ modes for a few, illustrative, spin-aligned configurations with $q = 3$: comparing NR (black) with EOB (red) waveform. Each panel plots the real part (left columns) and the instantaneous frequency (right columns).

lar momentum. More precisely, we use $(3, -0.85, -0.85)$, $(3, -0.60, -0.60)$, $(3.-0.30, -0.30)$ and $(3, +0.60, +0.60)$. The qualitative (and quantitative) behavior discussed here for this configuration is general enough to be considered paradigmatic all over the SXS waveform catalog. Figure 7 illustrates the behavior of the $(2,2)$, $(3,3)$ and $(4,4)$ mode. For each multipoles, we show the real part of the EOB/NR waveforms together with the instantaneous GW frequency $\omega_{\ell m}$. The EOB waveform is aligned to the NR one around merger, so to highlight the excellent EOB/NR agreement there. The EOB/NR agreement is rather good either for spins both anti-aligned or aligned with the orbital angular momentum. We should, however, mention that when the spins are large and aligned there is an increasing dephasing accumulating between the EOB and NR $(4,4)$ mode, as one can see in Fig. 7 (a). As it was the case for the $\ell = m = 2$ mode discussed above, a global understanding of the actual performance of the model comes from EOB/NR unfaithfulness computations. In addition to Eq. (48), due to the non-trivial angular dependence introduced by the subdominant spherical harmonics, we consider the worst-case performance of the model by maximizing the unfaithfulness over the sky

$$\max\ \bar{F}(h_1, h_2) \equiv \max_{\theta,\phi}\ \bar{F}(h_1, h_2). \tag{49}$$

In Fig. 6, we show the worst case performance for the $\ell = m$ modes up to $\ell = 4$, finding excellent agreement up to $\sim 120 M_\odot$ above which the model performance degrades slightly and moves above 3%. In all cases, the worst case mismatches arise from near edge-on configurations, where the power in the (2,2)-mode is minimized. The worst mismatches occur for mass ratios $1 \leq q \leq 1.5$ and equal-spin configurations, in which the approximate symmetry of the binary leads to a suppression of odd-m

modes. For these binaries, the degraded performance will be driven by the accuracy of the $(4,4)$ mode in both the EOB model and the underlying NR data itself.

B. Other subdominant multipoles

1. *Multipoles* $(2,1)$, $(3,2)$ *and* $(5,5)$

Let us discuss now modes $(2,1)$, $(3,2)$ and $(5,5)$, that can be robustly constructed over most (but crucially not all) the parameter space. To illustrate the typical behavior, we consider the same BBH configurations show in Fig. 7, but we focus now on amplitude and frequency. Each panel of the figure compares four curves: the NR one (black), the analytical EOB waveform (orange), the NQC-corrected EOB waveform (light-blue) and the complete EOB waveform that includes the ringdown part. In addition, on the $(2,1)$ frequency we also superpose the EOB orbital frequency, as a grey line. The blue, dashed, vertical lines in the plot mark the location of the merger point, i.e. the peak of the $(2,2)$ waveform amplitude. A few considerations first on the NR waveforms: during the ringdown, one clearly sees in the $(2,1)$ and $(3,2)$ the effect of mode mixing, that shows up as amplitude modulations and frequency oscillations. The origin of these features has been explained in details in Ref. [44]. By contrast, the $(5,5)$ mode shows features that clearly highlight some lack of accuracy in the NR data. This is more evident in both $(3,-0.60,-0.60)$ and $(3,-0.85,-0.85)$ configurations (see bottom rows of the (c) and (d) panels of Fig. 8. Let us focus first on the $(3,2)$ mode. Despite the absence of mode-mixing, the complete EOB waveform qualitatively reproduces the behavior of the NR one around peak and postpeak, especially for what concerns the amplitude. By contrast, the ringdown frequency, i.e. in the postpeak regime, is flat and *systematically larger* than the NR one because of lack of the physical information in the ringdown modelization. It is however interesting to note that the approximation is more reliable for large, anti-aligned, spins. Similarly, the shape of the waveform entailed by the action of the NQC is rather accurate and yields a reliable approximation of the frequency behavior up to merger. By contrast, the situation is different for the $(2,1)$ mode. When spins are aligned with the angular momentum, the standard procedure for improving the behavior of the merger waveform via NQC and the ringdown attachment works well, consistently with the nonspinning case discussed in Ref. [30]. This is clear for the case $(3,+0.60,+0.60)$ of Fig 8 and the procedure remains robust at least up to $(3,-0.30,-0.30)$ as the figure illustrates. By contrast, as the magnitude of the anti-aligned spins increase, the NQC correction becomes progressively inaccurate and the resulting waveform becomes incompatible with the NR ones. This is for example the case for $(3,-0.85,-0.85)$, where the NQC correction is unable to act so as to smoothly connect the inspiral, plunge and merger waveform to the ringdown (postmerger) part. This latter is, by contrast, reliable, except for the mode-mixing oscillation, that is missing by construction. We tracked the reason of the unphysical behavior of the NQC correction as follows. In our approach, that is the same of the nonspinning case, Paper I, the NR information used to determine the NQC parameters is extracted $2M$ after the $(2,1)$ peak. As a consequence, for a successful implementation, the NQC factor should be evaluated there. Unfortunately, the EOB dynamics in this region, that is *after* merger time (i.e. the peak of the $(2,2)$ mode), may develop unphysical features depending on the values of the spins. The simplest way to explain what is going on is by looking at the orbital frequency, Ω. This is shown as a grey line in the $(2,1)$ panels of Fig. 8. One sees that for both $(3,-0.60,-0.60)$ and $(3,-0.85,-0.85)$ Ω becomes very small around the peak of the $(2,1)$ mode until it crosses zero and becomes negative. This is unexpected for this configuration and not what it is supposed to be. The unphysical character of this feature can be understood by qualitative comparison with the system made by a point-particle inspiralling and plunging on a Kerr black hole. In this case, the orbital frequency changes sign for configurations where the spin of the black hole is antialigned with the orbital angular momentum and large: the frame dragging exerted by the black-hole space time on the particle is responsible of the sign change in the frequency (see e.g. Ref. [45]). One should be aware that such dynamical behavior reflects on the waveform, and in particular on the QNMs frequency excitations, notably also at the level of the $(2,2)$ mode, that should have a zero at the time when the angular velocity of the particle changes sign (i.e., from counterrotation with respect to the black hole, to rotating with the black hole). Such qualitative features are not present in the NR waveform, so we believe that the EOB frequency behavior for this configuration is incorrect after merger time. This suggests that the current Hamiltonian should be modified so to avoid this feature. At a practical level, the fact that Ω crosses zero when the values of the relative separation r is small, but finite, implies that the NQC functions $n_4 \equiv p_{r_*}/(r\Omega)$ and $n_5 \equiv p_{r_*}/(r\Omega)\Omega^{2/3}$ (see Paper I) become very large and prevent the related NQC correction to the phase to act efficiently so to correctly modify the bare inspiral waveform. This is is evident in panel (c) and (d) of Fig. 8. This problem affects the $(2,1)$ for any mass ratio when the anti-aligned spin(s) are sufficiently large. For example, a similar behavior is found also for $(8,-0.90,0)$. As a consequence, to use the current multipolar model for actual parameter estimation studies, it will be necessary to determine the precise region of the parameter space where the $(2,1)$ mode is reliable. Selecting only those datasets with $\chi_i > -0.4$, Fig. 9 shows the EOB/NR unfaithfulness, maximized over the sky, when including modes $(2,2)$, $(2,1)$ and $(3,3$. Further improvement, as well as the determination of the precise range of reliability of the $(2,1)$ mode through merger and ringdown, are postponed to future work. Here we will just briefly explore, in Sec. IV B 3 below, a possible modifica-

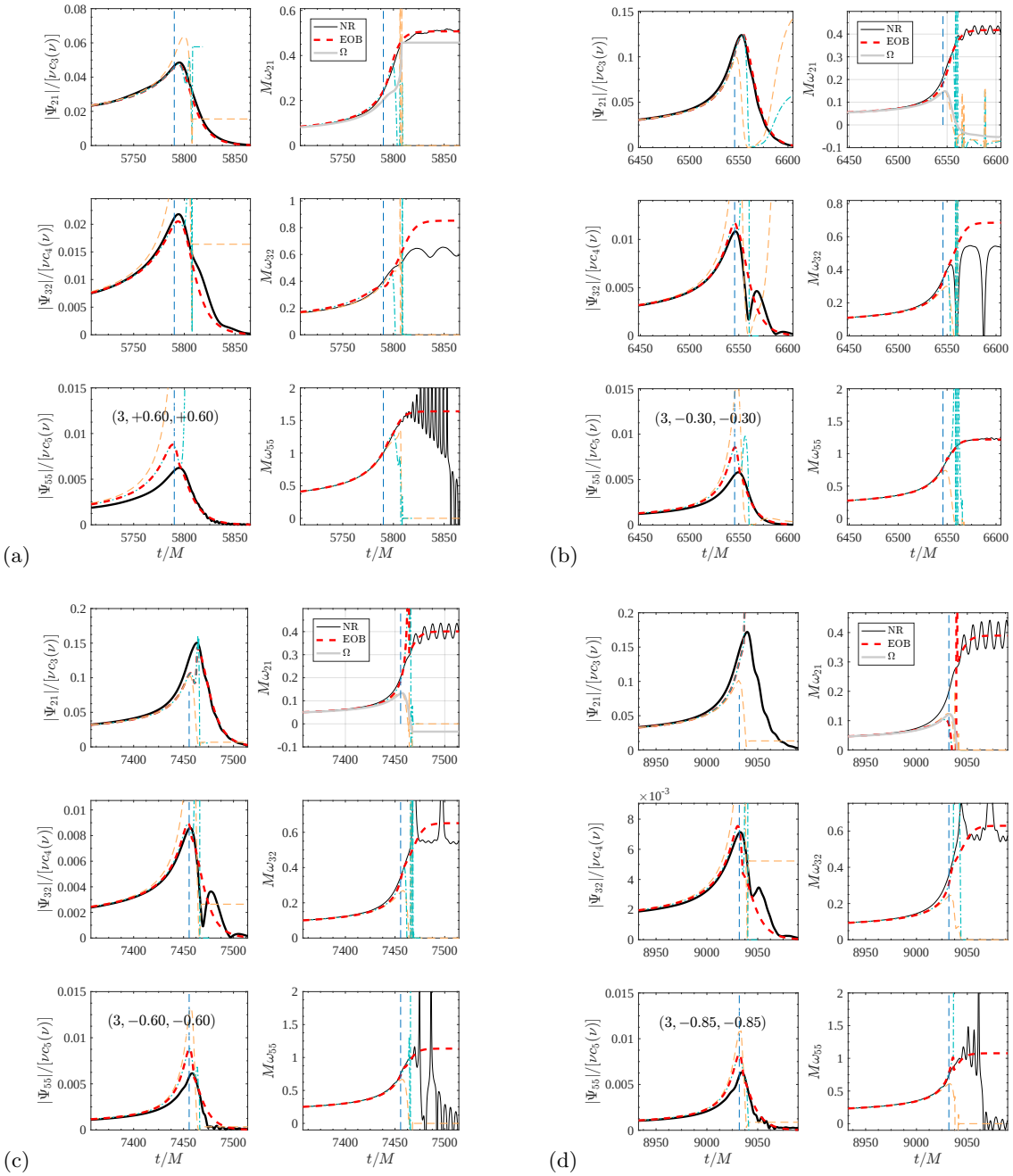

FIG. 8. Frequency and amplitude for the $(2,1)$, $(3,2)$ and $(5,5)$ modes for the same BBH configurations of Fig. 7. On top of the NR (black) and complete EOB curves (red, dashed), the plots also show: (i) the analytical EOB waveform, without NQC corrections and ringdown (orange online) and (ii) the NQC-augmented EOB waveform (light-blue online). The dashed, vertical, line marks the merger location, i.e. the peak of the $\ell = m = 2$ waveform amplitude. The $(2,1)$ frequency plots also incorporate the orbital frequency Ω (grey online). The construction of the $(2,1)$ mode through merger and ringdown cannot be accomplished correctly for large values of the spins anti-aligned with the orbital angular momentum [see panel (c) and (d)].

tion to the current spin-orbit sector of the Hamiltonian that may eventually improve the behavior of the $(2,1)$ mode in the anti-aligned spin case.

2. *Multipoles* $(3,1)$, $(4,3)$ *and* $(4,2)$

From fits of the SXS waveforms we can also obtain a postmerger/ringdown description of the $(3,1)$, $(4,2)$ and $(4,3)$ modes. For simplicity and robustness, the $(3,1)$ ringdown relies on the nonspinning fits of Ref. [30], while

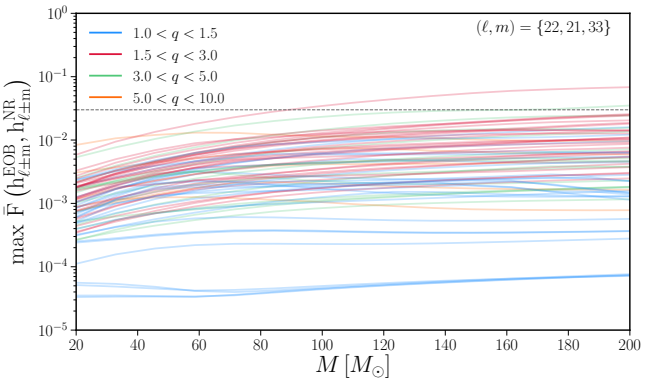

FIG. 9. EOB/NR unfaithfulness, maximized over the direction from the sky, when including $(2,2)$, $(2,1)$ and $(3,3)$ modes. Here we only consider a subset of the SXS waveforms with $\chi_i > -0.4$, where the $(2,1)$ EOB waveform mode does not present pathologies (see Fig. 8). The worst case configuration is `SXS:BBH:0239`, a binary of mass ratio and spins $(2.0, -0.37, +0.85)$.

for $(4,3)$ and $(4,2)$ the relevant information is found in Appendix D 2 g-D 2 f. When the magnitude of the spins are relatively mild, these modes can be modeled rather accurately (modulo mode mixing during ringdown) as in the nonspinning case [30]. Figure 10 illustrates this fact for $(3, +0.30, +0.30)$, with the usual EOB/NR comparison as we did above. For $(4,3)$ and $(4,2)$ modes one can appreciate the relevant action of the NQC factor. When spins are larger (and notably anti-aligned) one can have Ω-driven pathological effects like the $(2,1)$ mode discussed above. Seen also the (average) lower accuracy of the corresponding NR modes all over the SXS catalog, we postpone a more detailed discussion (and possible improvements) to future work.

3. *Improving the behavior of the* $(2,1)$ *multipole*

The correct behavior of the orbita frequency Ω in the strong-field regime is determined by subtle compensation between the orbital and spin-orbit part of the Hamiltonian. This is the region where our analytical understanding is weaker, as we have to rely on resummed results that are analytically incomplete. From the practical point of view, to NQC-complete the inspiral $(2,1)$ mode following the current scheme it would be sufficient the behavior of Ω be milder after the merger. In practice, we found that this is possible by implementing a small modification to the resummed (G_S, G_{S_*}) functions. The spin-orbit sector of `TEOBResumS` is based on Ref. [33], in particular the gyro-gravitomagnetic functions are given by Eqs. (38), (39), (41), and (42), where the inverse separation u is replaced by the inverse centrifugal radius u_c. While $G^0_S = 2uu_c^2$, Eq. (38) of Ref. [33], has the structure of the Kerr gyro-gravitomagnetic function, the

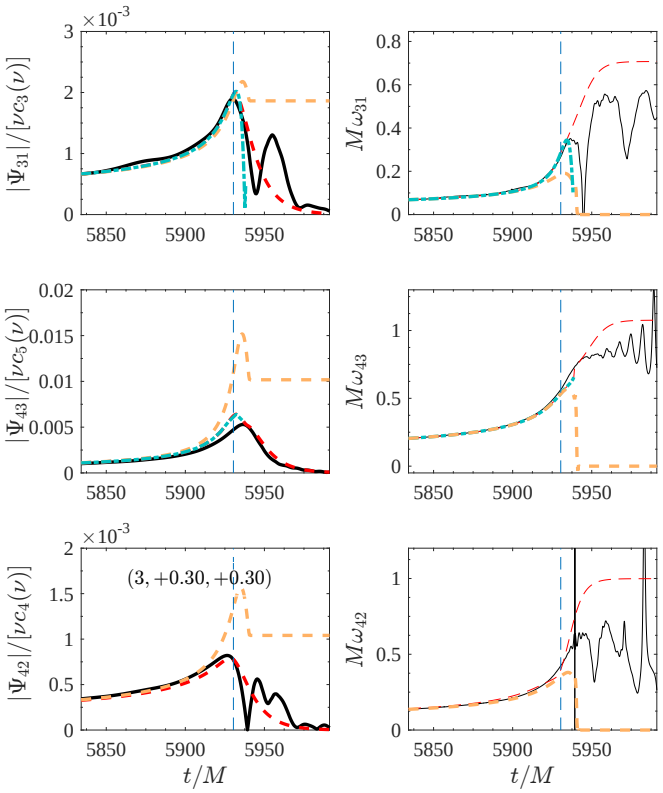

FIG. 10. Illustrative EOB/NR comparison for modes $(3,1)$, $(4,3)$ and $(4,2)$ for $(3, +0.3, +0.3)$. This behavior is analogous to the nonspinning case and is robust until the spins are mild. For larger spins, these modes may suffer the same problem related to the NQC factor discussed above for the $(2,1)$ mode.

dependence of u_c introduced in the other functions, $G^0_{S_*}$, $\hat{G}_S$ and $\hat{G}_{S_*}$ was an arbitrary choice. One finds that replacing such u_c dependence with the, more natural, u-dependence is sufficient to provide small modifications in the behavior of Ω that entail a far more robust behavior of the NQC correction. In practice, we use

$$G_S = 2uu_c^2 \hat{G}_S(u), \tag{50}$$

$$G_{S_*} = \frac{3}{2} u^3 \hat{G}_{S_*}(u), \tag{51}$$

where $(\hat{G}_S, \hat{G}_{S_*})$ are given by Eqs. (41)-(42) of Ref. [33] where u_c is replaced by u. The result of this change for $(3, -0.85, -0.85)$ is illustrated in Fig. 11. Note that, since the dynamics has now changed, to get a good $(2,2)$ EOB/NR phasing agreement we had to use $c_3 = 86.5$ instead of $c_3^{\rm fit} = 79.98$ from Eq. (39). Comparing Fig. 11 with the panel (d) of Fig. 8 one immediately notices the different behavior of the orbital frequency, whose peak is shallower than before. The consequence of this behavior is that the action of the NQC factor on both amplitude and frequency is more correct than before, though not yet fully accurate for this latter. Although improvable, this proves that the scheme for completing the EOB waveform through merger and ringdown for all modes that

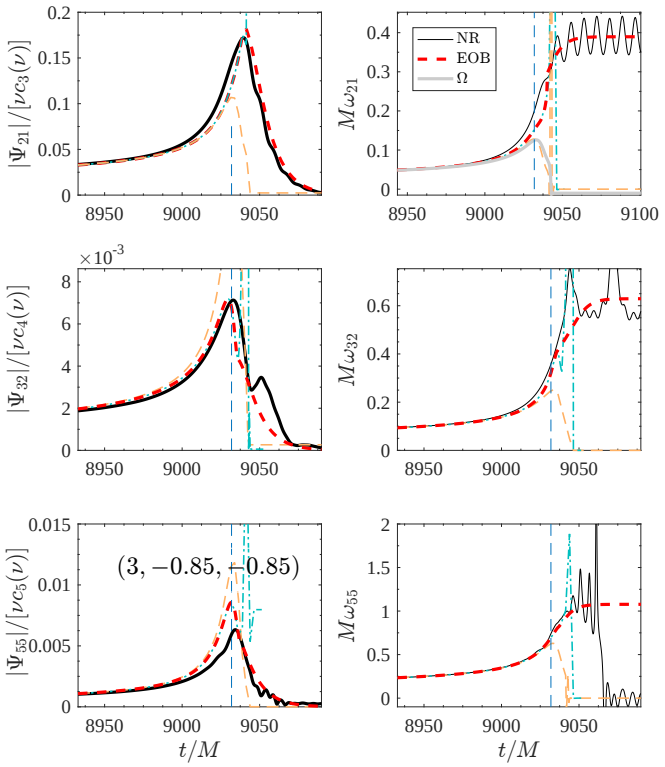

FIG. 11. Attempt of improving the behavior of the $(2,1)$ mode for $(3,-0.85,-0.85)$ by modifying the spin-orbit sector of the EOB Hamiltonian. The related change in the EOB orbital frequency, Ω, that is seen now to decrease more mildly after its peak than in Fig. 8 (d), is sufficient to improve the efficiency of the NQC correction, so to get a more acceptable frequency growth that can be smoothly connected with the ringdown. See text for additional details.

TABLE III. Frequency of the minimum of the $(2,1)$ amplitude for a few BBH configurations considered in Ref. [15] and not publicly available. $M\Omega_0$ is the (orbital) frequency corresponding to a minimum (or a zero) in the amplitude. Our EOB-predicted value, from the zero of $\hat{f}^{\rm S}_{21}$ in Table I, is more consistent with the NR one than the straightforward PN value.

Name	q	χ_1	χ_2	$\hat{S}$	$M\Omega_0^{\rm NR}$	$M\Omega_0^{\rm EOB}$	$M\Omega_0^{\rm PN}$
SXS:BBH:0614	2	0.75	−0.5	0.278	0.083	0.0968	0.057
SXS:BBH:0612	1.6	0.5	−0.5	0.115	0.068	0.0712	0.047
SXS:BBH:1377	1.1	−0.4	−0.7	−0.268	0.033	0.0330	0.029

was seen to be efficient in the nonspinning case [30] *can* be straightforwardly generalized to the spinning case provided the dynamics, i.e. the orbital frequency, behaves correctly. The result of Fig. 11 gives us a handle to improve the description of spin-orbit effects within the EOB Hamiltonian in future work.

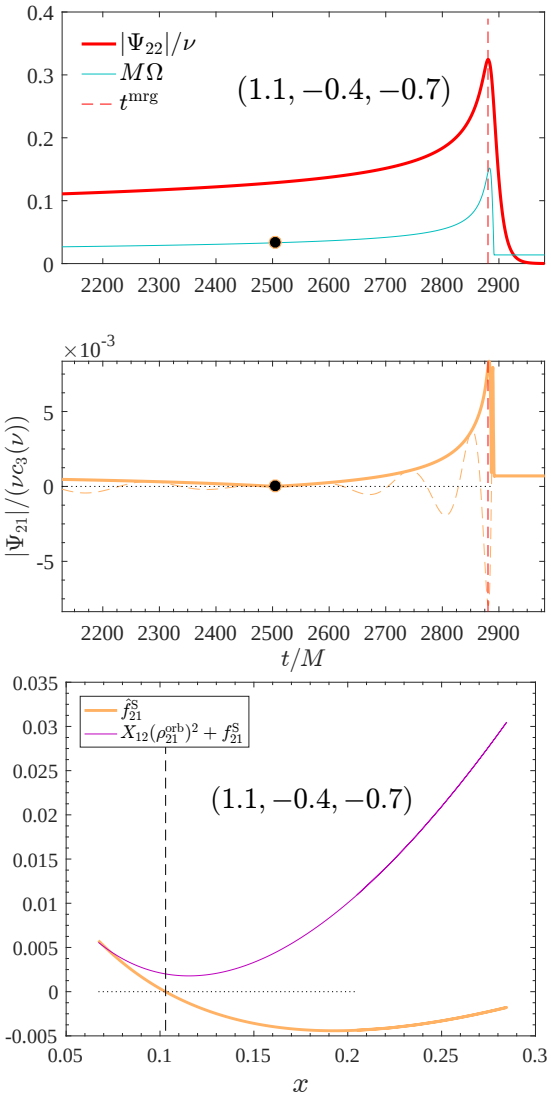

FIG. 12. Top and medium panels: occurrence of a zero in the $(2,1)$ amplitude in configuration $(1.1,-0.4,-0.7)$, corresponding to NR dataset `SXS:BBH:1377` analyzed in Ref. [15]. This dataset is not publicly available through the SXS catalog. The EOB-predicted value of the frequency is perfectly compatible with the NR value reported in Ref. [15] (see the last row of Table III). The bottom panel compares the zero location of the resummed (orange) and nonresummed (magenta) amplitudes. See text for details.

C. Peculiar behavior of $m = 1$ waveform amplitudes for $1 \leq q \leq 2$.

Reference [15] pointed out that a few NR simulations exhibit a minimum in the $(2,1)$ mode amplitude in the late inspiral phase. Such behavior was found in 4 SXS datasets: `SXS:BBH:0254` $(2,+0.6,-0.6)$; `SXS:BBH:0612` $(1.6,0.5,-0.5)$; `SXS:BBH:0614` $(2,+0.75,-0.5)$; and `SXS:BBH:1377` $(1.1,-0.4,-0.7)$. Only the first among these dataset if public through the SXS catalog. In addi-

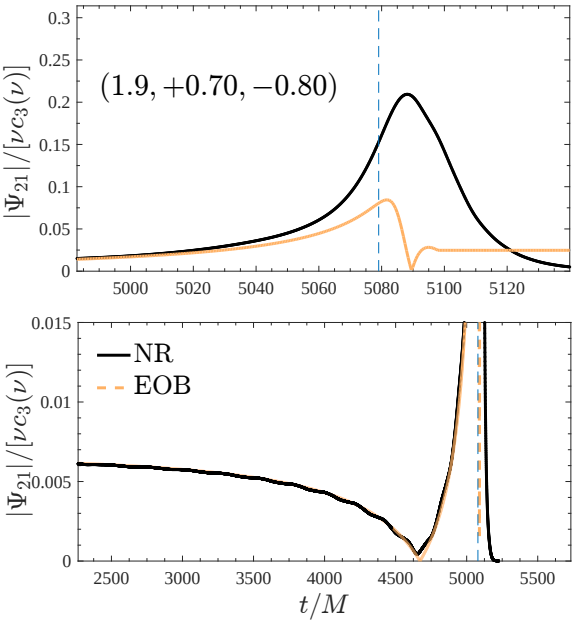

FIG. 13. Mode $(2,1)$: comparison between the EOB amplitude (orange) and the corresponding NR one from dataset `SXS:BBH:1466`. The purely analytical EOB waveform multipole can accurately predict the location of the minimum (that analytically is a zero of the modulus) consistently with the one found in the NR data. The excellent agreement shown is obtained *naturally*, without the need of calibrating any additional parameter entering the waveform amplitude. The dashed vertical line corresponds to merger time, i.e. the peak of the $\ell = m = 2$ waveform. The cusp in the analytical amplitude occurs because of a zero in $\hat{f}^{\rm S}_{21}$ as illustrated in Fig. 14.

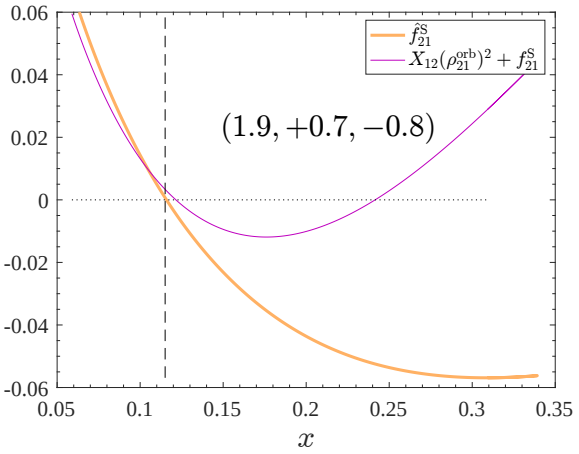

FIG. 14. Complementing Fig. 13: the behavior of the resummed versus nonresummed amplitude versus $x = \Omega^{2/3}$.

tion, Ref. [15] noticed that the same feature is present in the EOB resummed waveform (both in orbital-factorized and non-orbital factorized form). An explanation of this phenomenon was suggested on the basis of leading-order considerations, that were similarly proven using a 3PN-based analysis. In addition, Ref. [15] compared the PN prediction for the frequency corresponding to the minimum of the $(2,1)$ mode with the value extracted from NR simulations. From this PN-based analysis, Ref. [15] suggested that the phenomenon comes from a compensation between the spinning and leading-order nonspinning terms entering the $(2,1)$ mode. Notably, the PN based analysis aimed at explaining this feature qualitatively as well as semi-quantitatively (see Table I in Ref. [15]).

Here we revisit the analysis of Ref. [15] and we attempt to improve it along several directions thanks to the robustness of our factorized and resummed waveform amplitudes. In brief we can show that: (i) focusing on the same datasets considered in Ref. [15], we illustrate that the $(2,1)$, *purely analytical* EOB amplitude has a minimum (in fact, a zero) rather close to the values reported in Table I of Ref. [15], and definitely much closer than the PN-based prediction; (ii) the phenomenon is here understood as coming from the compensation, occurring at a given frequency, between the two (inverse-resummed) macro-terms that compose the analytically resummed expression of $\hat{f}^{S}_{21}$, one proportional to X_{12} and the other one proportional to $\tilde{a}_{12}$, and that appear with opposite signs; (iii) guided by this analytical understanding, we investigated whether some of the currently available simulations in the SXS catalog may develop a zero (that occurs in fact as a cusp) in the amplitude. Quite remarkably we found that it is indeed the case for `SXS:BBH:1466`, $(1.9, +0.70, -0.8)$, that shows a clean minimum that is perfectly consistent with the EOB-based analytical prediction; (iv) since the same structure, with the minus sign, is present also in other $m =$ odd modes, we investigated whether the same phenomenon may show up also in some of the other SXS datasets. Interestingly, we found that also the $(3,1)$ mode of `SXS:BBH:1496` is consistent with the EOB-predicted analytical behavior, suggesting that such features may occur in several modes.

Let us now discuss in detail the four points listed above. Figure 12 illustrates an EOB analytical waveform for $(1.1, -0.4, +0.7)$, that corresponds to the dataset SXS:BBH:1377. As mentioned above, this simulation is not public and so we cannot perform an explicit EOB/NR comparison. The top panel shows the $\ell = m = 2$ waveform amplitude together with the EOB orbital frequency $M\Omega$. The middle panel shows the $(2,1)$ waveform amplitude, that develops a zero highlighted by a marker. It turns out that this zero precisely corresponds to the zero of the $\hat{f}^{\rm S}_{21}$ function once evaluated at $x = (M\Omega)^{2/3}$. This function is shown, versus x, in the bottom panel of Fig. 12. To be more quantitative, the last row of Table III lists the corresponding frequency, that is identical to the NR-extracted value reported in the corresponding last column of Table I of [15]. To check the model further, we explored also the other two cases in the Table, similarly finding a rather good agreement between the EOB orbital frequency corresponding to the zero and

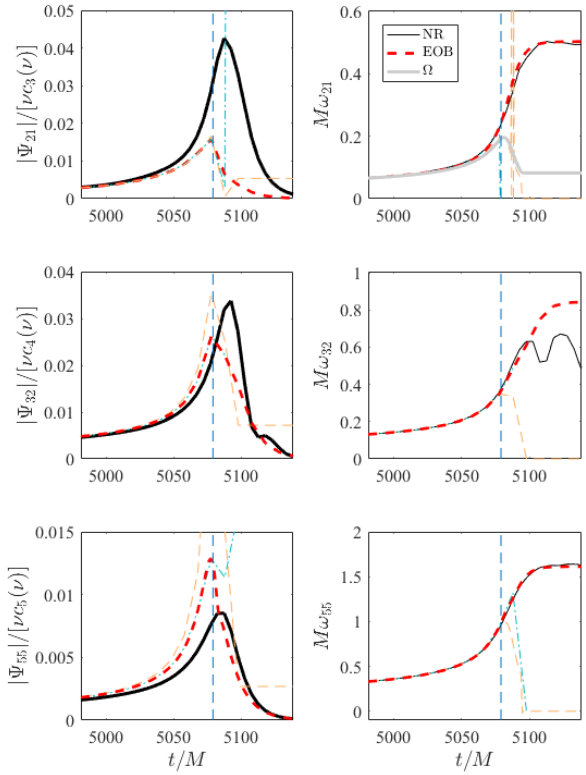

FIG. 15. EOB/NR waveform comparison for `SXS:BBH:1466` for modes $(2,1)$, $(3,2)$ and $(5,5)$. The frequency of the $(2,1)$ mode behaves correctly through merger and ringdown, while the EOB amplitude largely underestimates the NR one. As in Fig. 8, the orange curve is the purely analytical EOB waveform, while the light blue one is the NQC corrected. The vertical line marks the merger location

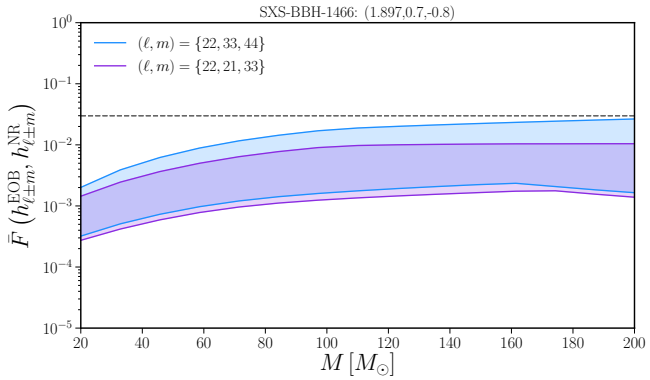

FIG. 16. The minimum and maximum EOB/NR unfaithfulness for `SXS:BBH:1466` over the whole sky. The blue curve uses the $(2,2)$, $(3,3)$ and $(4,4)$ modes. The purple curve uses the $(2,2)$, $(2,1)$ and $(3,3)$ modes. Worst case mismatches occur near edge on configurations with the unfaithfulness being below 3% up to $200M_\odot$.

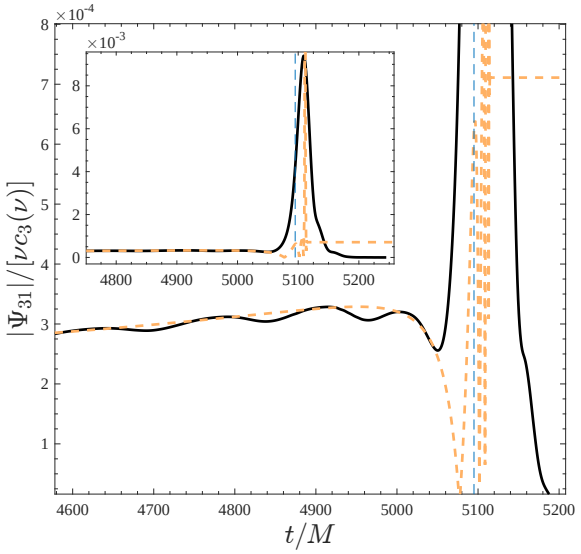

FIG. 17. Mode $(3,1)$: comparison between the EOB amplitude (orange) and the corresponding NR one from dataset `SXS:BBH:1496`, $(1.1584, +0.7997, +0.0285)$. While the analytical waveform has a zero because of $\hat{f}_{31}$, the NR one just shows a glimpse of a global minimum, probably because if insufficient numerical resolution. Note however the excellent qualitative and quantitative consistency between the two waveforms up to that point.

the NR value[4]. Our reasoning relies on our orbital factorized waveform, and in particular on the definition of $\hat{f}^{\rm S}_{21}$. However, Ref. [15] pointed out that a zero in the amplitude may occur also in the standard, non orbital-factorized, waveform amplitude. To make some quantitative statement, we also consider the function

$$f^{\rm orb+S}_{21} = X_{12}\left(\rho^{\rm orb}_{21}\right)^2 + f^{\rm S}_{21}, \tag{52}$$

where both $\rho^{\rm orb}_{21}$ and $f^{\rm S}_{21}$ are kept in PN-expanded form. The orbital term is given in the usual Taylor-expanded form $\rho^{\rm orb}_{21} = 1 + (\dots)x + (\dots)x^2 + (\dots)x^3 + (\dots)x^4 + (dots)x^5$. The spin term, at NNLO, reads

$$f^{\rm S}_{21} = -\frac{3}{2}\tilde{a}_{12}x^{1/2} + c^{\rm NLO}_{\rm SO}x^{3/2} + c^{\rm LO}_{\rm SS}x^2 + c^{\rm NNLO}_{\rm SO}x^{5/2}, \tag{53}$$

[4] Note that Ref. [15] does not explain how their $M\Omega^{\rm NR}_0$ is computed. We may imagine that it is just given by the NR orbital frequency divided by two, which is slightly different from the EOB orbital frequency we include due to the presence of tail terms and other effects.

where

$$c_{\rm SO}^{\rm NLO} = \left(\frac{110}{21}+\frac{79}{84}\nu\right)\tilde{a}_{12} - \frac{13}{84}\tilde{a}_0 X_{12}, \tag{54}$$

$$c_{\rm SS}^{\rm LO} = -\frac{27}{8}\tilde{a}_0\tilde{a}_{12} + \frac{3}{8}X_{12}\left(\tilde{a}_1^2 + \frac{10}{3}\tilde{a}_1\tilde{a}_2 + \tilde{a}_2^2\right), \tag{55}$$

$$c_{\rm SO}^{\rm NNLO} = \left(-\frac{3331}{1008} - \frac{13}{504}\nu + \frac{613}{1008}\nu^2\right)\tilde{a}_{12} + \left(-\frac{443}{252}+\frac{1735}{1008}\right)\tilde{a}_0 X_{12} + \frac{3}{4}\tilde{a}_0^2\tilde{a}_{12}. \tag{56}$$

For the configuration $(1.1, -0.4, -0.7)$, this function, represented versus x, *does not* have a zero, as illustrated by the magenta line in the bottom panel of Fig. 12.

The closeness between the numbers in Table III prompted us to additionally investigate for which values of spin and mass ratio the analytical $(2,1)$ amplitude develops a zero before merger frequency. Comparing with the configurations available through the SXS catalog (notably those up to February 3, 2019), we found that the parameters of dataset `SXS:BBH:1466` are such that the zero in the amplitude occurs at a frequency that is *smaller* than the merger frequency. We then explicitly checked the $(2,1)$ mode of this simulation and, as illustrated in Fig. 13, we found that it has a local minimum, that is very consistent with the cusp in the analytic EOB waveform modulus. In addition, Fig. 15 illustrates the behavior of the full waveform completed by NQC corrections and ringdown. As above, we show together the more difficult modes to model, $(2,1)$ and $(3,2)$, with $(5,5)$. The figure highlights that the $(2,1)$ frequency is well captured by the analytical model, although the amplitude is underestimated by more than a factor two. Consistently, Fig. 16 shows that the minimum and maximum unfaithfulness over the whole sky is always below 3%. This makes us confident that `TEOBiResumS_SM` can give a reliable representation of the $(2,1)$ mode also in this special region of the parameter space, since it naturally incorporates a feature that is absent in `SEOBNRv4HM` [15]. One should however be aware that the $(2,1)$ EOB mode is not as good for the case $(2, +0.60, -0.60)$, where the corresponding NR waveform is found to have very a clean minimum much closer to the merger frequency, as noted in Ref. [15]. This is probably due to lack of additional analytical information to improve the behavior of the $(2,1)$ mode in the strong-field regime. It would be interesting to investigate, for future work, whether higher-order PN terms (e.g. those obtained after hybridization with test-mass results, similarly to the procedure followed for the $m =$ even) could be useful to improve the behavior of the $(2,1)$ EOB amplitude for $(2, +0.60, -0.60)$.

As a last exploratory study, we investigated whether some of the other m-odd multipolar amplitudes can develop a zero at a frequency smaller than the merger frequency, and we found this happens for several modes. In the SXS catalog (up to February 3, 2019) we identified a configuration where, analytically, we may expect a zero in the $(3,1)$ mode. This is `SXS:BBH:1496`, with parameters $(1.1584, 0.7997, 0.0285)$. Figure 17 compares the analytical EOB waveform amplitude with the NR one. We think it is remarkable that the NR is consistent with the analytic waveform (modulo some numerical oscillation) up to $t/M \simeq 5050$. At this time the NR waveform develops a local dip that, we conjecture, would eventually lead to an approximate cusp by increasing the resolution. We hope that these special features of the waveform could be investigated in more detail by dedicated NR simulations.

V. CONCLUSIONS

We have introduced `TEOBiResumS_SM`, an improved, NR-informed, EOB model for nonprecessing, spinning, coalescing black hole binaries. This model incorporates several subdominant waveform modes, beyond the quadrupolar one, that are completed through merger and ringdown. The work presented here generalizes to the spinning case the nonspinning model `TEOBiResumMultipoles` presented in Paper I, Ref. [30]. Generally speaking, we found that modes with $m = \ell$, up to $\ell = 5$, are the most robust ones all over the parameter space covered by the SXS and BAM NR simulations at our disposal. The other modes, and especially the most relevant $(2,1)$ one, can be nonrobust for medium-to-large value of the spins anti-aligned with the orbital angular momentum. The waveform modes (and thus the radiation reaction) rely on a new resummed representation for the waveform multipolar amplitudes, that improves their robustness and predictive power through late-inspiral and merger, as well as a new, NR-informed, representation of the ringdown part.

Our results can be summarized as follows:

1. The new analytical description of the binary relative dynamics due to the orbital-factorized and resummed radiation reaction entails a new (somehow simpler) determination of the EOB flexibility functions $\{a_6^c(\nu), c_3(\nu, S_1, S_2)\}$, that is different from the one used in `TEOBResumS` [24]. We computed the EOB/NR unfaithfulness for the $(2,2)$ mode and found that it is always well below 0.7% all over the current release of the SXS NR waveform catalog (473 datasets) as well as on additional data from BAM code spanning up to mass ratio $q = 18$. We remark that the performance of the model is largely improved, with respect to Ref. [24], in the large-mass-ratio, large-spin corner, notably for $(8, +0.85, +0.85)$.

2. We provided a prescription for completing higher modes trough merger and ringdown. Such prescription is the carbon copy of what previously done in the nonspinning case and discussed in Paper I. No new conceptual modification to the procedure were introduced here. The novelty is the introduction of the spin-dependence in the NR-informed fits of the

quantities needed to determine the NQC parameters and the peak-postpeak (ringdown) behavior. Such fits are done factorizing some leading-order spin contributions, as well as incorporating test-mass information, in an attempt to reduce the flexibility in the fits and to improve their robustness all over the parameter space.

We found that for $\ell = m$ modes, up to $\ell = m = 5$, the model is very robust and reliable. When putting together all $m = \ell$ modes up to $\ell = 4$, the maximal EOB/NR unfaithfulness all over the sky (with Advanced LIGO noise) is always well below 3% up to total mass $M = 120 M_\odot$, that is exceeded slightly after because of lack of accuracy in both the EOB and the NR data itself, especially in the $(4, 4)$ mode. The model peforms similarly well ($\bar{F} \lesssim 3\%$) aso when the $(2, 1)$ mode is included. We have however pointed out that for large values of the spin, anti-aligned with the angular momentum, e.g. as $(3, -0.85, -0.85)$, inaccuracies in the postmerger EOB dynamics prevent one to get accurate $(2, 1)$ mode through merger and ringdown.

3. Inspired by previous work, we could confirm that the phenomenology of the $(2, 1)$ mode is rich, in particular that its amplitude can have a zero during the late-inspiral before merger for nearly equal-mass binaries. We have presented a quantitative understanding of the phenomenon. We also showed that the EOB waveform, in its orbital-factorized and resummed avatar of Ref. [31, 32], can accurately reproduce NR waveforms with the same phenomenology, at least when the frequency of the zero is sufficiently far from merger. We remark that was achieved *without* advocating any additional ad-hoc calibration or tuning of phenomenological parameters entering the waveform amplitude. Quite interestingly, the same phenomenon may occur also in some of the other of the $m =$ odd modes. In particular, we could find, for the $(3, 1)$ mode, a SXS configuration that shows this behavior and illustrate how it agrees with the analytical prediction.

4. In general, this work made us aware that the structure of the $(2, 1)$ mode is very challenging to be modeled properly through peak and ringdown using the simple approach developed in Paper I. Such difficulty is shared by other modes with $m \neq \ell$ in certain region of the parameter space, whenever the peak of such mode is significantly ($\sim 7 - 8M$) delayed with respect to the merger time (e.g. the $(4, 3)$ or $(3, 1)$). We consider the identification of this difficulty as one of the most relevant outcomes of this work. We think that the proper modelization of such $m \neq \ell$ modes in the transition from the late inspiral up to the waveform peak should not be done using brute force (e.g. by extending the effective postmerger fits also *before* the peak) but rather that it requires a more detailed understanding of the underlying physical elements, in particular: (i) the structure of the waveform (e.g. with the need of naturally incorporating the zero in the amplitude also when it is known to exist at rather high frequencies, e.g. for $(2, +0.60, -0.60)$); and (ii) the behavior of the EOB relative dynamics (notably mirrored in the time evolution of the orbital frequency $\Omega(t)$) in the extreme region just after the merger, corresponding to very small radial separation. We have shown explicitly that one of the analytical choices adopted in `TEOBResumS`, i.e. the u_c dependence in the gyro-gravitomagnetic functions, was (partly) responsible of the problems we encountered in modeling the $(2, 1)$ mode (see Sec. IV B 3). Together with a different choice of gauge, so to incorporate the test-black hole spin-orbit interaction [29], it might be possible to obtain an improved EOB dynamics more robust also in the postmerger regime, so to easily account for more subdominant multipoles via the usual NQC-completion and ringdown matching procedure.

ACKNOWLEDGMENTS

We are grateful to T. Damour for discussions. F. M., G. R. and P. R. thank IHES for hospitality during the development of this work.

Appendix A: Long-inspiral Numerical Relativity waveforms

This Appendix discussed 11 very long waveforms, summarized in Table XV, that have been made available in the SXS catalog with the latest updates this year. These waveforms all show an inspiral of over 100 orbits before a common horizion appears[5]. Figure 18 displays the $\bar{F}$ curves of these datasets. First, it should be noted that 6 waveforms are shown here that are not included in the analysis presented in Section III. These waveforms are marked in light blue. All, with the exception of `SXS:BBH:1385`, show a large unfaithfulness for low masses, with $\max(\bar{F}) > 3\%$ for `SXS:BBH:1393`. Figure 19 illustrates the time-domain alignment of EOB and NR waveforms for this extreme case. The waves are aligned on the frequency interval $[\omega_L, \omega_R] = [0.014, 0.03]$. Seen the large oscillations that show up in the amplitude, we are prone to think that at least part of this difference is due to yet uncontrolled systematics in the NR waveforms. As already mentioned in the main text, `SXS:BBH:1415` also shows unfaithfulness above 1% for small values of

[5] `SXS:BBH:1110` is excluded from this analysis since the waveform needs additional post-processing.

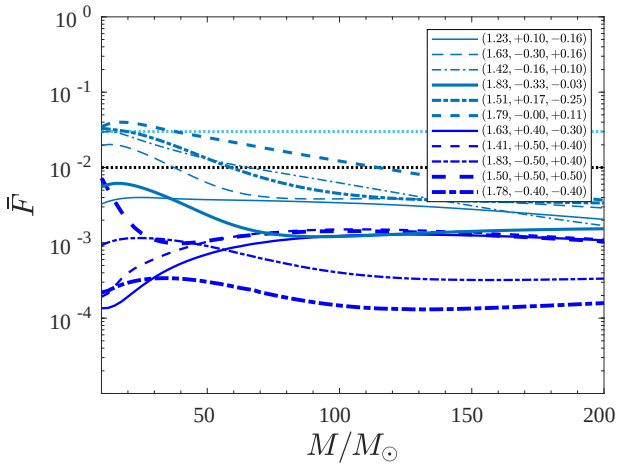

FIG. 18. Complement to Fig. 3 including all very long waveforms available in the SXS catalog. Note that a few of them are above the 1% threshold because of spurious effects during the inspiral.

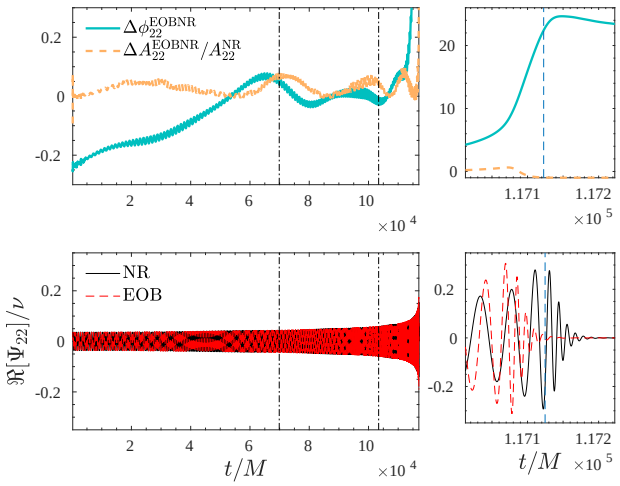

FIG. 19. EOB/NR time-domain phasing comparison for SXS:BBH:1393, (1.79,0,0.115), that explains why $\bar{F}$ grows for small total masses. The vertical lines indicate the alignment frequency region $[M\omega_L, M\omega_R] = [0.014, 0.022]$.

the total mass. Computing the unfaithfulness between the two highest levels of NR can be used as a conservtive estimate on the error. Figure 20 exhibits this comparison directly for `SXS:BBH:1415`: this suggests that the relatively large EOB/NR unfaithfulness is likely due to NR uncertainties.

Appendix B: Numerical Relativity datasets

The NR data used in this work were seperated into two categories. A set used for the *calibration of the postpeak and ringdown* and a set used excusively for *validation* of the model. The *postpeak-calibration* set consists of the following: (i)The set of the NR data is extended beyond the 23 non-spinning waveforms used in [30] (19 SXS, 3 BAM, 1 test-particle) .(ii) 38 SXS, spin-aligned, equal-mass waveforms with spins between $-0.99\chi_{1,2} \leq 0.9942$. See Table IV. (iii)78 SXS spin-aligned, unequal-mass, waveforms going up to mass ratio $q = 8$ with spins up to $-0.85 \leq \chi_{1,2} \leq 0.85$. See Table V – VI. This also includes a single high-precision waveform with $(q, \chi_1, \chi_2) = (8, -0.9, 0)$. (iv) 16 `BAM`, spin-aligned, unequal-mass waveforms from spanning mass ratios $2 \leq q \leq 18$, including two $q = 8$ waveforms with $\chi_1 = \chi_2 = \pm 0.85$ and two $q = 18$ waveforms with $\chi_1 = \pm 0.8$. See Table VII. (v) A set of waveforms for a test-particle inspiralling and plunging on a Kerr black hole [45] with the black hole spin $\hat{a}$ in the interval $-0.99 \leq \hat{a} \leq 0.99$. The NR waveforms contain between 12.4 and 62.1 orbits before the formation of a common horizon, with an average length of 24.4 orbits, while the eccentricity never exceeds 0.004.

The *validation* set consists of 338 waveforms from the publicly available catalog of the SXS collaboration. The waveforms span mass ratios up to $q = 8$ and spins up to $-0.97 \leq \chi_{1,2} \leq 0.998$. This set includes 5 long waveforms with more then 143 orbits before the forming of a common horizon. The remaining waveforms span between 10.0 and 79.8, with an average of 20.9 orbits before the forming of a common horizon, while eccentricity is limited to 0.001. The waveforms are listed in Tables VIII – XIV. Further details on the SXS catalog can be found in Refs. [46–56].

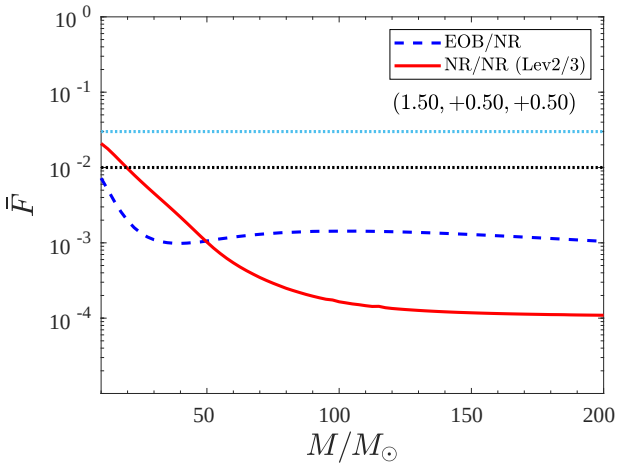

FIG. 20. Complement to Fig. 3 showing a direct comparison of the EOB/NR unfaithfulness vs. the NR/NR unfaithfulness computed with the resolutions *Lev2* and *Lev3*.

Appendix C: Numerical Relativity Systematics

As was highlighted in [30], numerical noise and systematics in the NR data can lead to a degradation in the mismatches. In Fig. 6 we find that the worst mismatches

TABLE IV. This table summarizes the SXS NR waveform data in the *postpeak-calibration* set, with mass-ratio $q = 1$. From left to right, the columns report: the SXS simulation number, mass ratio and dimensionless spins spins χ_i, and the maximum value of the EOB/NR unfaithfulness $\bar{F}$, see Fig. 2.

#	id	(q, χ_1, χ_2)	$\max(\bar{F})[\%]$
1	SXS:BBH:0178	$(1, 0.9942, 0.9942)$	0.0550
2	SXS:BBH:0177	$(1, 0.9893, 0.9893)$	0.0342
3	SXS:BBH:0172	$(1, 0.9794, 0.9794)$	0.0182
4	SXS:BBH:0157	$(1, 0.95, 0.95)$	0.0406
5	SXS:BBH:0160	$(1, 0.9, 0.9)$	0.0141
6	SXS:BBH:0153	$(1, 0.85, 0.85)$	0.0206
7	SXS:BBH:0230	$(1, 0.8, 0.8)$	0.0517
8	SXS:BBH:0228	$(1, 0.6, 0.6)$	0.1388
9	SXS:BBH:0150	$(1, 0.2, 0.2)$	0.1644
10	SXS:BBH:0149	$(1, -0.2, -0.2)$	0.0469
11	SXS:BBH:0148	$(1, -0.44, -0.44)$	0.0274
12	SXS:BBH:0215	$(1, -0.6, -0.6)$	0.0465
13	SXS:BBH:0154	$(1, -0.8, -0.8)$	0.0296
14	SXS:BBH:0212	$(1, -0.8, -0.8)$	0.0304
15	SXS:BBH:0159	$(1, -0.9, -0.9)$	0.0291
16	SXS:BBH:0156	$(1, -0.949, -0.949)$	0.0654
17	SXS:BBH:0231	$(1, 0.9, 0)$	0.1286
18	SXS:BBH:0232	$(1, 0.9, 0.5)$	0.0654
19	SXS:BBH:0229	$(1, 0.65, 0.25)$	0.1380
20	SXS:BBH:0227	$(1, 0.6, 0)$	0.0973
21	SXS:BBH:0005	$(1, 0.5, 0)$	0.1432
22	SXS:BBH:0226	$(1, 0.5, -0.9)$	0.0493
23	SXS:BBH:0224	$(1, 0.4, -0.8)$	0.0493
24	SXS:BBH:0225	$(1, 0.4, 0.8)$	0.1833
25	SXS:BBH:0223	$(1, 0.3, 0)$	0.0745
26	SXS:BBH:0222	$(1, -0.3, 0)$	0.0489
27	SXS:BBH:0220	$(1, -0.4, -0.8)$	0.0347
28	SXS:BBH:0221	$(1, -0.4, 0.8)$	0.1837
29	SXS:BBH:0004	$(1, -0.5, 0)$	0.0328
30	SXS:BBH:0218	$(1, -0.5, 0.5)$	0.0434
31	SXS:BBH:0219	$(1, -0.5, 0.9)$	0.1864
32	SXS:BBH:0216	$(1, -0.6, 0)$	0.0344
33	SXS:BBH:0217	$(1, -0.6, 0.6)$	0.0917
34	SXS:BBH:0214	$(1, -0.62, -0.25)$	0.1088
35	SXS:BBH:0213	$(1, -0.8, 0.8)$	0.0757
36	SXS:BBH:0209	$(1, -0.9, -0.5)$	0.0408
37	SXS:BBH:0210	$(1, -0.9, 0)$	0.0641
38	SXS:BBH:0211	$(1, -0.9, 0.9)$	0.0873
39	SXS:BBH:0306	$(1.31, 0.9612, -0.9)$	0.1985
40	SXS:BBH:0013	$(1.5, 0.5, 0)$	0.1491
41	SXS:BBH:0025	$(1.5, 0.5, -0.5)$	0.1534
42	SXS:BBH:0016	$(1.5, -0.5, 0)$	0.0349
43	SXS:BBH:0019	$(1.5, -0.5, 0.5)$	0.0250

TABLE V. This table summarizes the SXS NR waveform data in the *postpeak-calibration* set, with mass-ratio $1 < q \leq 2$. From left to right, the columns report: the SXS simulation number, mass ratio and dimensionless spins spins χ_i, and the maximum value of the EOB/NR unfaithfulness $\bar{F}$, see Fig. 2.

#	id	(q, χ_1, χ_2)	$\max(\bar{F})[\%]$
44	SXS:BBH:0258	$(2, 0.8713, -0.85)$	0.3884
45	SXS:BBH:0257	$(2, 0.85, 0.85)$	0.3031
46	SXS:BBH:0254	$(2, 0.6, -0.6)$	0.1227
47	SXS:BBH:0255	$(2, 0.6, 0)$	0.1234
48	SXS:BBH:0256	$(2, 0.6, 0.6)$	0.0666
49	SXS:BBH:0253	$(2, 0.5, 0.5)$	0.0697
50	SXS:BBH:0252	$(2, 0.3715, -0.8494)$	0.1561
51	SXS:BBH:0249	$(2, 0.3, -0.3)$	0.0952
52	SXS:BBH:0250	$(2, 0.3, 0)$	0.0813
53	SXS:BBH:0251	$(2, 0.3, 0.3)$	0.0725
54	SXS:BBH:0248	$(2, 0.1287, 0.85)$	0.0628
55	SXS:BBH:0244	$(2, 0, -0.6)$	0.0592
56	SXS:BBH:0245	$(2, 0, -0.3)$	0.0396
57	SXS:BBH:0246	$(2, 0, 0.3)$	0.0357
58	SXS:BBH:0247	$(2, 0, 0.6)$	0.0401
59	SXS:BBH:0243	$(2, -0.1287, -0.85)$	0.0603
60	SXS:BBH:0240	$(2, -0.3, -0.3)$	0.0201
61	SXS:BBH:0241	$(2, -0.3, 0)$	0.0194
62	SXS:BBH:0242	$(2, -0.3, 0.3)$	0.0225
63	SXS:BBH:0239	$(2, -0.37, 0.85)$	0.0364
64	SXS:BBH:0238	$(2, -0.5, -0.5)$	0.0304
65	SXS:BBH:0235	$(2, -0.6, -0.6)$	0.0324
66	SXS:BBH:0236	$(2, -0.6, 0)$	0.0452
67	SXS:BBH:0237	$(2, -0.6, 0.6)$	0.0743
68	SXS:BBH:0234	$(2, -0.85, -0.85)$	0.0780
69	SXS:BBH:0233	$(2, -0.8713, 0.85)$	0.1575

typically come from near edge-on cases, where the power in the $(2,2)$-mode is minimized, and for mass ratios near $q \sim 1$, where the amplitude of the odd-m multipoles is suppressed. When restricting to the $(\ell, m) = (2,2), (3,3)$ and $(4,4)$ modes, as shown in the bottom panel of Fig.6, the mode that contributes the most for the near equal-mass, edge-on configurations is the $(4,4)$ mode. However, as highlighted in Fig. 21, the $(4,4)$ mode in the NR datasets can often be particularly problematic, especially through the merger-ringdown. In particular, we see strong oscillatory features in the instantaneous frequency and un-physical, non-monotonic behaviour in the amplitude. This can result in large mismatches that are relatively uninformative regarding the accuracy of the EOB model against NR. At higher mass ratios, where the mode is well-resolved in NR, the mismatches are under control and well below 3%. At low total masses, where we compute mismatches against a larger portion of the inspi-

TABLE VI. This table summarizes the SXS NR waveform data in the *postpeak-calibration* set, with mass-ratio $3 \leq q$. From left to right, the columns report: the SXS simulation number, mass ratio and dimensionless spins spins χ_i, and the maximum value of the EOB/NR unfaithfulness $\bar{F}$, see Fig. 2.

#	id	(q, χ_1, χ_2)	$\max(\bar{F})[\%]$
70	SXS:BBH:0036	$(3, -0.5, 0)$	0.0272
71	SXS:BBH:0045	$(3, 0.5, -0.5)$	0.1325
72	SXS:BBH:0174	$(3, 0.5, 0)$	0.1365
73	SXS:BBH:0260	$(3, -0.85, -0.8494)$	0.1127
74	SXS:BBH:0261	$(3, -0.7313, 0.85)$	0.1441
75	SXS:BBH:0262	$(3, -0.6, 0)$	0.0393
76	SXS:BBH:0263	$(3, -0.6, 0.6)$	0.1036
77	SXS:BBH:0264	$(3, -0.6, -0.6)$	0.0427
78	SXS:BBH:0265	$(3, -0.6, -0.4)$	0.0302
79	SXS:BBH:0266	$(3, -0.6, 0.4)$	0.0711
80	SXS:BBH:0267	$(3, -0.5, -0.5)$	0.0350
81	SXS:BBH:0268	$(3, -0.4, -0.6)$	0.0377
82	SXS:BBH:0269	$(3, -0.4, 0.6)$	0.0518
83	SXS:BBH:0270	$(3, -0.3, -0.3)$	0.0201
84	SXS:BBH:0271	$(3, -0.3, 0)$	0.0183
85	SXS:BBH:0272	$(3, -0.3, 0.3)$	0.0277
86	SXS:BBH:0273	$(3, -0.2687, -0.8493)$	0.0580
87	SXS:BBH:0274	$(3, -0.2313, 0.85)$	0.0327
88	SXS:BBH:0275	$(3, 0, -0.6)$	0.0571
89	SXS:BBH:0276	$(3, 0, -0.3)$	0.0351
90	SXS:BBH:0277	$(3, 0, 0.3)$	0.0183
91	SXS:BBH:0278	$(3, 0, 0.6)$	0.0239
92	SXS:BBH:0279	$(3, 0.2314, -0.8494)$	0.1186
93	SXS:BBH:0280	$(3, 0.2687, 0.85)$	0.0377
94	SXS:BBH:0281	$(3, 0.3, -0.3)$	0.0680
95	SXS:BBH:0282	$(3, 0.3, 0)$	0.0435
96	SXS:BBH:0283	$(3, 0.3, 0.3)$	0.0299
97	SXS:BBH:0284	$(3, 0.4, -0.6)$	0.1208
98	SXS:BBH:0285	$(3, 0.4, 0.6)$	0.0228
99	SXS:BBH:0286	$(3, 0.5, 0.5)$	0.0172
100	SXS:BBH:0287	$(3, 0.6, -0.6)$	0.1836
101	SXS:BBH:0288	$(3, 0.6, -0.4)$	0.1356
102	SXS:BBH:0289	$(3, 0.6, 0)$	0.0581
103	SXS:BBH:0290	$(3, 0.6, 0.4)$	0.0166
104	SXS:BBH:0291	$(3, 0.6, 0.6)$	0.0135
105	SXS:BBH:0292	$(3, 0.7314, -0.8493)$	0.3565
106	SXS:BBH:0293	$(3, 0.85, 0.85)$	0.4486
107	SXS:BBH:0060	$(5, -0.5, 0)$	0.0163
108	SXS:BBH:0110	$(5, 0.5, 0)$	0.0240
109	SXS:BBH:0208	$(5, -0.9, 0)$	0.0638
110	SXS:BBH:0202	$(7, 0.6, 0)$	0.3702
111	SXS:BBH:0203	$(7, 0.4, 0)$	0.0503
112	SXS:BBH:0205	$(7, -0.4, 0)$	0.0392
113	SXS:BBH:0207	$(7, -0.6, 0)$	0.0629
114	SXS:BBH:0064	$(8, -0.5, 0)$	0.0246
115	SXS:BBH:0065	$(8, 0.5, 0)$	0.1442
116	SXS:BBH:1375	$(8, -0.9, 0)$	0.1482

TABLE VII. This table summarizes the `BAM` NR waveform data in the *postpeak-calibration* set. From left to right, the columns report: the simulation number, mass ratio and dimensionless spins spins χ_i, and the maximum value of the EOB/NR unfaithfulness $\bar{F}$, see Fig. 2. These waveforms were mostly presented in Refs. [57–59]

#	(q, χ_1, χ_2)	$\max(\bar{F})[\%]$
117	$(2, 0.5, 0.5)$	0.3543
118	$(2, 0.75, 0.75)$	0.4344
119	$(3, -0.5, -0.5)$	0.1790
120	$(4, -0.75, -0.75)$	0.3162
121	$(4, -0.5, -0.5)$	0.2176
122	$(4, -0.25, -0.25)$	0.1231
123	$(4, 0.25, 0.25)$	0.0745
124	$(4, 0.5, 0.5)$	0.0482
125	$(4, 0.75, 0.75)$	0.0632
126	$(8, -0.85, -0.85)$	0.4308
127	$(8, 0.8, 0)$	0.2860
128	$(8, 0.85, 0.85)$	0.2399
129	$(18, -0.8, 0)$	0.1456
130	$(18, -0.4, 0)$	0.0390
131	$(18, 0.4, 0)$	0.0153
132	$(18, 0.8, 0)$	0.0997

ral signal, we see excellent agreement between the EOB model and NR for all modes and configurations used in our analysis. In the mismatches shown in Fig. 6, we have removed NR datasets that display obvious pathologies, such as those demonstrated in Fig. 21.

Appendix D: Analytic modeling of the multipolar ringdown waveform

1. Introduction

In this Appendix we discuss the fits of the NR data needed for completing `TEOBiResumS_SM` through merger and ringdown. The fits concern: (i) frequency and amplitude at the peak of each multipole; (ii) the time delays $\Delta t_{\ell m}$ between the peak of each multipole and the peak of the $(2, 2)$ mode; (iii) fits for waveforms quantities at the location at the NQC extraction point. Technical details are all listed in Sec. III D and Sec. V A of Ref. [30] and we address the reader there for complementary information. In Sec. D 2 below we report fits of various waveform quantities at the peak of each multipole, that is amplitude, frequency and time-delay $\left(A^{\rm peak}_{\ell m}, \omega^{\rm peak}_{\ell m}, \Delta t_{\ell m}\right)$. Following Refs. [24, 30, 35, 36], the postpeak waveform needs three additional parameters $\left(c_3^{A_{\ell m}}, c_3^{\phi_{\ell m}}, c_4^{\phi_{\ell m}}\right)$ to be fitted to NR data. This is discussed in Sec. D 3

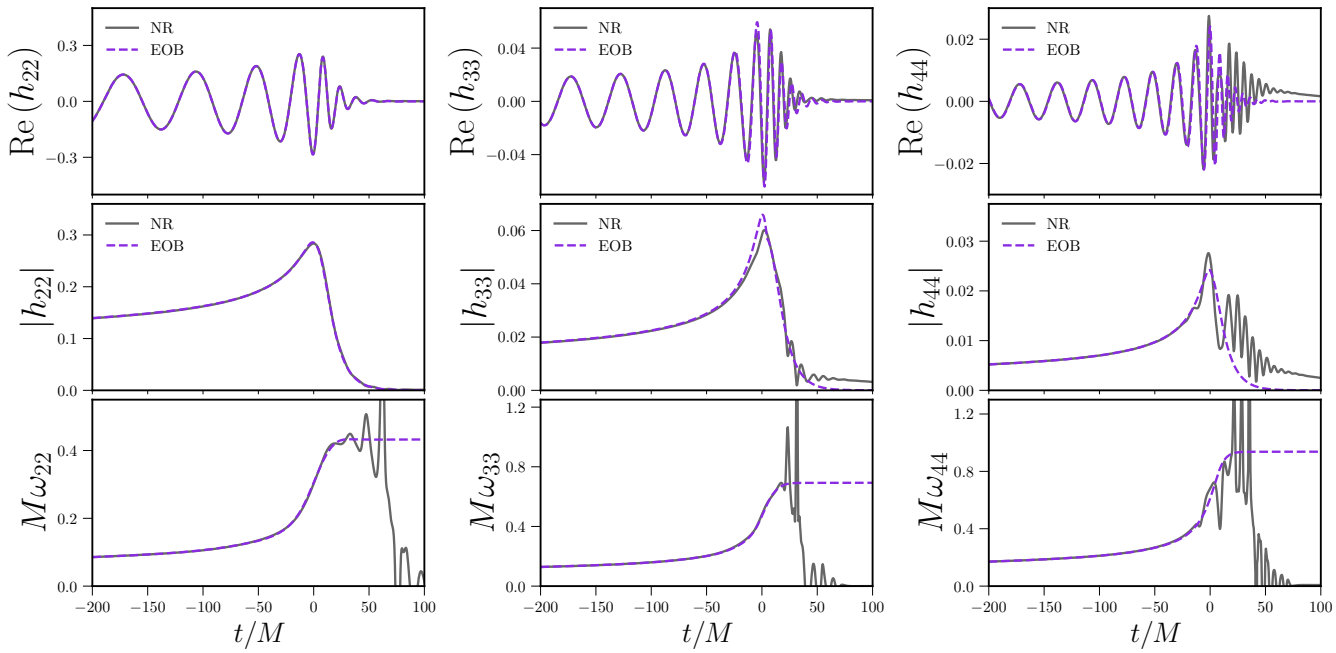

FIG. 21. Strain, amplitude and instantaenous frequency for `SXS:BBH:0039`. Whilst the $(2,2)$ and $(3,3)$ modes are well-behaved, the $(4,4)$ mode demonstrates unphysical features, as seen by the non-monotonic behavior of the amplitude in the merger-ringdown and the strong, oscillatory features in the frequency. This is an example of how NR systematics can lead to relatively poor mismatches against the EOB model.

below. We present spin-dependent fits for multipoles $(2,2),(3,3),(4,4),(5,5)$, although, for robustness, we prefer to use the nonspinning fits discussed in [30] except for the $(2,2)$ mode. This gives a rather accurate representation of the waveform provided that the other quantities (e.g. the peak ones) incorporate the complete spin dependence. The fits of the quasi-normal-mode frequencies and (inverse) damping timpes entering $\left(\omega_1^{\ell m}, \alpha_1^{\ell m}, \alpha_{21}^{\ell m}\right)$ are given in [30][6]. The waveform quantities used to determine the NQC corrections to the waveform amplitude and phase, $\left(A_{\ell m}^{\rm NQC}, \omega_{\ell m}^{\rm NQC}, \dot{A}_{\ell m}^{\rm NQC}, \dot{\omega}_{\ell m}^{\rm NQC}\right)$ are usually obtained analytically from the postpeak template and all details are collected in Sec. D 5 below. For the $(4,4)$ mode, however, this procedure cannot deliver an accurate time-derivative of the waveform amplitude, so that a dedicated fit is given. In the case of the $(\ell,m)=(2,2)$ mode fits for all 4 NQC quanties are also given. Unless otherwise stated all fits are done using `fitnlm` of `matlab` and `NonLinearModelFit` of `MATHEMATICA`. All fits exclusively use the the calibration set taken from the BAM catalog, test-particle data and the *calibration set* of SXS waveforms listed in Appendix B. The exception is Δt_{21}, which is informed additionally by the *test set* of SXS waveforms.

[6] The reader should note that the fits are done versus the spin of the remnant $\hat{a}_f$, which in turn is obtained from the fits presented in Ref. [60].

2. Modeling the peak of each multipole

Firs of all, let us recall some symmetric combinations of the spin variables that will be useful later on

$$\hat{S} \equiv \frac{S_1+S_2}{M^2} = \frac{1}{2}\left(\tilde{a}_0 + X_{12}\tilde{a}_{12}\right), \tag{D1}$$

$$\bar{S} \equiv \frac{S_1-S_2}{M^2} = \frac{1}{2}\left(X_{12}\tilde{a}_0 + \tilde{a}_{12}\right). \tag{D2}$$

We refer to the multipolar decomposition of the strain

$$h \equiv h_+ - i h_\times = \sum_{\ell,m} h_{\ell m}\, {}_{-2}Y_{\ell m}(\iota,\varphi)\ . \tag{D3}$$

Here ${}_{-2}Y_{\ell m}$ are the $s=2$ spin-weighted, spherical harmonics. ι and φ are the polar (with respect to the direction of the orbital angular momentum) and azimuthal angle in the source frame. Each multipole is decomposed in amplitude $A_{\ell m}$ and a phase $\phi_{\ell m}$ as

$$h_{\ell m} = A_{\ell m} e^{{\rm i}\phi_{\ell m}}\ . \tag{D4}$$

The instantaneous GW frequency $\omega_{\ell m}$ is defined as

$$\omega_{\ell m} \equiv -\dot{\phi}_{\ell m}, \tag{D5}$$

TABLE VIII. This table summarizes the SXS NR waveform data in the *validation* set. From left to right, the columns report: the SXS simulation number, mass ratio and dimensionless spins spins χ_i, and the maximum value of the EOB/NR unfaithfulness $\bar{F}$, see Fig. 2.

#	id	(q, χ_1, χ_2)	$\max(\bar{F})[\%]$
133	SXS:BBH:1135	$(1, -0.4375, -0.4375)$	0.0251
134	SXS:BBH:1122	$(1, 0.4376, 0.4376)$	0.1711
135	SXS:BBH:1137	$(1, -0.9692, -0.9692)$	0.1015
136	SXS:BBH:1123	$(1, 0.5, 0.5)$	0.1796
137	SXS:BBH:2102	$(1, 0.6, 0.6)$	0.1394
138	SXS:BBH:2089	$(1, -0.6, -0.6)$	0.0469
139	SXS:BBH:2104	$(1, 0.8, 0.8)$	0.0523
140	SXS:BBH:1475	$(1, -0.8, -0.8)$	0.0301
141	SXS:BBH:1114	$(1, 0.2, -0.0)$	0.1213
142	SXS:BBH:2086	$(1, -0.8, -0.8)$	0.0449
143	SXS:BBH:1141	$(1, -0.4376, -0.4376)$	0.0273
144	SXS:BBH:0328	$(1, 0.8, 0.8)$	0.0519
145	SXS:BBH:1477	$(1, 0.8, 0.8)$	0.0522
146	SXS:BBH:0366	$(1, 0.2, -0.0)$	0.1120
147	SXS:BBH:1134	$(1, -0.4375, -0.4375)$	0.0283
148	SXS:BBH:0329	$(1, -0.8, -0.8)$	0.0448
149	SXS:BBH:2092	$(1, 0.5, -0.5)$	0.0795
150	SXS:BBH:1124	$(1, 1.0, 1.0)$	0.0597
151	SXS:BBH:1509	$(1, -0.244, -0.1)$	0.0442
152	SXS:BBH:2096	$(1, -0.3, -0.0)$	0.0469
153	SXS:BBH:2097	$(1, 0.3, -0.0)$	0.1267
154	SXS:BBH:1506	$(1, 0.4589, -0.32)$	0.0987
155	SXS:BBH:0370	$(1, 0.4, -0.2)$	0.1074
156	SXS:BBH:0459	$(1, -0.4, 0.2)$	0.0547
157	SXS:BBH:0304	$(1, -0.5, 0.5)$	0.0437
158	SXS:BBH:0327	$(1, -0.8, 0.8)$	0.0758
159	SXS:BBH:1497	$(1, 0.6824, 0.6677)$	0.0836
160	SXS:BBH:0330	$(1, -0.8, 0.8)$	0.0758
161	SXS:BBH:2085	$(1, -0.9, 0.9)$	0.0737
162	SXS:BBH:0418	$(1, 0.4, -0.0)$	0.1385
163	SXS:BBH:0415	$(1, -0.4, -0.0)$	0.0172
164	SXS:BBH:2091	$(1, -0.6, 0.6)$	0.0778
165	SXS:BBH:0436	$(1, -0.4, -0.2)$	0.0309
166	SXS:BBH:1144	$(1, -0.4376, -0.4376)$	0.0409
167	SXS:BBH:2087	$(1, -0.8, 0.8)$	0.0754
168	SXS:BBH:1476	$(1, -0.8, 0.8)$	0.0761
169	SXS:BBH:1507	$(1, 0.5067, 0.288)$	0.1112
170	SXS:BBH:0376	$(1, 0.6, -0.4)$	0.1021
171	SXS:BBH:0394	$(1, 0.6, 0.4)$	0.1368
172	SXS:BBH:0462	$(1, -0.6, -0.4)$	0.0441
173	SXS:BBH:0447	$(1, -0.6, 0.4)$	0.0524
174	SXS:BBH:2090	$(1, -0.6, -0.0)$	0.0356
175	SXS:BBH:2088	$(1, -0.625, -0.25)$	0.0524
176	SXS:BBH:2101	$(1, 0.6, 0.0)$	0.0972
177	SXS:BBH:0585	$(1, -0.6, 0.0)$	0.0293
178	SXS:BBH:1481	$(1, 0.7937, 0.7312)$	0.0584
179	SXS:BBH:2103	$(1, 0.65, 0.25)$	0.1376
180	SXS:BBH:1502	$(1, 0.7, -0.42)$	0.1087
181	SXS:BBH:1503	$(1, 0.7266, 0.1356)$	0.0832
182	SXS:BBH:1495	$(1, 0.7791, 0.5337)$	0.0360
183	SXS:BBH:1501	$(1, 0.7527, 0.088)$	0.1291

TABLE IX. This table summarizes the SXS NR waveform data in the *validation* set, with mass-ratios $1 \leq q \leq 1.25$. From left to right, the columns report: the SXS simulation number, mass ratio and dimensionless spins spins χ_i, and the maximum value of the EOB/NR unfaithfulness $\bar{F}$, see Fig. 2.

#	id	(q, χ_1, χ_2)	$\max(\bar{F})[\%]$
184	SXS:BBH:2094	$(1, -0.8, -0.4)$	0.0560
185	SXS:BBH:2095	$(1, 0.8, -0.4)$	0.0729
186	SXS:BBH:1499	$(1, -0.7546, 0.3429)$	0.0347
187	SXS:BBH:2098	$(1, -0.8, 0.4)$	0.0348
188	SXS:BBH:2099	$(1, 0.8, 0.4)$	0.0753
189	SXS:BBH:1500	$(1, -0.7686, -0.2)$	0.0477
190	SXS:BBH:1492	$(1, -0.7934, -0.4707)$	0.0444
191	SXS:BBH:0326	$(1, 0.8, -0.0)$	0.0787
192	SXS:BBH:0325	$(1, -0.8, 0.0)$	0.0427
193	SXS:BBH:2106	$(1, 0.9, 0.5)$	0.0409
194	SXS:BBH:2083	$(1, -0.9, -0.5)$	0.0525
195	SXS:BBH:2093	$(1, 0.9, -0.5)$	0.1101
196	SXS:BBH:2084	$(1, -0.9, 0.0)$	0.0673
197	SXS:BBH:2100	$(1, -0.9, 0.5)$	0.0313
198	SXS:BBH:2105	$(1, 0.9, 0.0)$	0.1028
199	SXS:BBH:1376	$(1, 0.25, 0.5)$	0.1951
200	SXS:BBH:1498	$(1, 0.2232, -0.7837)$	0.0204
201	SXS:BBH:1351	$(1, -0.2281, -0.0)$	0.0522
202	SXS:BBH:0544	$(1.08, -0.0, 0.6865)$	0.2017
203	SXS:BBH:0518	$(1.1088, -0.1367, 0.4346)$	0.1139
204	SXS:BBH:1513	$(1.1474, -0.1052, -0.0091)$	0.0614
205	SXS:BBH:1352	$(1.1506, 0.71, -0.6717)$	0.1258
206	SXS:BBH:1496	$(1.1584, 0.8, 0.0285)$	0.1476
207	SXS:BBH:0626	$(1.1745, -0.8277, 0.7341)$	0.0249
208	SXS:BBH:0311	$(1.186, 0.42, 0.38)$	0.1231
209	SXS:BBH:0523	$(1.2, -0.2073, -0.47)$	0.0338
210	SXS:BBH:0312	$(1.2, 0.39, -0.48)$	0.1018
211	SXS:BBH:0313	$(1.2175, 0.38, -0.52)$	0.0977
212	SXS:BBH:1353	$(1.2183, 0.3308, -0.4382)$	0.0966
213	SXS:BBH:0318	$(1.22, 0.33, -0.44)$	0.0953
214	SXS:BBH:0319	$(1.22, 0.33, -0.44)$	0.1160
215	SXS:BBH:0309	$(1.2212, 0.33, -0.44)$	0.2148
216	SXS:BBH:0305	$(1.2212, 0.33, -0.44)$	0.0956
217	SXS:BBH:0314	$(1.2278, 0.31, -0.46)$	0.0909
218	SXS:BBH:0307	$(1.2278, 0.32, -0.58)$	0.0424
219	SXS:BBH:1490	$(1.2456, 0.4119, 0.7593)$	0.1680
220	SXS:BBH:0465	$(1.25, 0.6, -0.8)$	0.0666
221	SXS:BBH:0486	$(1.25, 0.0, 0.8)$	0.1672
222	SXS:BBH:0438	$(1.25, -0.6, -0.8)$	0.0377
223	SXS:BBH:0559	$(1.25, -0.2, 0.8)$	0.1213
224	SXS:BBH:0475	$(1.25, -0.4, 0.8)$	0.0731
225	SXS:BBH:0409	$(1.25, 0.4, 0.8)$	0.1693
226	SXS:BBH:0503	$(1.25, -0.6, 0.8)$	0.0395
227	SXS:BBH:0535	$(1.25, 0.2, -0.8)$	0.0616
228	SXS:BBH:0386	$(1.25, -0.2, -0.8)$	0.0373
229	SXS:BBH:0398	$(1.25, -0.0, -0.8)$	0.0453
230	SXS:BBH:1223	$(1.25, 0.38, -0.46)$	0.1079
231	SXS:BBH:0591	$(1.25, 0.0, 0.4)$	0.0766
232	SXS:BBH:0464	$(1.25, -0.0, -0.4)$	0.0516
233	SXS:BBH:0466	$(1.25, -0.8, -0.4)$	0.0401
234	SXS:BBH:0377	$(1.25, -0.8, 0.4)$	0.0446

TABLE X. This table summarizes the SXS NR waveform data in the *validation* set, with mass-ratios $1.25 \leq q \leq 1.75$. From left to right, the columns report: the SXS simulation number, mass ratio and dimensionless spins spins χ_i, and the maximum value of the EOB/NR unfaithfulness $\bar{F}$, see Fig. 2.

#	id	(q, χ_1, χ_2)	$\max(\bar{F})[\%]$
235	SXS:BBH:0525	$(1.25, 0.8, -0.4)$	0.1776
236	SXS:BBH:0507	$(1.25, 0.8, 0.4)$	0.1107
237	SXS:BBH:1487	$(1.2545, -0.8, 0.5118)$	0.0418
238	SXS:BBH:0315	$(1.2718, 0.32, -0.56)$	0.0907
239	SXS:BBH:1508	$(1.2791, 0.2928, -0.0741)$	0.1236
240	SXS:BBH:1474	$(1.2821, 0.7237, -0.8)$	0.0891
241	SXS:BBH:1493	$(1.2828, 0.01, 0.8)$	0.1597
242	SXS:BBH:1505	$(1.3256, -0.0949, 0.5545)$	0.0950
243	SXS:BBH:1471	$(1.33, -0.7752, -0.8)$	0.0458
244	SXS:BBH:1482	$(1.3857, -0.5813, 0.8)$	0.0278
245	SXS:BBH:0625	$(1.4, -0.7109, 0.22)$	0.0446
246	SXS:BBH:1473	$(1.45, 0.7, 0.7877)$	0.1585
247	SXS:BBH:1511	$(1.4662, 0.0278, -0.1)$	0.0621
248	SXS:BBH:1146	$(1.5, 0.95, 0.9493)$	0.7163
249	SXS:BBH:0437	$(1.5, -0.2, -0.8)$	0.0433
250	SXS:BBH:0404	$(1.5, -0.0, -0.8)$	0.0577
251	SXS:BBH:0579	$(1.5, 0.4, -0.8)$	0.1247
252	SXS:BBH:0361	$(1.5, -0.0, 0.8)$	0.0815
253	SXS:BBH:0369	$(1.5, 0.6, -0.8)$	0.1771
254	SXS:BBH:0392	$(1.5, -0.2, 0.8)$	0.0630
255	SXS:BBH:0441	$(1.5, 0.6, 0.8)$	0.1344
256	SXS:BBH:0385	$(1.5, 0.8, -0.0)$	0.1593
257	SXS:BBH:0397	$(1.5, -0.8, -0.4)$	0.0334
258	SXS:BBH:0440	$(1.5, -0.0, 0.4)$	0.0745
259	SXS:BBH:0372	$(1.5, 0.8, -0.4)$	0.2114
260	SXS:BBH:1470	$(1.5191, -0.7286, -0.7893)$	0.0441
261	SXS:BBH:0499	$(1.5238, 0.01, 0.7367)$	0.0968
262	SXS:BBH:1480	$(1.5482, -0.8, -0.31)$	0.0339
263	SXS:BBH:1479	$(1.55, -0.557, -0.8)$	0.0402
264	SXS:BBH:0519	$(1.5655, 0.6384, 0.4125)$	0.0731
265	SXS:BBH:1488	$(1.5933, -0.3276, 0.7472)$	0.0336
266	SXS:BBH:1491	$(1.66, 0.2, -0.7)$	0.0911
267	SXS:BBH:0529	$(1.7, -0.0066, 0.527)$	0.0599
268	SXS:BBH:1465	$(1.708, -0.7876, 0.7675)$	0.0786
269	SXS:BBH:0510	$(1.711, -0.0238, -0.7464)$	0.0607
270	SXS:BBH:0501	$(1.75, 0.6, 0.8)$	0.1072
271	SXS:BBH:0423	$(1.75, 0.0, -0.8)$	0.0662
272	SXS:BBH:0488	$(1.75, 0.6, -0.8)$	0.2127
273	SXS:BBH:0473	$(1.75, 0.2, -0.8)$	0.0991
274	SXS:BBH:0435	$(1.75, 0.4, 0.8)$	0.0978
275	SXS:BBH:0355	$(1.75, -0.6, 0.8)$	0.0447
276	SXS:BBH:0414	$(1.75, -0.4, -0.8)$	0.0416
277	SXS:BBH:0566	$(1.75, 0.2, 0.8)$	0.0923
278	SXS:BBH:0512	$(1.75, -0.6, -0.8)$	0.0192
279	SXS:BBH:0451	$(1.75, 0.0, 0.4)$	0.0498
280	SXS:BBH:0550	$(1.75, -0.2, 0.8)$	0.0509
281	SXS:BBH:0382	$(1.75, -0.0, 0.8)$	0.0658
282	SXS:BBH:0402	$(1.75, -0.8, 0.4)$	0.0840
283	SXS:BBH:0371	$(1.75, -0.0, -0.4)$	0.0522
284	SXS:BBH:0454	$(1.75, -0.8, -0.4)$	0.0237
285	SXS:BBH:0552	$(1.75, 0.8, -0.4)$	0.2288

TABLE XI. This table summarizes the SXS NR waveform data in the *validation* set, with mass-ratios $1.75 \leq q \leq 2$. From left to right, the columns report: the SXS simulation number, mass ratio and dimensionless spins spins χ_i, and the maximum value of the EOB/NR unfaithfulness $\bar{F}$, see Fig. 2.

#	id	(q, χ_1, χ_2)	$\max(\bar{F})[\%]$
286	SXS:BBH:0388	$(1.75, 0.8, 0.4)$	0.1073
287	SXS:BBH:1510	$(1.7762, 0.0332, 0.2888)$	0.0525
288	SXS:BBH:0545	$(1.787, 0.0, -0.79)$	0.0672
289	SXS:BBH:1469	$(1.8511, 0.8, 0.669)$	0.1509
290	SXS:BBH:0403	$(1.8808, 0.0, -0.052)$	0.0415
291	SXS:BBH:0555	$(1.89, -0.0, 0.5288)$	0.0458
292	SXS:BBH:1466	$(1.9, 0.7, -0.8)$	0.1664
293	SXS:BBH:0580	$(1.9293, 0.0154, -0.7813)$	0.0718
294	SXS:BBH:0368	$(1.9341, -0.0539, 0.25)$	0.0247
295	SXS:BBH:0530	$(1.9489, 0.0085, 0.5439)$	0.0424
296	SXS:BBH:1478	$(2, 0.8, 0.1263)$	0.1251
297	SXS:BBH:1504	$(2, 0.2458, 0.0787)$	0.0430
298	SXS:BBH:0482	$(2, -0.021, -0.1344)$	0.0380
299	SXS:BBH:2113	$(2, -0.3714, 0.85)$	0.0578
300	SXS:BBH:2126	$(2, 0.3715, -0.85)$	0.0882
301	SXS:BBH:2122	$(2, 0.1286, 0.85)$	0.0632
302	SXS:BBH:0332	$(2, 0.0, 0.8)$	0.0467
303	SXS:BBH:2117	$(2, -0.1287, -0.85)$	0.0603
304	SXS:BBH:0399	$(2, 0.2, 0.4)$	0.0622
305	SXS:BBH:0333	$(2, 0.8, 0.8)$	0.1892
306	SXS:BBH:0410	$(2, 0.6, -0.0)$	0.1252
307	SXS:BBH:0331	$(2, -0.0, -0.8)$	0.0720
308	SXS:BBH:0407	$(2, -0.0, 0.4)$	0.0371
309	SXS:BBH:0375	$(2, -0.0, -0.4)$	0.0502
310	SXS:BBH:0584	$(2, -0.4, -0.4)$	0.0240
311	SXS:BBH:2107	$(2, -0.8712, 0.85)$	0.1517
312	SXS:BBH:0354	$(2, -0.2, 0.4)$	0.0219
313	SXS:BBH:2108	$(2, -0.85, -0.85)$	0.0779
314	SXS:BBH:0334	$(2, -0.8, -0.8)$	0.0306
315	SXS:BBH:0335	$(2, -0.8, 0.8)$	0.1034
316	SXS:BBH:2128	$(2, 0.6, -0.6)$	0.1222
317	SXS:BBH:2121	$(2, 0.0, 0.6)$	0.0395
318	SXS:BBH:0574	$(2, 0.4, 0.4)$	0.0800
319	SXS:BBH:2132	$(2, 0.8713, -0.85)$	0.2481
320	SXS:BBH:2131	$(2, 0.85, 0.85)$	0.3730
321	SXS:BBH:2109	$(2, -0.6, -0.6)$	0.0326
322	SXS:BBH:2119	$(2, 0.0, -0.3)$	0.0455
323	SXS:BBH:0599	$(2, 0.2, 0.0)$	0.0667
324	SXS:BBH:1112	$(2, -0.2, -0.0)$	0.0236
325	SXS:BBH:2118	$(2, 0.0, -0.6)$	0.0594
326	SXS:BBH:2127	$(2, 0.5, 0.5)$	0.0749
327	SXS:BBH:2114	$(2, -0.3, -0.3)$	0.0227
328	SXS:BBH:2115	$(2, -0.3, 0.0)$	0.0199
329	SXS:BBH:2123	$(2, 0.3, -0.3)$	0.0977
330	SXS:BBH:2116	$(2, -0.3, 0.3)$	0.0249
331	SXS:BBH:2124	$(2, 0.3, -0.0)$	0.0839
332	SXS:BBH:2130	$(2, 0.6, 0.6)$	0.0678
333	SXS:BBH:0448	$(2, 0.4, -0.4)$	0.1296
334	SXS:BBH:2120	$(2, 0.0, 0.3)$	0.0356
335	SXS:BBH:2111	$(2, -0.6, 0.6)$	0.0747
336	SXS:BBH:0554	$(2, 0.2, -0.4)$	0.0839

TABLE XII. This table summarizes the SXS NR waveform data in the *validation* set, with mass-ratios $2 \leq q \leq 3$. From left to right, the columns report: the SXS simulation number, mass ratio and dimensionless spins spins χ_i, and the maximum value of the EOB/NR unfaithfulness $\bar{F}$, see Fig. 2.

#	id	(q, χ_1, χ_2)	$\max(\bar{F})[\%]$
337	SXS:BBH:2112	$(2, -0.5, -0.5)$	0.0274
338	SXS:BBH:2129	$(2, 0.6, -0.0)$	0.1237
339	SXS:BBH:0461	$(2, -0.6, 0.0)$	0.0346
340	SXS:BBH:0513	$(2, 0.6, -0.4)$	0.1823
341	SXS:BBH:0387	$(2, -0.6, -0.4)$	0.0236
342	SXS:BBH:2125	$(2, 0.3, 0.3)$	0.0749
343	SXS:BBH:0412	$(2, -0.2, -0.4)$	0.0302
344	SXS:BBH:2110	$(2, -0.6, -0.0)$	0.0538
345	SXS:BBH:1148	$(2, 0.43, 0.51)$	0.0778
346	SXS:BBH:1147	$(2, 0.43, -0.51)$	0.0823
347	SXS:BBH:1494	$(2.208, -0.4741, -0.3891)$	0.0243
348	SXS:BBH:1467	$(2.23, -0.5624, 0.8)$	0.0574
349	SXS:BBH:1459	$(2.2589, 0.7631, 0.8)$	0.1752
350	SXS:BBH:1468	$(2.2675, 0.5148, 0.8)$	0.0563
351	SXS:BBH:0631	$(2.325, -0.1256, -0.3633)$	0.0334
352	SXS:BBH:1453	$(2.3521, 0.8, -0.7843)$	0.3789
353	SXS:BBH:1472	$(2.3657, -0.8, -0.116)$	0.0253
354	SXS:BBH:1512	$(2.4, 0.2393, -0.0)$	0.0599
355	SXS:BBH:1454	$(2.4541, -0.8, -0.7336)$	0.0660
356	SXS:BBH:1462	$(2.6312, -0.8, 0.5107)$	0.0760
357	SXS:BBH:1461	$(2.883, -0.4487, -0.8)$	0.0535
358	SXS:BBH:1484	$(2.9, -0.56, 0.3)$	0.0477
359	SXS:BBH:1387	$(3, 0.47, -0.36)$	0.1006
360	SXS:BBH:1456	$(3, 0.745, 0.7)$	0.0508
361	SXS:BBH:2151	$(3, 0.2314, -0.8493)$	0.1204
362	SXS:BBH:2146	$(3, -0.2312, 0.85)$	0.0615
363	SXS:BBH:2133	$(3, -0.7314, 0.85)$	0.1448
364	SXS:BBH:2145	$(3, -0.2687, -0.8495)$	0.0579
365	SXS:BBH:2152	$(3, 0.2687, 0.85)$	0.0655
366	SXS:BBH:2156	$(3, 0.4, -0.6)$	0.1216
367	SXS:BBH:2135	$(3, -0.6, 0.6)$	0.1004
368	SXS:BBH:2141	$(3, -0.4, 0.6)$	0.0529
369	SXS:BBH:2142	$(3, -0.3, -0.3)$	0.0226
370	SXS:BBH:1152	$(3, 0.7, 0.6)$	0.0175
371	SXS:BBH:1151	$(3, 0.7, 0.6)$	0.0172
372	SXS:BBH:1150	$(3, 0.7, 0.6)$	0.0161
373	SXS:BBH:2139	$(3, -0.5, -0.5)$	0.0331
374	SXS:BBH:1170	$(3, -0.7, -0.6)$	0.0699
375	SXS:BBH:1382	$(3, 0.7, 0.6)$	0.0341
376	SXS:BBH:2157	$(3, 0.4, 0.6)$	0.0230
377	SXS:BBH:2136	$(3, -0.6, -0.6)$	0.0418
378	SXS:BBH:1172	$(3, -0.7, -0.6)$	0.0483
379	SXS:BBH:1171	$(3, -0.7, -0.6)$	0.0512
380	SXS:BBH:2153	$(3, 0.3, -0.3)$	0.0665
381	SXS:BBH:2159	$(3, 0.6, -0.6)$	0.1828
382	SXS:BBH:1175	$(3, -0.7, -0.6)$	0.0484
383	SXS:BBH:1174	$(3, -0.7, -0.6)$	0.0484
384	SXS:BBH:1173	$(3, -0.7, -0.6)$	0.0481
385	SXS:BBH:2140	$(3, -0.4, -0.6)$	0.0374
386	SXS:BBH:2150	$(3, 0.0, 0.6)$	0.0238
387	SXS:BBH:2147	$(3, -0.0, -0.6)$	0.0562

TABLE XIII. This table summarizes the SXS NR waveform data in the *validation* set, with mass-ratios $3 \leq q \leq 5$. From left to right, the columns report: the SXS simulation number, mass ratio and dimensionless spins spins χ_i, and the maximum value of the EOB/NR unfaithfulness $\bar{F}$, see Fig. 2.

#	id	(q, χ_1, χ_2)	$\max(\bar{F})[\%]$
388	SXS:BBH:2138	$(3, -0.6, 0.4)$	0.0745
389	SXS:BBH:2148	$(3, -0.0, -0.3)$	0.0146
390	SXS:BBH:2154	$(3, 0.3, -0.0)$	0.0206
391	SXS:BBH:2134	$(3, -0.6, -0.0)$	0.0433
392	SXS:BBH:2149	$(3, -0.0, 0.3)$	0.0190
393	SXS:BBH:2163	$(3, 0.6, 0.6)$	0.0201
394	SXS:BBH:2143	$(3, -0.3, -0.0)$	0.0178
395	SXS:BBH:2160	$(3, 0.6, -0.4)$	0.1359
396	SXS:BBH:2162	$(3, 0.6, 0.4)$	0.0166
397	SXS:BBH:2144	$(3, -0.3, 0.3)$	0.0275
398	SXS:BBH:2137	$(3, -0.6, -0.4)$	0.0299
399	SXS:BBH:2158	$(3, 0.5, 0.5)$	0.0180
400	SXS:BBH:2155	$(3, 0.3, 0.3)$	0.0228
401	SXS:BBH:2161	$(3, 0.6, 0.0)$	0.0593
402	SXS:BBH:1485	$(3.093, 0.3527, -0.4)$	0.0830
403	SXS:BBH:1446	$(3.1541, -0.8, 0.7766)$	0.1093
404	SXS:BBH:1447	$(3.16, 0.74, 0.8)$	0.0588
405	SXS:BBH:1483	$(3.1656, 0.5607, -0.1941)$	0.0781
406	SXS:BBH:1457	$(3.2452, 0.5449, 0.8)$	0.0180
407	SXS:BBH:0317	$(3.3271, 0.5226, -0.4482)$	0.1074
408	SXS:BBH:1489	$(3.4647, 0.3, -0.1717)$	0.0421
409	SXS:BBH:1452	$(3.6414, 0.8, -0.4265)$	0.2995
410	SXS:BBH:1486	$(3.7227, 0.4272, -0.0335)$	0.0286
411	SXS:BBH:1458	$(3.8, -0.0633, 0.8)$	0.0252
412	SXS:BBH:1932	$(4, -0.8, 0.8)$	0.1056
413	SXS:BBH:1907	$(4, 0.0, 0.8)$	0.0242
414	SXS:BBH:1966	$(4, -0.4, -0.8)$	0.0281
415	SXS:BBH:1962	$(4, -0.4, 0.8)$	0.0686
416	SXS:BBH:1936	$(4, -0.8, -0.8)$	0.1017
417	SXS:BBH:1942	$(4, 0.4, -0.8)$	0.1111
418	SXS:BBH:1911	$(4, -0.0, -0.8)$	0.0653
419	SXS:BBH:1938	$(4, 0.4, 0.8)$	0.0259
420	SXS:BBH:2018	$(4, -0.8, 0.4)$	0.0557
421	SXS:BBH:1937	$(4, 0.4, -0.0)$	0.0204
422	SXS:BBH:1417	$(4, 0.4, 0.5)$	0.0484
423	SXS:BBH:2036	$(4, -0.0, -0.4)$	0.0332
424	SXS:BBH:2013	$(4, 0.0, 0.4)$	0.0137
425	SXS:BBH:1961	$(4, -0.4, 0.0)$	0.0231
426	SXS:BBH:2014	$(4, 0.8, 0.4)$	0.1074
427	SXS:BBH:1418	$(4, -0.4, -0.5)$	0.0644
428	SXS:BBH:1931	$(4, -0.8, 0.0)$	0.0304
429	SXS:BBH:2040	$(4, -0.8, -0.4)$	0.0193
430	SXS:BBH:1451	$(4.0556, 0.3134, -0.8)$	0.0606
431	SXS:BBH:1450	$(4.0673, -0.2835, -0.8)$	0.0349
432	SXS:BBH:1449	$(4.1856, -0.8, -0.3444)$	0.0179
433	SXS:BBH:1434	$(4.3672, 0.8, 0.8)$	0.0352
434	SXS:BBH:1445	$(4.6713, -0.5, 0.8)$	0.1436
435	SXS:BBH:1463	$(5, 0.6131, 0.2406)$	0.1064
436	SXS:BBH:1111	$(5, -0.9, -0.0)$	0.0417
437	SXS:BBH:1428	$(5.5165, -0.8, -0.7)$	0.0660
438	SXS:BBH:1440	$(5.6383, 0.77, 0.3063)$	0.2936

TABLE XIV. This table summarizes the SXS NR waveform data in the *validation* set, with mass-ratios $q \geq 5$. From left to right, the columns report: the SXS simulation number, mass ratio and dimensionless spins spins χ_i, and the maximum value of the EOB/NR unfaithfulness $\bar{F}$, see Fig. 2.

#	id	(q, χ_1, χ_2)	$\max(\bar{F})[\%]$
439	SXS:BBH:1443	$(5.6806, 0.4079, -0.7372)$	0.0220
440	SXS:BBH:1432	$(5.8391, 0.6576, 0.7925)$	0.3098
441	SXS:BBH:1438	$(5.8683, 0.1258, 0.8)$	0.0453
442	SXS:BBH:1444	$(5.937, -0.0631, -0.7582)$	0.0307
443	SXS:BBH:1437	$(6, 0.8, 0.1475)$	0.3598
444	SXS:BBH:1425	$(6.1181, -0.8, 0.6727)$	0.1102
445	SXS:BBH:1436	$(6.2778, 0.0095, -0.8)$	0.0337
446	SXS:BBH:1424	$(6.4641, -0.6566, -0.8)$	0.0487
447	SXS:BBH:1439	$(6.4819, 0.72, -0.3192)$	0.3839
448	SXS:BBH:1464	$(6.5349, -0.0523, -0.3225)$	0.0180
449	SXS:BBH:1442	$(6.5857, -0.71, -0.1785)$	0.0287
450	SXS:BBH:1435	$(6.5891, -0.7893, 0.0673)$	0.0324
451	SXS:BBH:1448	$(6.9451, -0.4814, 0.5248)$	0.0880
452	SXS:BBH:1427	$(7.4107, -0.61, -0.731)$	0.0365
453	SXS:BBH:1429	$(7.7476, -0.2, -0.7788)$	0.0262
454	SXS:BBH:1421	$(7.809, -0.6081, 0.8)$	0.1432
455	SXS:BBH:1422	$(8, -0.8, -0.4588)$	0.0469
456	SXS:BBH:1426	$(8, 0.4839, 0.7479)$	0.1885
457	SXS:BBH:1420	$(8, -0.8, 0.8)$	0.1431
458	SXS:BBH:1419	$(8, -0.8, -0.8)$	0.0666
459	SXS:BBH:1423	$(8, -0.6, -0.7525)$	0.0185
460	SXS:BBH:1430	$(8, 0.2844, -0.7515)$	0.0162
461	SXS:BBH:1441	$(8, 0.6, -0.478)$	0.2715
462	SXS:BBH:1433	$(8, -0.7372, 0.2074)$	0.0509
463	SXS:BBH:1431	$(8, 0.0779, -0.7759)$	0.0278
464	SXS:BBH:1455	$(8, -0.4, 0.0)$	0.0311
465	SXS:BBH:1460	$(8, 0.1237, 0.1087)$	0.0126

where the dot indicate the time derivative. Motivated by the leading-order analytical behavior of each multipole, we introduce the following rescaled multipolar amplitudes $\hat{A}_{\ell m}$:

$$\hat{A}_{22} \equiv A_{22} / \left[\nu \left(1 - \hat{S}\omega_{22}\right)\right], \tag{D6}$$

$$\hat{A}_{21} \equiv A_{21}/\nu, \tag{D7}$$

$$\hat{A}_{33} \equiv A_{33}/\nu, \tag{D8}$$

$$\hat{A}_{32} \equiv A_{32} / \left[\nu \left(1 - \tilde{a}_0 \left(\omega_{32}/2\right)^{1/3}\right)\right], \tag{D9}$$

$$\hat{A}_{44} \equiv A_{44} / \left[\nu \left(1 - \frac{1}{2}\hat{S}\omega_{44}\right)\right], \tag{D10}$$

$$\hat{A}_{43} \equiv A_{43}/\nu, \tag{D11}$$

$$\hat{A}_{42} \equiv A_{42} / \left[\nu \left(1 - \tilde{a}_0 \left(\omega_{42}/2\right)^{1/3}\right)\right]. \tag{D12}$$

Then one defines the time where each (ℓ, m) mode peaks as

$$t^{\rm peak}_{\ell m} \equiv t\left(\max\left[\hat{A}_{\ell m}\right]\right), \tag{D13}$$

and the merger time, that is defined as the peak of the $(2, 2)$ mode, i.e.

$$t^{\rm mrg} \equiv t^{\rm peak}_{22}. \tag{D14}$$

One then defines the time-delay between merger time and the time where each mode peak, as

$$\Delta t_{\ell m} \equiv t^{\rm peak}_{\ell m} - t_{\rm mrg} \tag{D15}$$

For shortness, we denote quantities calculated at a given time using the corresponding superscript, e.g.

$$\hat{A}^{\rm peak}_{\ell m} \equiv \hat{A}_{\ell m}\left(t^{\rm peak}_{\ell m}\right). \tag{D16}$$

Let us now give all details on a mode-by-mode basis.

a. $(\ell, m) = (2, 2)$ *multipole*

We start by describing the template with which $\omega^{\rm mrg}_{22}$ and $\hat{A}^{\rm mrg}_{22}$ were fitted. The same structure is used both for the amplitude and frequency at merger. We here present it explicitly for $\omega^{\rm mrg}_{22}$, w hile the same for $\hat{A}^{\rm mrg}_{22}$ is obtained by suitably changing the coefficient labels. The frequency at merger $\omega^{\rm mrg}_{22}$ is factorized as

$$\omega^{\rm mrg}_{22} = \omega^{\rm mrg_0}_{22}\omega^{\rm orb}_{22}(\nu)\omega^{\hat{S}}_{22}(\hat{S}, X_{12}) \ , \tag{D17}$$

where $\omega^{\rm mrg_0}_{22}$ is the value of the merger frequency obtained from a nonspinning test-particle waveform (see e.g. Table 3 of [45]). The nonspinning ν-dependence is then introduced by fitting the nonspinning data with a template of the form

$$\omega^{\rm orb}_{22}(\nu) = 1 + a^{\omega}_1\nu + a^{\omega}_2\nu^2 \ , \tag{D18}$$

where the coefficients a^{ω}_i are determined using 19 nonspinning SXS waveforms with mass ratios $1 \leq m_1/m_2 \leq 10$. The spin dependence is introduced in two steps: first one accurately fits the spin-dependence of equal-mass data. Then, additional flexibility to incorporate the spinning, unequal-mass data is introduced. More precisely the equal-mass, spin-dependence is obtained with

$$\omega^{\hat{S}}_{22}(\hat{S}, X_{12} = 0) = \frac{1 + b^{\omega_{m_1=m_2}}_1\hat{S} + b^{\omega_{m_1=m_2}}_2\hat{S}^2}{1 + b^{\omega_{m_1=m_2}}_3\hat{S}}, \tag{D19}$$

which is informed by 39 equal-mass, spin-aligned, SXS waveforms. The additional dependence on mass ratio is incorporated substituting into Eq. (D19)

$$b^{\omega_{m_1=m_2}}_i \to \frac{b^{\omega_{m_1=m_2}}_i + c^{\omega}_{i1}X_{12}}{1 + c^{\omega}_{i2}X_{12}} \ , \tag{D20}$$

with $i = \{1, 3\}$. where the additional coefficients c_{ij} are fitted using test-particle data, 77 additional SXS spinning waveforms and 14 additional NR waveforms from BAM. The coefficients are explicitly given in Table XVI.

TABLE XV. This table summarizes the *long-inspiral* SXS NR waveform data. From left to right, columns report: the SXS simulation number, mass ratio and dimensionless spins $\chi_{1,2}$, number of orbits N, eccentricity ϵ and the maximum value of the unfaithfulness $\bar{F}$ computed between: the two highest levels of resolution (L2/L3); between $N = 2$ and $N = 3$ extrapolation to infinity and between EOB and NR. Datasets from SXS:BBH:466 and SXS:BBH:470 are part of the *validation* set, while the indepth study of the other waveforms is left for future work. These waveforms are discussed in Appendix A.

#	id	(q, χ_1, χ_2)	N	ϵ $[10^{-3}]$	$\max(\bar{F}_{\rm L2/L3})[\%]$	$\max(\bar{F}_{\rm N2/N3})[\%]$	$\max(\bar{F})[\%]$
466	SXS:BBH:1412	$(1.63, +0.40, -0.30)$	145.1	0.4450	0.9458	0.0019	0.1292
467	SXS:BBH:1413	$(1.41, +0.50, +0.40)$	145.4	< 1.0	1.5130	0.0021	0.1509
468	SXS:BBH:1414	$(1.83, -0.50, +0.40)$	143.1	< 1.6	1.1665	0.0009	0.1158
469	SXS:BBH:1415	$(1.50, +0.50, +0.50)$	147.7	< 0.043	2.0778	0.0032	0.7218
470	SXS:BBH:1416	$(1.78, -0.40, -0.40)$	139.0	< 1.7	0.7734	0.0003	0.0340
471	SXS:BBH:1385	$(1.23, +0.10, -0.16)$	107.4	< 1.7	0.0907	0.0036	0.4001
472	SXS:BBH:1389	$(1.63, -0.30, +0.16)$	140.4	0.3521	1.0402	0.0034	2.0221
473	SXS:BBH:1390	$(1.42, -0.16, +0.10)$	137.9	0.1895	1.3064	0.0004	3.0090
474	SXS:BBH:1391	$(1.83, -0.33, -0.03)$	142.9	< 1.3	1.0075	0.0016	0.6159
475	SXS:BBH:1392	$(1.51, +0.17, -0.25)$	140.6	0.0548	1.3799	0.0679	3.3064
476	SXS:BBH:1393	$(1.79, -0.00, +0.11)$	146.4	< 1.6	1.0599	0.0007	3.9967

TABLE XVI. Explicit coefficients and their errors for the merger frequency and amplitude fits of the $(2, 2)$ mode. The analytic template of the fit is defined in Eqs. (D17) – (D20).

$\omega_{22}^{\rm mrg_0}$	=	0.273356		$\hat{A}_{22}^{\rm mrg_{=0}}$	=	1.44959	
a_1^{ω}	=	0.84074	± 0.014341	$a_1^{\hat{A}}$	=	-0.041285	± 0.0078878
a_2^{ω}	=	1.6976	± 0.075488	$a_2^{\hat{A}}$	=	1.5971	± 0.041521
$b_1^{\omega_{m_1=m_2}}$	=	-0.42311	± 0.088583	$b_1^{\hat{A}_{m_1=m_2}}$	=	-0.74124	± 0.016178
$b_2^{\omega_{m_1=m_2}}$	=	-0.066699	± 0.042978	$b_2^{\hat{A}_{m_1=m_2}}$	=	-0.088705	± 0.0081611
$b_3^{\omega_{m_1=m_2}}$	=	-0.83053	± 0.084516	$b_3^{\hat{A}_{m_1=m_2}}$	=	-1.0939	± 0.015318
c_{11}^{ω}	=	0.15873	± 0.1103	$c_{11}^{\hat{A}}$	=	0.44467	± 0.037352
c_{12}^{ω}	=	-0.43361	± 0.2393	$c_{12}^{\hat{A}}$	=	-0.32543	± 0.081211
c_{21}^{ω}	=	0.60589	± 0.076215	$c_{31}^{\hat{A}}$	=	0.45828	± 0.066062
c_{22}^{ω}	=	-0.71383	± 0.096828	$c_{32}^{\hat{A}}$	=	-0.21245	± 0.080254

b. $(\ell, m) = (2, 1)$ *multipole*

The procedure followed for the subdominant modes is similar to what is done for the $(2, 2)$. There are however some differences. First of all, the peak time shift $\Delta t_{\ell m}$ is also fitted to NR simulations. Second, basing ourselves to the analytical behavior of the multipolar waveform, we have decided to use different factorizations and different variables to model each mode. For example, the $(2, 1)$ multipole (and every m-odd mode) vanishes because of symmetry in the equal-mass equal-spin case. This has brought us to consider the following factorization for $\hat{A}_{21}^{\rm peak}$, which is written as

$$\hat{A}_{21}^{\rm peak} = \hat{A}_{21}^{\rm peak_0} X_{12} \hat{A}_{21}^{\rm orb}(\nu) + \hat{A}_{21}^{\rm Spin}\left(\bar{S}, \nu\right). \tag{D21}$$

where $\hat{A}_{21}^{\rm peak_0}$ is the peak amplitude in the test-particle limit. The factor $\hat{A}_{21}^{\rm orb}$ is informed by non-spinning waveforms and is fitted with the template

$$\hat{A}_{21}^{\rm orb}(\nu) = \frac{1 + a_1^{\hat{A}_{21}}\nu + a_2^{\hat{A}_{21}}\nu^2}{1 + a_3^{\hat{A}_{21}}\nu}\,. \tag{D22}$$

The spin dependence is first captured in the test-particle limit with the function

$$\hat{A}_{21}^{\rm Spin}(\bar{S}, \nu = 0) = \frac{1 + b_1^{\hat{A}^0_{21}}\bar{S} + b_2^{\hat{A}^0_{21}}\bar{S}^2}{1 + b_3^{\hat{A}^0_{21}}\bar{S}}\,. \tag{D23}$$

The ν-dependence is then modeled via the replacement

$$b_i^{\hat{A}^0_{21}} \to b_i^{\hat{A}^0_{21}} + c_{i1}^{\hat{A}_{21}}\nu + c_{i2}^{\hat{A}_{21}}\nu^2\,, \tag{D24}$$

with $i = \{1, 2, 3\}$.

The gravitational wave frequency ω_{21} is instead factorized as

$$\omega_{21}^{\rm peak} = \omega_{21}^{\rm peak_0}\omega_{21}^{\rm orb}(\nu)\omega_{21}^{\rm Spin}\left(\hat{S}, \nu\right), \tag{D25}$$

where the ν-dependence of the nonspinning part is modeled as

$$\omega_{21}^{\rm orb}(\nu) = 1 + a_1^{\omega_{21}}\nu + a_2^{\omega_{21}}\nu^2 \ . \tag{D26}$$

The spin dependence is fitted first in the test-particle limit

$$\omega_{21}^{\rm Spin}\left(\hat{S}, \nu = 0\right) = 1 + b_1^{\omega_{21}^0}\hat{S} + b_2^{\omega_{21}^0}\hat{S}^2 \ , \tag{D27}$$

and then extended to a general mass ratio via the replacement

$$b_i^{\omega_{21}^0} \to b_i^{\omega_{21}^0} + c_i^{\omega_{21}}\nu \ , \tag{D28}$$

with $i = \{1, 2\}$.

Finally, to represent analytically the time-delay Δt_{21} we use

$$\Delta t_{21} = \Delta t_{21}^{\rm orb}(\nu)\Delta t_{21}^{\rm spin}\left(\bar{S}, X_{12}\right) \ , \tag{D29}$$

where the orbital behavior is factorized into two separate parts before fitting with

$$\begin{aligned}\Delta t_{21}^{\rm orb}(\nu) = &\left(\Delta t_{21}^0(1-4\nu) + \Delta t_{21}^{\nu=1/4}4\nu\right) \\ &\times \left(1 + a_1^{\Delta t_{21}}\nu\sqrt{1-4\nu}\right) \ .\end{aligned} \tag{D30}$$

The factor $\Delta t_{21}^{\nu=1/4}$ is obtained by fitting a 2nd-order polynomial, in $\hat{a}_0$ to the equal-mass waveforms. Δt_{21}^0 is the test-particle value. The equal-mass spin behavior is fitted with

$$\Delta t_{21}^{\rm spin}\left(\bar{S}, X_{12} = 0\right) = 1 + b_1^{\Delta t_{21}^{\nu=1/4}}\hat{a}_0 + b_2^{\Delta t_{21}^{\nu=1/4}}\hat{a}_0^2 \ , \tag{D31}$$

while the comparable mass case is extrapolated using

$$b_1^{\Delta t_{21}^{\nu=1/4}} \to \frac{b_1^{\Delta t_{21}^0} + c_{i1}^{\Delta t_{21}}X_{12}}{1 + c_{i2}^{\Delta t_{21}}X_{12}} \ , \tag{D32}$$

with $i = \{1, 2\}$. The outcome of the fit, with the explicit values of all coefficients, id found in Table XVII.

c. $(\ell, m) = (3, 3)$ *multipole*

For this mode, the peak amplitude is written as the sum of two terms

$$\hat{A}_{33}^{\rm peak} = \hat{A}_{33}^{\rm peak_0}X_{12}\hat{A}_{33}^{\rm orb}(\nu) + \hat{A}_{33}^{\rm Spin}(\tilde{a}_{12}, \nu) \ , \tag{D33}$$

where $\hat{A}_{33}^{\rm peak_0}$ is the peak amplitude in the test particle limit. The orbital term is modeled as

$$\hat{A}_{33}^{\rm orb}(\nu) = \frac{1 + a_1^{\hat{A}_{33}}\nu + a_2^{\hat{A}_{33}}\nu^2}{1 + a_3^{\hat{A}_{33}}\nu} \ . \tag{D34}$$

The spin dependence is first fitted in the test-particle limit using

$$\hat{A}_{33}^{\rm Spin}(\tilde{a}_{12}, \nu = 0) = \frac{b_1^{\hat{A}_{33}^0}\tilde{a}_{12}}{1 + b_2^{\hat{A}_{33}^0}\tilde{a}_{12}} \ , \tag{D35}$$

and then extended to comparable masses via the replacements

$$b_1^{\hat{A}_{33}^0} \to \frac{b_1^{\hat{A}_{33}^0} + c_{11}^{\hat{A}_{33}}\nu}{1 + c_{12}^{\hat{A}_{33}}\nu + c_{13}^{\hat{A}_{33}}\nu^2} \ , \tag{D36}$$

$$b_2^{\hat{A}_{33}^0} \to \frac{b_2^{\hat{A}_{33}^0} + c_{21}^{\hat{A}_{33}}\nu}{1 + c_{22}^{\hat{A}_{33}}\nu + c_{23}^{\hat{A}_{33}}\nu^2} \ . \tag{D37}$$

The istantaneous frequency ω_{33} is factorized as

$$\omega_{33}^{\rm peak} = \omega_{33}^{\rm peak_0}\omega_{33}^{\rm orb}(\nu)\omega_{33}^{\rm Spin}\left(\hat{S}, \nu\right) \ , \tag{D38}$$

where

$$\omega_{33}^{\rm orb}(\nu) = 1 + a_1^{\omega_{33}}\nu + a_2^{\omega_{33}}\nu^2 \ . \tag{D39}$$

The test-particle spin factor is given by

$$\omega_{33}^{\rm Spin}\left(\hat{S}, \nu = 0\right) = \frac{1 + b_1^{\omega_{33}^0}\hat{S} + b_2^{\omega_{33}^0}\hat{S}^2}{1 + b_3^{\omega_{33}^0}\hat{S}} \ , \tag{D40}$$

while the general spin-dependence stems from the replacement

$$b_i^{\omega_{33}^0} \to \frac{b_i^{\omega_{33}^0} + c_{i1}^{\omega_{33}}\nu}{1 + c_{i2}^{\omega_{33}}\nu} \ , \tag{D41}$$

with $i = \{1, 3\}$.

To describe Δt_{33} we start from the expression

$$\Delta t_{33} = \Delta t_{33}^0\Delta t_{33}^{\rm orb}(\nu)\Delta t_{33}^{\rm spin}\left(\hat{S}, \nu\right) \ , \tag{D42}$$

with

$$\Delta t_{33}^{\rm orb}(\nu) = 1 + a_1^{\Delta t_{33}}\nu + a_2^{\Delta t_{33}}\nu^2 \ , \tag{D43}$$

$$\Delta t_{33}^{\rm spin}\left(\hat{S}, \nu = 0\right) = \frac{1 + b_1^{\Delta t_{33}^0}\hat{S} + b_2^{\Delta t_{33}^0}\hat{S}^2}{1 + b_3^{\Delta t_{33}^0}\hat{S}} \ . \tag{D44}$$

The spin-dependence is obtained from the replacement

$$b_1^{\Delta t_{33}^0} \to \frac{b_1^{\Delta t_{33}^0} + c_{i1}^{\Delta t_{33}}\nu}{1 + c_{i2}^{\Delta t_{33}}\nu} \ , \tag{D45}$$

with $i = \{1, 2, 3\}$. The explicit values of the fit coefficients are listed in Table XVIII.

d. $(\ell, m) = (3, 2)$ *multipole*

The peak amplitude of the $(3, 2)$ mode is fitted with a factorized template of the form

$$\hat{A}_{32}^{\rm peak} = \hat{A}_{32}^{\rm peak_0}\left(1 - 3\nu\right)\hat{A}_{32}^{\rm orb}\left(\nu\right)\hat{A}_{32}^{\rm Spin}\left(\bar{S}, \nu\right) \ , \tag{D46}$$

where $\hat{A}_{32}^{\rm peak_0}$ is the peak amplitude of the mode in the test-particle limit. The factor $\hat{A}_{32}^{\rm orb}$ is informed by nonspinning waveforms and is fitted with the template

$$\hat{A}_{32}^{\rm orb}(\nu) = \frac{1 + a_1^{\hat{A}_{32}}\nu + a_2^{\hat{A}_{32}}\nu^2}{1 + a_3^{\hat{A}_{32}}\nu} \ . \tag{D47}$$

TABLE XVII. Explicit coefficients of the fits of $\hat{A}_{21}^{\rm peak}$, $\omega_{21}^{\rm peak}$ and Δt_{21}.

$\hat{A}_{21}^{\rm peak_0}$	=	0.523878	$\omega_{21}^{\rm peak_0}$	=	0.290643	Δt_{21}^{0}	=	11.75925
$a_1^{\hat{A}_{21}}$	=	3.33622	$a_1^{\omega_{21}}$	=	−0.563075	$\Delta t_{21}^{\nu=1/4}$	=	6.6264
$a_2^{\hat{A}_{21}}$	=	3.47085	$a_2^{\omega_{21}}$	=	3.28677	$a_1^{\Delta t_{21}}$	=	−2.0728
$a_3^{\hat{A}_{21}}$	=	4.76236						
$b_1^{\hat{A}_{21}^0}$	=	−0.428186	$b_1^{\omega_{21}^0}$	=	0.179639	$b_1^{\Delta t_{21}^0}$	=	0.0472289
$b_2^{\hat{A}_{21}^0}$	=	−0.335659	$b_2^{\omega_{21}^0}$	=	−0.302122	$b_2^{\Delta t_{21}^0}$	=	0.115583
$b_3^{\hat{A}_{21}^0}$	=	0.828923						
$c_{11}^{\hat{A}_{21}}$	=	0.891139	$c_1^{\omega_{21}}$	=	−1.20684	$c_{11}^{\Delta t_{21}}$	=	−1976.13
$c_{12}^{\hat{A}_{21}}$	=	−5.191702	$c_2^{\omega_{21}}$	=	0.425645	$c_{12}^{\Delta t_{21}}$	=	3719.88
$c_{21}^{\hat{A}_{21}}$	=	3.480139				$c_{21}^{\Delta t_{21}}$	=	−2545.41
$c_{22}^{\hat{A}_{21}}$	=	10.237782				$c_{22}^{\Delta t_{21}}$	=	5277.62
$c_{31}^{\hat{A}_{21}}$	=	−13.867475						
$c_{32}^{\hat{A}_{21}}$	=	10.525510						

TABLE XVIII. Explicit coefficients of the fits of $\hat{A}_{33}^{\rm peak}$, $\omega_{33}^{\rm peak}$ and Δt_{33}.

$\hat{A}_{33}^{\rm peak_0}$	=	0.566017	$\omega_{33}^{\rm peak_0}$	=	0.454128	Δt_{33}^{0}	=	3.42593
$a_1^{\hat{A}_{33}}$	=	−0.22523	$a_1^{\omega_{33}}$	=	1.08224	$a_1^{\Delta t_{33}}$	=	0.183349
$a_2^{\hat{A}_{33}}$	=	3.0569	$a_2^{\omega_{33}}$	=	2.59333	$a_2^{\Delta t_{33}}$	=	4.22361
$a_3^{\hat{A}_{33}}$	=	−0.396851						
$b_1^{\hat{A}_{33}^0}$	=	0.100069	$b_1^{\omega_{33}^0}$	=	−0.406161	$b_1^{\Delta t_{33}^0}$	=	−0.49791
$b_2^{\hat{A}_{33}^0}$	=	−0.455859	$b_2^{\omega_{33}^0}$	=	−0.0647944	$b_2^{\Delta t_{33}^0}$	=	−0.18754
			$b_3^{\omega_{33}^0}$	=	−0.748126	$b_3^{\Delta t_{33}^0}$	=	−1.07291
$c_{11}^{\hat{A}_{33}}$	=	−0.401156	$c_{11}^{\omega_{33}}$	=	0.85777	$c_{11}^{\Delta t_{33}}$	=	−1.9478
$c_{12}^{\hat{A}_{33}}$	=	−0.141551	$c_{12}^{\omega_{33}}$	=	−0.70066	$c_{12}^{\Delta t_{33}}$	=	13.9828
$c_{13}^{\hat{A}_{33}}$	=	−15.4949	$c_{31}^{\omega_{33}}$	=	2.97025	$c_{21}^{\Delta t_{33}}$	=	1.25084
$c_{21}^{\hat{A}_{33}}$	=	1.84962	$c_{32}^{\omega_{33}}$	=	−3.96242	$c_{22}^{\Delta t_{33}}$	=	−3.41811
$c_{22}^{\hat{A}_{33}}$	=	−2.03512				$c_{31}^{\Delta t_{33}}$	=	−1043.15
$c_{23}^{\hat{A}_{33}}$	=	−4.92334				$c_{32}^{\Delta t_{33}}$	=	1033.85

The spin dependence is first captured for the test-particle limit with the function

$$\hat{A}_{32}^{\rm Spin}(\bar{S},\nu=0)=\frac{1+b_1^{\hat{A}_{32}^0}\tilde{a}_0}{1+b_2^{\hat{A}_{32}^0}\tilde{a}_0}\ , \tag{D48}$$

while the ν-dependence enters via the replacement

$$b_i^{\hat{A}_{32}^0}\to\frac{b_i^{\hat{A}_{32}^0}+c_{i1}^{\hat{A}_{32}}\nu+c_{i2}^{\hat{A}_{32}}\nu^2}{1+c_{i3}^{\hat{A}_{32}}\nu+c_{i4}^{\hat{A}_{32}}\nu^2}\ , \tag{D49}$$

with $i=\{1,2\}$.

The instantaneous frequency ω_{32} mode is factorized as

$$\omega_{32}^{\rm peak}=\omega_{32}^{\rm peak_0}\omega_{32}^{\rm orb}(\nu)\omega_{32}^{\rm Spin}\left(\tilde{a}_0,\nu\right)\ . \tag{D50}$$

The orbital dependence is modeled as

$$\omega_{32}^{\rm orb}(\nu)=\frac{1+a_1^{\omega_{32}}\nu+a_2^{\omega_{32}}\nu^2}{1+a_3^{\omega_{32}}\nu+a_4^{\omega_{32}}\nu^2}\ . \tag{D51}$$

The spin dependence is fitted first for the equal-mass case

$$\omega_{32}^{\rm Spin}\left(\tilde{a}_0,\nu=1/4\right)=\frac{1+b_1^{\omega_{32}^{\nu=1/4}}\tilde{a}_0+b_2^{\omega_{32}^{\nu=1/4}}\tilde{a}_0^2}{1+b_3^{\omega_{32}^{\nu=1/4}}\tilde{a}_0}\ , \tag{D52}$$

while the additional dependence on the mass ratio enters via the replacements

$$b_i^{\omega_{32}^0}\to\frac{b_i^{\omega_{32}^{\nu=1/4}}+c_{i1}^{\omega_{32}}X_{12}+c_{i2}^{\omega_{32}}X_{12}^2}{1+c_{i3}^{\omega_{32}}X_{12}}\ , \tag{D53}$$

with $i=\{1,2\}$. The coefficients of $\hat{A}_{32}^{\rm peak}$ and $\omega_{32}^{\rm peak}$ are explicitly listed in Table XXIII.

Moving to Δt_{32}, it is given by

$$\Delta t_{32}=\Delta t_{32}^0\Delta t_{32}^{\rm orb}(\nu)\Delta t_{32}^{\rm spin}\left(\hat{S},\nu\right)\ , \tag{D54}$$

where the orbital behavior is fitted with

$$\Delta t_{32}^{\rm orb}(\nu)=\frac{1+a_1^{\Delta t_{32}}\nu+a_2^{\Delta t_{32}}\nu^2}{1+a_3^{\Delta t_{32}}\nu+a_4^{\Delta t_{32}}\nu^2}\ . \tag{D55}$$

The spin behavior is more complicated than the corresponding term of other modes. This is separated into two sectors, as

$$\Delta t_{32}^{\rm spin}\left(\hat{S},\nu\right) = \Delta t_{32}^{{\rm spin}_{\nu>1/5}}\left(\hat{S},\nu\right)\Theta\left(\nu-1/5\right) + \Delta t_{32}^{{\rm spin}_{\nu\leq 1/5}}\left(\hat{S},\nu\right)\left[1-\Theta\left(\nu-1/5\right)\right] , \tag{D56}$$

where Θ denotes the Heaviside step function. In the $\nu > 1/5$ regime the fit is first done to the equal-mass case

$$\Delta t_{32}^{{\rm spin}_{\nu>1/5}}\left(\hat{S},\nu=1/4\right) = \frac{1+b_1^{\Delta t_{32}^{\nu=1/4}}\hat{S}+b_2^{\Delta t_{32}^{\nu=1/4}}\hat{S}^2}{1+b_3^{\Delta t_{32}^{\nu=1/4}}\hat{S}} . \tag{D57}$$

Then it is extrapolated following

$$b_i^{\Delta t_{32}^{\nu=1/4}} \to \frac{b_1^{\Delta t_{32}^{\nu=1/4}}+c_{i1}^{\Delta t_{32}}X_{12}+c_{i2}^{\Delta t_{32}}X_{12}^2+c_{i3}^{\Delta t_{32}}X_{12}^3}{1+c_{i4}^{\Delta t_{43}}X_{12}+c_{i5}^{\Delta t_{43}}X_{12}^2} , \tag{D58}$$

with $i=\{1,2,3\}$.

In the $\nu \leq 1/5$ regime the fit is first done to the equal-mass case

$$\Delta t_{32}^{{\rm spin}_{\nu\leq 1/5}}\left(\hat{S},\nu=0\right) = \frac{1+b_1^{\Delta t_{32}^{0}}\hat{S}+b_2^{\Delta t_{32}^{0}}\hat{S}^2}{1+b_3^{\Delta t_{32}^{0}}\hat{S}} . \tag{D59}$$

Then it is extrapolated following

$$b_i^{\Delta t_{32}^{0}} \to \frac{b_1^{\Delta t_{32}^{0}}+c_{i1}^{\Delta t_{32}}\nu+c_{i2}^{\Delta t_{32}}\nu^2+c_{i3}^{\Delta t_{32}}\nu^3}{1+c_{i4}^{\Delta t_{32}}\nu+c_{i5}^{\Delta t_{32}}\nu^2} , \tag{D60}$$

with $i=\{1,2,3\}$. The coefficients appearing in Δt_{32} are shown in Table XX.

e. $(\ell,m)=(4,4)$ *multipole*

The peak amplitude of the $(4,4)$ mode is fitted with

$$\hat{A}_{44}^{\rm peak} = \hat{A}_{44}^{{\rm peak}_0}\left(1-3\nu\right)\hat{A}_{44}^{\rm orb}\left(\nu\right)\hat{A}_{44}^{\rm Spin}\left(\hat{S},\nu\right) , \tag{D61}$$

where $\hat{A}_{44}^{{\rm peak}_0}$ is the peak amplitude of the mode in the test-particle limit. The factor $\hat{A}_{44}^{\rm orb}$ is informed by non-spinning waveforms and is fitted with the template

$$\hat{A}_{44}^{\rm orb}(\nu) = \frac{1+a_1^{\hat{A}_{44}}\nu+a_2^{\hat{A}_{44}}\nu^2}{1+a_3^{\hat{A}_{44}}\nu} . \tag{D62}$$

The spin dependence is first captured for the test-particle limit with the function

$$\hat{A}_{44}^{\rm Spin}(\hat{S},\nu=0) = \frac{1+b_1^{\hat{A}_{44}^0}\hat{S}+b_2^{\hat{A}_{44}^0}\hat{S}^2}{1+b_3^{\hat{A}_{44}^0}\hat{S}} , \tag{D63}$$

TABLE XIX. Explicit coefficients of the fits of $\hat{A}_{32}^{\rm peak}$ and $\omega_{32}^{\rm peak}$.

$\hat{A}_{32}^{{\rm peak}_0}$	=	0.199019	$\omega_{32}^{{\rm peak}_0}$	=	0.451607
$a_1^{\hat{A}_{32}}$	=	−6.06831	$a_1^{\omega_{32}}$	=	−9.13525
$a_2^{\hat{A}_{32}}$	=	10.7505	$a_2^{\omega_{32}}$	=	21.488
$a_3^{\hat{A}_{32}}$	=	−3.68883	$a_3^{\omega_{32}}$	=	−8.81384
			$a_4^{\omega_{32}}$	=	20.0595
$b_1^{\hat{A}_{32}^0}$	=	−0.258378	$b_1^{\omega_{32}^{\nu=1/4}}$	=	−0.458126
$b_2^{\hat{A}_{32}^0}$	=	0.679163	$b_2^{\omega_{32}^{\nu=1/4}}$	=	0.0474616
			$b_3^{\omega_{32}^{\nu=1/4}}$	=	−0.486049
$c_{11}^{\hat{A}_{32}}$	=	4.36263	$c_{11}^{\omega_{32}}$	=	3.25319
$c_{12}^{\hat{A}_{32}}$	=	−12.5897	$c_{12}^{\omega_{32}}$	=	0.535555
$c_{13}^{\hat{A}_{32}}$	=	−7.73233	$c_{13}^{\omega_{32}}$	=	−8.07905
$c_{14}^{\hat{A}_{32}}$	=	16.2082	$c_{21}^{\omega_{32}}$	=	1.00066
$c_{21}^{\hat{A}_{32}}$	=	3.04724	$c_{22}^{\omega_{32}}$	=	−1.1333
$c_{22}^{\hat{A}_{32}}$	=	46.5711	$c_{23}^{\omega_{32}}$	=	0.601572
$c_{23}^{\hat{A}_{32}}$	=	2.10475			
$c_{24}^{\hat{A}_{32}}$	=	56.9136			

and then extended in the comparable mass region of the parameter space through

$$b_i^{\hat{A}_{44}^0} \to \frac{b_i^{\hat{A}_{44}^0}+c_{i1}^{\hat{A}_{44}}\nu+c_{i2}^{\hat{A}_{44}}\nu^2}{1+c_{i3}^{\hat{A}_{44}}\nu+c_{i4}^{\hat{A}_{44}}\nu^2} , \text{ with } i=\{1,2,3\} . \tag{D64}$$

The peak frequency ω_{44} is factorized as

$$\omega_{44}^{\rm peak} = \omega_{44}^{{\rm peak}_0}\omega_{44}^{\rm orb}(\nu)\omega_{44}^{\rm Spin}\left(\hat{S},\nu\right) . \tag{D65}$$

The orbital dependence is modeled through

$$\omega_{44}^{\rm orb}(\nu) = \frac{1+a_1^{\omega_{44}}\nu+a_2^{\omega_{44}}\nu^2}{1+a_3^{\omega_{44}}\nu+a_4^{\omega_{44}}\nu^2} . \tag{D66}$$

The spin dependence is fitted first for the test-particle limit as

$$\omega_{44}^{\rm Spin}\left(\hat{S},\nu=0\right) = \frac{1+b_1^{\omega_{44}^0}\hat{S}+b_2^{\omega_{44}^0}\hat{S}^2+b_3^{\omega_{44}^0}\hat{S}^3}{1+b_4^{\omega_{33}^0}\hat{S}} . \tag{D67}$$

The spin dependence in the comparable mass region of the parameter space is modeled through

$$b_i^{\omega_{44}^0} \to \frac{b_i^{\omega_{44}^0}+c_{i1}^{\omega_{44}}\nu+c_{i2}^{\omega_{44}}\nu^2}{1+c_{i3}^{\omega_{44}}\nu+c_{i4}^{\omega_{44}}\nu^2} , \tag{D68}$$

with $i=\{1,2,3,4\}$.

We fit Δt_{44} in a factorized form as

$$\Delta t_{44} = \Delta t_{44}^0\Delta t_{44}^{\rm orb}(\nu)\Delta t_{44}^{\rm spin}\left(\hat{S},X_{12}\right) . \tag{D69}$$

The orbital behavior is fitted with

$$\Delta t_{44}^{\rm orb}(\nu) = \frac{1+a_1^{\Delta t_{44}}\nu+a_2^{\Delta t_{44}}\nu^2}{1+a_3^{\Delta t_{44}}\nu+a_4^{\Delta t_{44}}\nu^2} , \tag{D70}$$

TABLE XX. Explicit coefficients of Δt_{32}.

Δt^0_{32}	=	9.16665	$c_{11}^{\Delta t^\nu_{32}}$	=	−0.037634	$c_{11}^{\Delta t^{X_{12}}_{32}}$	=	2.497188
$a_1^{\Delta t_{32}}$	=	−11.3497	$c_{12}^{\Delta t^\nu_{32}}$	=	12.456704	$c_{12}^{\Delta t^{X_{12}}_{32}}$	=	−7.532596
$a_2^{\Delta t_{32}}$	=	32.9144	$c_{13}^{\Delta t^\nu_{32}}$	=	2.670868	$c_{13}^{\Delta t^{X_{12}}_{32}}$	=	4.645986
$a_3^{\Delta t_{32}}$	=	−8.36579	$c_{14}^{\Delta t^\nu_{32}}$	=	−12.255859	$c_{14}^{\Delta t^{X_{12}}_{32}}$	=	−3.652524
$a_4^{\Delta t_{32}}$	=	20.1017	$c_{15}^{\Delta t^\nu_{32}}$	=	37.843505	$c_{15}^{\Delta t^{X_{12}}_{32}}$	=	3.398687
$b_1^{\Delta t^0_{32}}$	=	−0.34161	$c_{21}^{\Delta t^\nu_{32}}$	=	−25.058475	$c_{21}^{\Delta t^{X_{12}}_{32}}$	=	7.054185
$b_2^{\Delta t^0_{32}}$	=	−0.46107	$c_{22}^{\Delta t^\nu_{32}}$	=	449.470722	$c_{22}^{\Delta t^{X_{12}}_{32}}$	=	−12.260185
$b_3^{\Delta t^0_{32}}$	=	0.34744	$c_{23}^{\Delta t^\nu_{32}}$	=	−1413.508735	$c_{23}^{\Delta t^{X_{12}}_{32}}$	=	5.724802
$b_1^{\Delta t^{\nu=1/4}_{32}}$	=	0.15477	$c_{24}^{\Delta t^\nu_{32}}$	=	−11.852596	$c_{24}^{\Delta t^{X_{12}}_{32}}$	=	−3.242611
$b_2^{\Delta t^{\nu=1/4}_{32}}$	=	−0.755639	$c_{25}^{\Delta t^\nu_{32}}$	=	41.348059	$c_{25}^{\Delta t^{X_{12}}_{32}}$	=	2.714232
$b_3^{\Delta t^{\nu=1/4}_{32}}$	=	0.21816	$c_{31}^{\Delta t^\nu_{32}}$	=	−5.650710	$c_{31}^{\Delta t^{X_{12}}_{32}}$	=	2.614565
			$c_{32}^{\Delta t^\nu_{32}}$	=	−9.567484	$c_{32}^{\Delta t^{X_{12}}_{32}}$	=	−9.507583
			$c_{33}^{\Delta t^\nu_{32}}$	=	173.182999	$c_{33}^{\Delta t^{X_{12}}_{32}}$	=	7.321586
			$c_{34}^{\Delta t^\nu_{32}}$	=	−10.938605	$c_{34}^{\Delta t^{X_{12}}_{32}}$	=	−3.937568
			$c_{35}^{\Delta t^\nu_{32}}$	=	35.670656	$c_{35}^{\Delta t^{X_{12}}_{32}}$	=	4.584970

while the spinning one is first fitted to equal mass simulations as

$$\Delta t_{44}^{\rm spin}\left(\hat{S}, X_{12}=0\right) = \frac{1+b_1^{\Delta t_{44}^{\nu=1/4}}\hat{S}}{1+b_2^{\Delta t_{44}^{\nu=1/4}}\hat{S}} \ . \tag{D71}$$

The general ν-dependence enters via the replacement

$$b_i^{\Delta t_{44}^{\nu=1/4}} \to b_i^{\Delta t_{44}^{\nu=1/4}} + c_{i1}^{\Delta t_{44}} X_{12} + c_{i2}^{\Delta t_{44}} X_{12}^2 \ , \tag{D72}$$

with $i=\{1,2\}$. The explicit values of the fit coefficients can be found in Table XXI.

f. $(\ell, m) = (4, 3)$ *multipole*

The peak amplitude of the $(4,3)$ mode is fitted with

$$\hat{A}_{43}^{\rm peak} = \hat{A}_{43}^{\rm peak_0} X_{12}\,(1-2\nu)\,\hat{A}_{43}^{\rm orb}\,(\nu) + \hat{A}_{43}^{\rm Spin}\,(\tilde{a}_0,\nu) \ , \tag{D73}$$

where $\hat{A}_{43}^{\rm peak_0}$ is the peak amplitude of the mode in the test-particle limit. The factor $\hat{A}_{43}^{\rm orb}$ is informed by non-spinning waveforms and is fitted with the template

$$\hat{A}_{43}^{\rm orb}(\nu) = \frac{1+a_1^{\hat{A}_{43}}\nu + a_2^{\hat{A}_{43}}\nu^2}{1+a_3^{\hat{A}_{43}}\nu} \ . \tag{D74}$$

The spin dependence is first captured for the test-particle limit with the function

$$\hat{A}_{43}^{\rm Spin}(\tilde{a}_0,\nu=0) = \frac{1+b_1^{\hat{A}^0_{43}}\tilde{a}_0 + b_2^{\hat{A}^0_{43}}\tilde{a}_0^2}{1+b_3^{\hat{A}^0_{43}}\tilde{a}_0} \ . \tag{D75}$$

The spin dependence in the comparable mass region of the parameter space is modeled through

$$b_i^{\hat{A}^0_{43}} \to \frac{b_i^{\hat{A}^0_{43}} + c_{i1}^{\hat{A}_{43}}\nu}{1+c_{i2}^{\hat{A}_{43}}\nu + c_{i3}^{\hat{A}_{43}}\nu^2} \ , \tag{D76}$$

with $i=\{1,2,3\}$. For the equal mass case however a special fit is made to accurately capture the correct behavior, i.e.

$$\hat{A}_{43}^{\rm peak}\left(\tilde{a}_{12}, \nu=\frac{1}{4}\right) = \frac{b_1^{\hat{A}_{43}^{\nu=1/4}}\tilde{a}_{12} + b_2^{\hat{A}_{43}^{\nu=1/4}}\tilde{a}_{12}^2}{1+b_3^{\hat{A}_{43}^{\nu=1/4}}\tilde{a}_{12}} \ . \tag{D77}$$

The istantaneous frequency at peak $\omega_{43}^{\rm peak}$ is factorized as

$$\omega_{43}^{\rm peak} = \omega_{43}^{\rm peak_0}\omega_{43}^{\rm orb}(\nu)\omega_{43}^{\rm Spin}\left(\hat{S},\nu\right), \tag{D78}$$

where the orbital factor is modeled as

$$\omega_{43}^{\rm orb}(\nu) = \frac{1+a_1^{\omega_{43}}\nu + a_2^{\omega_{43}}\nu^2}{1+a_3^{\omega_{43}}\nu + a_4^{\omega_{43}}\nu^2} \ . \tag{D79}$$

The spin dependence is fitted first for the test-particle case

$$\omega_{43}^{\rm Spin}\left(\hat{S},\nu=0\right) = \frac{1+b_1^{\omega^0_{43}}\hat{S} + b_2^{\omega^0_{43}}\hat{S}^2}{1+b_3^{\omega^0_{43}}\hat{S}} \ , \tag{D80}$$

and then extended to other regions of the parameter space with

$$b_i^{\omega^0_{43}} \to \frac{b_i^{\omega^0_{43}} + c_{i1}^{\omega_{43}}\nu + c_{i2}^{\omega_{43}}\nu^2}{1+c_{i3}^{\omega_{43}}\nu} \ , \tag{D81}$$

TABLE XXI. Explicit coefficients of the fits of $\hat{A}_{44}^{\rm peak}$, $\omega_{44}^{\rm peak}$ and Δt_{44}.

$\hat{A}_{44}^{\rm peak_0}$	=	0.276618	$\omega_{44}^{\rm peak_0}$	=	0.635659	Δt_{44}^0	=	5.27778
$a_1^{\hat{A}_{44}}$	=	−3.7082	$a_1^{\omega_{44}}$	=	−0.964614	$a_1^{\Delta t_{44}}$	=	−8.35574
$a_2^{\hat{A}_{44}}$	=	0.280906	$a_2^{\omega_{44}}$	=	−11.1828	$a_2^{\Delta t_{44}}$	=	17.5288
$a_3^{\hat{A}_{44}}$	=	−3.71276	$a_3^{\omega_{44}}$	=	−2.08471	$a_3^{\Delta t_{44}}$	=	−6.50259
			$a_4^{\omega_{44}}$	=	−6.89287	$a_4^{\Delta t_{44}}$	=	10.1575
$b_1^{\hat{A}_{44}^0}$	=	−0.316647	$b_1^{\omega_{44}^0}$	=	−0.445192	$b_1^{\Delta t_{44}^{\nu=1/4}}$	=	0.00159701
$b_2^{\hat{A}_{44}^0}$	=	−0.062423	$b_2^{\omega_{44}^0}$	=	−0.0985658	$b_2^{\Delta t_{44}^{\nu=1/4}}$	=	−1.14134
$b_3^{\hat{A}_{44}^0}$	=	−0.852876	$b_3^{\omega_{44}^0}$	=	−0.0307812			
			$b_4^{\omega_{44}^0}$	=	−0.801552			
$c_{11}^{\hat{A}_{44}}$	=	1.2436	$c_{11}^{\omega_{44}}$	=	−0.92902	$c_{11}^{\Delta t_4}$	=	−2.28656
$c_{12}^{\hat{A}_{44}}$	=	−1.60555	$c_{12}^{\omega_{44}}$	=	10.86310	$c_{12}^{\Delta t_{44}}$	=	1.66532
$c_{13}^{\hat{A}_{44}}$	=	−4.05685	$c_{13}^{\omega_{44}}$	=	−4.44930	$c_{21}^{\Delta t_{44}}$	=	−0.589331
$c_{14}^{\hat{A}_{44}}$	=	1.59143	$c_{14}^{\omega_{44}}$	=	3.01808	$c_{22}^{\Delta t_{44}}$	=	0.708784
$c_{21}^{\hat{A}_{44}}$	=	0.837418	$c_{22}^{\omega_{44}}$	=	1.62523			
$c_{22}^{\hat{A}_{44}}$	=	−2.93528	$c_{23}^{\omega_{44}}$	=	−7.70486			
$c_{23}^{\hat{A}_{44}}$	=	−11.5591	$c_{23}^{\omega_{44}}$	=	15.06517			
$c_{24}^{\hat{A}_{44}}$	=	34.1863	$c_{41}^{\omega_{44}}$	=	0.93790			
$c_{31}^{\hat{A}_{44}}$	=	0.950035	$c_{42}^{\omega_{44}}$	=	8.36038			
$c_{32}^{\hat{A}_{44}}$	=	7.95168	$c_{43}^{\omega_{44}}$	=	−4.85774			
$c_{33}^{\hat{A}_{44}}$	=	−1.26899	$c_{44}^{\omega_{44}}$	=	4.80446			
$c_{34}^{\hat{A}_{44}}$	=	−9.72147						

where $i = \{1, 2, 3\}$.

For what concerns Δt_{43}, it is represented as

$$\Delta t_{43} = \Delta t_{43}^0 \Delta t_{43}^{\rm orb}(\nu) \Delta t_{43}^{\rm spin}\left(\hat{S}, \nu\right) \ , \tag{D82}$$

with

$$\Delta t_{43}^{\rm orb}(\nu) = \frac{1 + a_1^{\Delta t_{43}}\nu + a_2^{\Delta t_{43}}\nu^2}{1 + a_3^{\Delta t_{43}}\nu + a_4^{\Delta t_{43}}\nu^2} \ , \tag{D83}$$

$$\Delta t_{43}^{\rm spin}\left(\hat{S}, \nu = 0\right) = \frac{1 + b_1^{\Delta t_{43}^0}\hat{S} + b_2^{\Delta t_{43}^0}\hat{S}^2}{1 + b_3^{\Delta t_{43}^0}\hat{S}} \ . \tag{D84}$$

We then incorporate the general ν-dependence via the replacement

$$b_i^{\Delta t_{43}^0} \to \frac{b_1^{\Delta t_{43}^0} + c_{i1}^{\Delta t_{43}}\nu + c_{i2}^{\Delta t_{43}}\nu^2}{1 + c_{i3}^{\Delta t_{43}}\nu + c_{i4}^{\Delta t_{43}}\nu^2} \ , \tag{D85}$$

with $i = \{1, 2, 3\}$. The explicit values of the fit coefficients are listed in Table XXII.

g. $(\ell, m) = (4, 2)$ *multipole*

The peak amplitude of the $(4, 2)$ mode is fitted with a factorized template of the form

$$\hat{A}_{42}^{\rm peak} = \hat{A}_{42}^{\rm peak_0}\left(1 - 3\nu\right)\hat{A}_{42}^{\rm orb}\left(\nu\right)\hat{A}_{42}^{\rm Spin}\left(\hat{S}, \nu\right) \ , \tag{D86}$$

where $\hat{A}_{42}^{\rm peak_0}$ is the peak amplitude of the mode in the test-particle limit. The factor $\hat{A}_{42}^{\rm orb}$ is informed by non-spinning waveforms and is fitted with the template

$$\hat{A}_{42}^{\rm orb}(\nu) = 1 + a_1^{\hat{A}_{42}}\nu + a_2^{\hat{A}_{42}}\nu^2 \ . \tag{D87}$$

The spin dependence is first captured for the test-particle limit with the function

$$\hat{A}_{42}^{\rm Spin}(\hat{S}, \nu = 0) = \frac{1 + b_1^{\hat{A}_{42}^0}\hat{S} + b_2^{\hat{A}_{42}^0}\hat{S}^2}{1 + b_3^{\hat{A}_{42}^0}\hat{S} + b_4^{\hat{A}_{42}^0}\hat{S}^2} \ . \tag{D88}$$

The general ν-dependence is then taken into account via the replacement

$$b_i^{\hat{A}_{42}^0} \to \frac{b_i^{\hat{A}_{42}^0} + c_{i1}^{\hat{A}_{42}}\nu}{1 + c_{i2}^{\hat{A}_{42}}\nu} \ , \tag{D89}$$

with $i = \{1, 2, 3, 4\}$.

The instantaneous frequency $\omega_{42}^{\rm peak}$ is factorized as

$$\omega_{42}^{\rm peak} = \omega_{42}^{\rm peak_0}\omega_{42}^{\rm orb}(\nu)\omega_{42}^{\rm Spin}\left(\hat{S}, \nu\right) \tag{D90}$$

The orbital dependence is modeled through

$$\omega_{42}^{\rm orb}(\nu) = \frac{1 + a_1^{\omega_{42}}\nu + a_2^{\omega_{42}}\nu^2}{1 + a_3^{\omega_{42}}\nu + a_4^{\omega_{42}}\nu^2} \ . \tag{D91}$$

TABLE XXII. Explicit coefficients of the fits of $\hat{A}_{43}^{\rm peak}$, $\omega_{43}^{\rm peak}$ and Δt_{43}.

$\hat{A}_{43}^{\rm peak_0}$	=	0.0941570	$\omega_{43}^{\rm peak_0}$	=	0.636130	Δt_{43}^0	=	9.53705
$a_1^{\hat{A}_{43}}$	=	-5.74386	$a_1^{\omega_{43}}$	=	-9.02463	$a_1^{\Delta t_{43}}$	=	-11.2377
$a_2^{\hat{A}_{43}}$	=	12.6016	$a_2^{\omega_{43}}$	=	21.9802	$a_2^{\Delta t_{43}}$	=	38.3177
$a_3^{\hat{A}_{43}}$	=	-3.27435	$a_3^{\omega_{43}}$	=	-8.75892	$a_3^{\Delta t_{43}}$	=	-7.29734
$a_4^{\omega_{43}}$	=	20.5624				$a_4^{\Delta t_{43}}$	=	21.4267
$b_1^{\hat{A}_{43}^0}$	=	-0.02132252	$b_1^{\omega_{43}^0}$	=	-0.973324	$b_1^{\Delta t_{43}^0}$	=	-1.371832
$b_2^{\hat{A}_{43}^0}$	=	0.02592749	$b_2^{\omega_{43}^0}$	=	-0.109921	$b_2^{\Delta t_{43}^0}$	=	0.362375
$b_3^{\hat{A}_{43}^0}$	=	-0.826977	$b_3^{\omega_{43}^0}$	=	-1.08036	$b_3^{\Delta t_{43}^0}$	=	-1.0808402
$b_1^{\hat{A}_{43}^{\nu=1/4}}$	=	-0.00471163						
$b_2^{\hat{A}_{43}^{\nu=1/4}}$	=	0.0291409						
$b_3^{\hat{A}_{43}^{\nu=1/4}}$	=	-0.351031						
$c_{11}^{\hat{A}_{43}}$	=	0.249099	$c_{11}^{\omega_{43}}$	=	11.5224	$c_{11}^{\Delta t_{43}}$	=	3.215984
$c_{12}^{\hat{A}_{43}}$	=	-7.345984	$c_{12}^{\omega_{43}}$	=	-26.8421	$c_{12}^{\Delta t_{43}}$	=	42.133767
$c_{13}^{\hat{A}_{43}}$	=	108.923746	$c_{13}^{\omega_{43}}$	=	-2.84285	$c_{13}^{\Delta t_{43}}$	=	-9.440398
$c_{21}^{\hat{A}_{43}}$	=	-0.104206	$c_{21}^{\omega_{43}}$	=	3.51943	$c_{14}^{\Delta t_{43}}$	=	35.160776
$c_{22}^{\hat{A}_{43}}$	=	7.073534	$c_{22}^{\omega_{43}}$	=	-12.1688	$c_{21}^{\Delta t_{43}}$	=	1.133942
$c_{23}^{\hat{A}_{43}}$	=	-44.374738	$c_{23}^{\omega_{43}}$	=	-3.96385	$c_{22}^{\Delta t_{43}}$	=	-10.356311
$c_{31}^{\hat{A}_{43}}$	=	3.545134	$c_{31}^{\omega_{43}}$	=	5.53433	$c_{23}^{\Delta t_{43}}$	=	-6.701429
$c_{32}^{\hat{A}_{43}}$	=	1.341375	$c_{32}^{\omega_{43}}$	=	3.73988	$c_{24}^{\Delta t_{43}}$	=	10.726960
$c_{33}^{\hat{A}_{43}}$	=	-19.552083	$c_{33}^{\omega_{43}}$	=	4.219	$c_{31}^{\Delta t_{43}}$	=	-6.036207
						$c_{32}^{\Delta t_{43}}$	=	67.730599
						$c_{33}^{\Delta t_{43}}$	=	-3.082275
						$c_{34}^{\Delta t_{43}}$	=	11.547917

The spin dependence is fitted first for the test-mass case with

$$\omega_{42}^{\rm Spin}\left(\hat{S},\nu=0\right)=\frac{1+b_1^{\omega_{42}^0}\hat{S}+b_2^{\omega_{42}^0}\hat{S}^2}{1+b_3^{\omega_{42}^0}\hat{S}+b_4^{\omega_{42}^0}\hat{S}^2}\ , \tag{D92}$$

and then the general ν-dependence is taken into account via the replacement

$$b_i^{\omega_{42}^0}\to\frac{b_i^{\omega_{42}^0}+c_{i1}^{\omega_{42}}\nu}{1+c_{i2}^{\omega_{42}}\nu+c_{i3}^{\omega_{42}}\nu^2}\ , \tag{D93}$$

with $i=\{1,2,3,4\}$. The delay Δt_{42} is fitted as

$$\Delta t_{42}=\Delta t_{42}^0\Delta t_{42}^{\rm orb}(\nu)\Delta t_{42}^{\rm spin}\left(\hat{S},\nu\right)\ , \tag{D94}$$

where

$$\Delta t_{42}^{\rm orb}(\nu)=\frac{1+a_1^{\Delta t_{42}}\nu+a_2^{\Delta t_{42}}\nu^2}{1+a_3^{\Delta t_{42}}\nu+a_4^{\Delta t_{42}}\nu^2}\ , \tag{D95}$$

$$\Delta t_{42}^{\rm spin}\left(\hat{S},\nu=0\right)=\frac{1+b_1^{\Delta t_{42}^0}\hat{S}}{1+b_2^{\Delta t_{42}^0}\hat{S}}\ . \tag{D96}$$

For $\nu<6/25$ the spin factor is approximated by the test-particle fit. For the other regions, it is extrapolated using

$$b_i^{\Delta t_{42}^0}\to\frac{b_1^{\Delta t_{42}^0}+c_{i1}^{\Delta t_{42}}\nu}{1+c_{i2}^{\Delta t_{42}}\nu}\ , \tag{D97}$$

with $i=\{1,2\}$. The explicit values of the coefficients of the fits are listed in Table XXIII.

h. $(\ell,m)=(5,5)$ *multipole*

For this multipole, the peak amplitude is written as the sum of two terms as

$$\hat{A}_{55}^{\rm peak}=\hat{A}_{55}^{\rm peak_0}X_{12}\left(1-2\nu\right)\hat{A}_{55}^{\rm orb}(\nu)+\hat{A}_{55}^{\rm Spin}(\tilde{a}_{12},\nu)\ , \tag{D98}$$

where $\hat{A}_{55}^{\rm peak_0}$ is the peak amplitude in the test particle limit. The non-spinning ν-dependence is modeled as

$$\hat{A}_{55}^{\rm orb}(\nu)=1+a_1^{\hat{A}_{55}}\nu+a_2^{\hat{A}_{55}}\nu^2\ . \tag{D99}$$

The spin dependence is first fitted to the test-particle limit using

$$\hat{A}_{55}^{\rm Spin}(\tilde{a}_{12},\nu=0)=\frac{b_1^{\hat{A}_{55}^0}\tilde{a}_{12}}{1+b_2^{\hat{A}_{55}^0}\tilde{a}_{12}}\ , \tag{D100}$$

TABLE XXIII. Explicit coefficients of the fits of $\hat{A}^{\rm peak}_{42}$, $\omega^{\rm peak}_{42}$ and Δt_{42}.

$\hat{A}^{\rm peak_0}_{42}$	=	0.0314364	$\omega^{\rm peak_0}_{42}$	=	0.617533	Δt^0_{42}	=	11.66665
$a^{\hat{A}_{42}}_1$	=	-4.56243	$a^{\omega_{42}}_1$	=	-7.44121	$a^{\Delta t_{42}}_1$	=	-9.844617
$a^{\hat{A}_{42}}_2$	=	6.4522	$a^{\omega_{42}}_2$	=	14.233	$a^{\Delta t_{42}}_2$	=	23.32294
			$a^{\omega_{42}}_3$	=	-6.61754	$a^{\Delta t_{42}}_3$	=	-5.760481
			$a^{\omega_{42}}_4$	=	11.4329	$a^{\Delta t_{42}}_4$	=	7.121793
$b^{\hat{A}^0_{42}}_1$	=	-1.63682	$b^{\omega^0_{42}}_1$	=	-2.37589	$b^{\Delta t^0_{42}}_1$	=	-1.3002045
$b^{\hat{A}^0_{42}}_2$	=	0.854459	$b^{\omega^0_{42}}_2$	=	1.97249	$b^{\Delta t^0_{42}}_2$	=	-0.9494348
$b^{\hat{A}^0_{42}}_3$	=	0.120537	$b^{\omega^0_{42}}_3$	=	-2.36107			
$b^{\hat{A}^0_{42}}_4$	=	-0.399718	$b^{\omega^0_{42}}_4$	=	2.16383			
$c^{\hat{A}_{42}}_{11}$	=	6.53943	$c^{\omega_{42}}_{11}$	=	10.1045	$c^{\Delta t_{42}}_{11}$	=	24.604717
$c^{\hat{A}_{42}}_{12}$	=	-4.00073	$c^{\omega_{42}}_{12}$	=	-6.94127	$c^{\Delta t_{42}}_{12}$	=	-0.808279
$c^{\hat{A}_{42}}_{21}$	=	-0.638688	$c^{\omega_{42}}_{13}$	=	12.1857	$c^{\Delta t_{42}}_{21}$	=	62.471781
$c^{\hat{A}_{42}}_{22}$	=	-3.94066	$c^{\omega_{42}}_{21}$	=	-1.62866	$c^{\Delta t_{42}}_{22}$	=	48.340961
$c^{\hat{A}_{42}}_{31}$	=	-0.482148	$c^{\omega_{42}}_{22}$	=	-2.6756			
$c^{\hat{A}_{42}}_{32}$	=	$7.668 \times 10^{-9} - 4$	$c^{\omega_{42}}_{23}$	=	-4.7536			
$c^{\hat{A}_{42}}_{41}$	=	1.25617	$c^{\omega_{42}}_{31}$	=	10.071			
$c^{\hat{A}_{42}}_{42}$	=	-4.04848	$c^{\omega_{42}}_{32}$	=	-6.7299			
			$c^{\omega_{43}}_{33}$	=	12.0377			
			$c^{\omega_{42}}_{41}$	=	-8.56139			
			$c^{\omega_{42}}_{42}$	=	-5.27136			
			$c^{\omega_{43}}_{43}$	=	5.10653			

and then extrapolated to the comparable mass region through

$$b_1^{\hat{A}^0_{55}} \to \frac{b_1^{\hat{A}^0_{55}}}{1 + c_{11}^{\hat{A}_{55}}\nu + c_{12}^{\hat{A}_{55}}\nu^2} \,, \tag{D101}$$

$$b_2^{\hat{A}^0_{55}} \to \frac{b_2^{\hat{A}^0_{55}}}{1 + c_{21}^{\hat{A}_{55}}\nu + c_{22}^{\hat{A}_{55}}\nu^2} \,. \tag{D102}$$

The frequency of the $(5,5)$ mode is factorized as

$$\omega_{55}^{\rm peak} = \omega_{55}^{\rm peak_0}\omega_{55}^{\rm orb}(\nu)\omega_{55}^{\rm Spin}\left(\hat{S},\nu\right) \,, \tag{D103}$$

where

$$\omega_{55}^{\rm orb}(\nu) = \frac{1 + a_1^{\omega_{55}}\nu + a_2^{\omega_{55}}\nu^2}{1 + a_3^{\omega_{55}}\nu} \,, \tag{D104}$$

and the test-particle spin factor is given by

$$\omega_{55}^{\rm Spin}\left(\hat{S},\nu=0\right) = \frac{1 + b_1^{\omega^0_{55}}\hat{S}}{1 + b_2^{\omega^0_{55}}\hat{S}} \,. \tag{D105}$$

The spin dependence in the general case is obtained by means of

$$b_i^{\omega^0_{55}} \to \frac{b_i^{\omega^0_{55}} + c_{i1}^{\omega_{55}}\nu}{1 + c_{i2}^{\omega_{55}}\nu} \,, \tag{D106}$$

with $i = \{1,2\}$. Note that, in this case, we do not incorporate spin-dependence in Δ_{55}, but only rely on the nonspinning fit of Ref. [30].

3. NR-fitting of the postpeak parameters

In this Appendix we report the fits of the postpeak parameters $(c_3^{A_{\ell m}}, c_3^{\phi_{\ell m}}, c_4^{\phi_{\ell m}})$ for all multipoles multipoles discussed in the main text. For $(2,2)$, $(3,3)$, $(4,4)$, $(5,5)$ we present fits that explicitly depend on the spins of the black holes. By contrast, the same parameters for the other multipoles $(2,1)$, $(3,2)$, $(3,1)$ $(4,3)$, $(4,2)$, are approximated by the spin-independent fits of Ref. [30]. Let us note, however, that we prefer to *not use* the full spin-dependent fits of $(c_3^{\phi_{33}}, c_4^{\phi_{33}})$ and in $(c_3^{\phi_{44}}, c_4^{\phi_{44}})$. Instead the fits of Ref. [30] are used to get a more robust behavior of ω_{33} and ω_{44} in all corners of the parameter space, notably when the mass ratio is between one and two and the spins are large. See Appendix D 4 for a brief discussion.

a. *The* $(\ell, m) = (2,2)$ *postpeak*

The data of $(c_3^{A_{22}}, c_3^{\phi_{22}}, c_4^{\phi_{22}})$ were extracted from NR fitting the NR waveforms in the calibration set over an interval starting at the peak of length $4\tau_1^{22}$.

The fits are done in three steps, based on the model

$$Y(\nu;\,\hat{S}) = b_0^Y(\nu) + b_1^Y\left(X_{12}\right)\hat{S} + b_2^Y\left(X_{12}\right)\hat{S}^2 + b_3^Y\left(X_{12}\right)\hat{S}^3 + b_4^Y\left(X_{12}\right)\hat{S}^4. \tag{D107}$$

In the first step $Y(\nu;\,\hat{S}=0)$ is fitted to the non-spinning

TABLE XXIV. Explicit coefficients of the fits of $\hat{A}_{55}^{\rm peak}$ and $\omega_{55}^{\rm peak}$

$\hat{A}_{55}^{\rm peak_0}$	=	0.00522697	$\omega_{55}^{\rm peak_0}$	=	0.818117
$a_1^{\hat{A}_{55}}$	=	−0.29628	$a_1^{\omega_{55}}$	=	−2.8918
$a_2^{\hat{A}_{55}}$	=	6.4207	$a_2^{\omega_{55}}$	=	−3.2012
			$a_3^{\omega_{55}}$	=	−3.773
$b_1^{\hat{A}_{55}^0}$	=	0.04360530	$b_1^{\omega_{55}^0}$	=	−0.332703
$b_2^{\hat{A}_{55}^0}$	=	−0.5769451	$b_2^{\omega_{55}^0}$	=	−0.675738
$c_{11}^{\hat{A}_{55}}$	=	5.720690	$c_{11}^{\omega_{55}}$	=	1.487294
$c_{12}^{\hat{A}_{55}}$	=	44.868515	$c_{12}^{\omega_{55}}$	=	−2.058537
$c_{21}^{\hat{A}_{55}}$	=	12.777090	$c_{21}^{\omega_{55}}$	=	1.454248
$c_{22}^{\hat{A}_{55}}$	=	−42.548247	$c_{22}^{\omega_{55}}$	=	−1.301284

data. In the second step $b_i^Y\,(X_{12}=0)$ are fitted to the equal mass data. In the third and final step the fits are extrapolated to the comparable mass case imposing the 1-D fits informed in the previous two steps. The coefficients of the fit are listed in Table XXV.

b. *The* $(\ell,m)=(3,3)$ *postpeak*

The data of $(c_3^{A_{33}}, c_3^{\phi_{33}}, c_4^{\phi_{33}})$ were extracted from NR fitting the NR waveforms in the calibration set over an interval starting at the peak of length $1\tau_1^{33}$. The interpolation is modeled with the template

$$Y(\nu;\,\hat{S}) = b_0^Y(\nu) + b_1^Y\,(X_{12})\,\hat{S}. \tag{D108}$$

While for the case of $c_3^{A_{33}}$ the fit is done versus $\tilde{a}_{12}$. The fits are done in two hierarchical steps. (i) $b_0^Y(\nu)$ is fitted to the non-spinning data. (ii) $b_1^Y\,(X_{12})$ is fitted with a quadratic polynomial, while imposing the fit of $b_0^Y(\nu)$. The fits are given explicitly in Table XXVI.

c. *The* $(\ell,m)=(4,4)$ *postpeak*

The data of $(c_3^{A_{44}}, c_3^{\phi_{44}}, c_4^{\phi_{44}})$ were extracted from NR fitting the NR waveforms in the calibration set over an interval starting at the peak of length $1\tau_1^{44}$. The interpolation of $(c_3^{\phi_{44}}, c_4^{\phi_{44}})$ is modeled with the template

$$Y(\nu;\,\hat{S}) = b_0^Y(\nu) + b_1^Y\,(X_{12})\,\hat{S} + b_2^Y\,(X_{12})\,\hat{S}^2 \tag{D109}$$

in three steps, similar to the the $(2,2)$ mode. (i) $b_0^Y(\nu)$ is fitted to the non-spinning data. (ii) $b_i^Y\,(X_{12}=0)$ is fitted to the equal mass data. (iii) The full dependence of $b_i^Y\,(X_{12})$ on X_{12} is fitted while imposing the one-dimensional fits informed in the first two steps. $c_{3\,44}^{A}$ is modeled with the template

$$c_3^{A_{44}}(\nu;\,\hat{S}) = b_0^{c_3^{A_{44}}}(\nu) + b_1^{c_3^{A_{44}}}\nu\hat{S} + b_2^{c_3^{A_{44}}}\nu\hat{S}^2. \tag{D110}$$

The fit is is done in two steps. (i) $b_0^{c_3^{A_{44}}}(\nu)$ is fitted to the non-spinning data. (ii) The coefficients $b_i^{c_3^{A_{44}}}$ are informed using the spinning data, while imposing the non-spinning fit. The fits are given explicitly in Table XXVII.

d. *The* $(\ell,m)=(5,5)$ *postpeak*

The data of $(c_3^{A_{55}}, c_3^{\phi_{55}}, c_4^{\phi_{55}})$ were extracted from NR fitting the NR waveforms in the calibration set over an interval starting at the peak of length $1\tau_1^{55}$. The interpolation is modeled with the template

$$Y(\nu;\,\hat{S}) = b_0^Y(\nu) + b_1^Y\,(X_{12})\,\hat{S} + b_2^Y\,(X_{12})\,\hat{S}^2. \tag{D111}$$

While for the case of $c_3^{A_{55}}$ the fit is done versus $\tilde{a}_{12}$. The fits are done in two hierarchical steps. (i) $b_0^Y(\nu)$ is fitted to the non-spinning data. (ii) $b_i^Y\,(X_{12})$ are fitted with a linear polynomial, while imposing the fit of $b_0^Y(\nu)$. The fits are given explicitly in Table XXVIII.

4. Motivating the choices for the $(3,3)$ and $(4,4)$ postmerger phases

As mentioned above, the results presented in the main text *do not* rely on the the fits of $(c_3^{\phi_{33}}, c_4^{\phi_{33}})$ and $(c_3^{\phi_{44}}, c_4^{\phi_{44}})$ given in Appendix D 3 with the full spin dependence, but instead use only their spin-independent part, as already presented Ref. [30]. This choice was made so to ensure a more robust behavior of the frequency at the beginning of the ringdown when the spins are positive and large. We illustrate this argument inspecting the behavior of ω_{44} for two highly-spinning configurations. Figure 22 shows EOB/NR comparisons with two EOB waveforms obtained with either the nonspinning fits (red online) or those with the full spin dependence (green). One sees that the spin-dependent fit performs rather well for `SXS:BBH:1124` $(1, 0.998, 0.998)$, consistently with the fact that we used `SXS:BBH:0178`,

TABLE XXV. The fitted coefficients of $(c_3^{A_{22}}, c_3^{\phi_{22}}, c_4^{\phi_{22}})$ as defined in Eq. (D107).

$Y = c_3^{A_{22}}$			$Y = c_3^{\phi_{22}}$			$Y = c_4^{\phi_{22}}$		
$b_0^{c_3^A}(\nu)$	$= -0.5585$	0.81196ν	$b_0^{c_3^\phi}(\nu)$	$= 3.8436$	$+0.71565\nu$	$b_0^{c_4^\phi}(\nu)$	$= 1.4736$	2.2337ν
$b_1^{c_3^A}(X_{12})$	$= -0.398576$	$+0.1659421X_{12}$	$b_1^{c_3^\phi}(X_{12})$	$= 5.12794$	$-1.323643X_{12}$	$b_1^{c_4^\phi}(X_{12})$	$= 8.26539$	$+0.779683X_{12}$
$b_2^{c_3^A}(X_{12})$	$= 0.099805$	$-0.2560047X_{12}$	$b_2^{c_3^\phi}(X_{12})$	$= 9.9136$	$-3.555007X_{12}$	$b_2^{c_4^\phi}(X_{12})$	$= 14.2053$	$-0.069638X_{12}$
$b_3^{c_3^A}(X_{12})$	$= 0.72125$	$-0.9418946X_{12}$	$b_3^{c_3^\phi}(X_{12})$	$= -4.1075$	$+7.011267X_{12}$	$b_3^{c_4^\phi}(X_{12})$	$=$	0
$b_4^{c_3^A}(X_{12})$	$=$	0	$b_4^{c_3^\phi}(X_{12})$	$= -31.5562$	$+32.737824X_{12}$	$b_4^{c_4^\phi}(X_{12})$	$=$	0

TABLE XXVI. The explicit fits of $(c_3^{A_{33}}, c_3^{\phi_{33}}, c_4^{\phi_{33}})$. The reader should note that the fits of $(c_3^{\phi_{33}}, c_4^{\phi_{33}})$ are not used for any of the results given in the main text. Instead the corresponding fits of Ref. [30] are used. See Appendix D 4 for a brief discussion.

$c_3^{A_{33}}(\nu, X_{12}, \tilde{a}_{12})$	$= -0.5585$	$+0.81196\nu$	$+$	$(-0.3502608$	$+1.587606X_{12}$	$-1.555325X_{12}^2)$	$\tilde{a}_{12}$
$c_3^{\phi_{33}}\left(\nu, X_{12}, \hat{S}\right)$	$= 3.0611$	-6.1597ν	$+$	$(-0.634377$	$+5.983525X_{12}$	$-5.8819X_{12}^2)$	$\hat{S}$
$c_4^{\phi_{33}}\left(\nu, X_{12}, \hat{S}\right)$	$= 1.789$	-5.6684ν	$+$	$(-3.877528$	$+12.0433X_{12}$	$-6.524665X_{12}^2)$	$\hat{S}$

with parameters $(1, 0.9942, 0.9942)$, to inform the fit. By contrast, one sees that the same description applied to a different configuration, $(1.5, 0.95, 0.95)$, corresponding to `SXS:BBH:1146`, does not perform equally well, with a nonnegiglible gap between the EOB and NR frequencies accumulating right after the peak. One finds, however, that removing the spin-dependence in $(c_3^{\phi_{44}}, c_4^{\phi_{44}})$ allows one to obtain a much closer EOB/NR consistency for `SXS:BBH:1146`. For the other case, moving to the nonspinning description slightly worsens the agreement, both before and after the waveform peak [7]. On the basis of these results, and especially seen the rather good $\bar{F}$ behavior illustrated in Fig. 6, we decided to be simple and remove the spin dependence in $(c_3^{\phi_{44}}, c_4^{\phi_{44}})$. We applied the same rational also to the $(3,3)$ mode. Clearly, in case of very high-spins, currents fits should be improved to some extent, increasing the calibration set so to incorporate more points in that corner of the parameter space. This will be investigated in future work.

5. Modeling the NQC extraction points

Let us finally discuss analytic representations of the NR point (amplitude, frequency and derivative) on the multipolar waveform that is needed for computing the NQC corrections to the waveform multipole by multipole. For the $(2,2)$ and $(3,3)$ modes we give below dedicated fits. For all other modes, the useful NR quantities are obtained analytically from the (fitted) post-peak analytical waveform discussed above. Let us recall here that, for each mode, the NQC time is always

$$t_{\ell m}^{\rm NQC} \equiv t_{\ell m}^{\rm peak} + 2. \tag{D112}$$

All quantities mentioned below with the NQC label are computed at $t = t_{\ell m}^{\rm NQC}$.

a. *The* $(2,2)$ *NQC extraction point*

For the $(2,2)$ mode the NQC-point quantities $\left\{\hat{A}_{22}^{\rm NQC}, \dot{A}_{22}^{\rm NQC}, \omega_{22}^{\rm NQC}, \dot{\omega}_{22}^{\rm NQC}\right\}$ are fitted directly. The 3-piece hybrid fit, presented in [24, 37] is modified for $q > 4$. The fits of $\left\{\hat{A}_{22}^{\rm NQC}\omega_{22}^{\rm NQC}\right\}$ are done using the template discussed already for the peak, see Appendix D 2 a. The reader should note however that the fit of $\omega_{22}^{\rm NQC}$ has additional flexibility. The replacement in (D20) is also done for $i = 2$ for this case. In the following the fitting of $\dot{A}_{22}^{\rm NQC}$ and $\dot{\omega}_{22}^{\rm NQC}$. Both rely on the same template thus it is only given for the former explicitly. To fit the time derivative of the amplitude at $t_{\rm NQC}$ it was proven useful to not fit it directly, but to fit $\dot{A}_{22}^{\rm NQC}/\nu\omega_{22}^{\rm NQC}$, starting with the following factorization

$$\frac{\dot{A}_{22}^{\rm NQC}}{\nu\omega_{22}^{\rm NQC}} = \left[\hat{\dot{A}}_{22}^{\rm NQC_{orb}}(\nu) + \hat{\dot{A}}_{22}^{\rm NQC_{Spin}}\left(X_{12}, \hat{S}\right)\right]. \tag{D113}$$

The nonspinning contribution is fitted as

$$\hat{\dot{A}}_{22}^{\rm NQC_{orb}}(\nu) = 1 + a_1^{\dot{A}_{22}^{\rm NQC}}\nu + a_2^{\dot{A}_{22}^{\rm NQC}}\nu^2. \tag{D114}$$

The spin-dependence is represented as

$$\hat{\dot{A}}_{22}^{\rm NQC_{Spin}}\left(X_{12}\hat{S}\right) = b_1^{\dot{A}_{22}^{\rm NQC_{m_1=m_2}}}\hat{S} + b_1^{\dot{A}_{22}^{\rm NQC_{m_1=m_2}}}\hat{S}^2\,. \tag{D115}$$

[7] The reader should note that the postpeak phasing impacts the inspiral waveform through the NQC extraction points obtained from the postpeak template. See Appendix D 5 c

TABLE XXVII. The explicit fits of $(c_3^{A_{44}}, c_3^{\phi_{44}}, c_4^{\phi_{44}})$. The reader should note that the fits of $(c_3^{\phi_{44}}, c_4^{\phi_{44}})$ are not used for any of the results given in the main text. Instead the corresponding fits of Ref. [30] are used. See Appendix D 4 for a brief discussion.

$c_3^{A_{44}}\left(\nu,\hat{S}\right)$	=	-0.41591	$+3.2099\nu$	$-$		9.614738ν	$\hat{S}$	$+$		122.461125ν	$\hat{S}^2$
$c_3^{\phi_{44}}\left(\nu,X_{12},\hat{S}\right)$	=	$\frac{3.6662-30.072\nu+76.371\nu^2}{1-3.5522\nu}$	$+$	$(-4.9184$	$+7.911653X_{12})$	$\hat{S}$	$+$	$(-15.6772$	$+21.181688X_{12})$	$\hat{S}^2$	
$c_4^{\phi_{44}}\left(\nu,X_{12},\hat{S}\right)$	=	0.21595	$+23.216\nu$	$+$	$(-3.4207$	$+11.746452X_{12})$	$\hat{S}$	$+$	$(-15.5383$	$+34.922883X_{12})$	$\hat{S}^2$

TABLE XXVIII. The explicit fits of $(c_3^{A_{55}}, c_3^{\phi_{55}}, c_4^{\phi_{55}})$.

$c_3^{A_{55}}\left(\nu,X_{12},\tilde{a}_{12}\right)$	=	-7.063079	$+65.464944\nu$	$+$	$(-2.055335$	$-0.585373X_{12})$	$\tilde{a}_{12}$	$+$	$(-12.631409$	$+19.271346X_{12})$	$\tilde{a}_{12}^2$
$c_3^{\phi_{55}}\left(\nu,X_{12},\hat{S}\right)$	=	-1.510167	$+30.569461\nu$	$+$	$(-2.687133$	$+4.873750X_{12})$	$\hat{S}$	$+$	$(-14.629684$	$+19.696954X_{12})$	$\hat{S}^2$
$c_4^{\phi_{55}}\left(\nu,X_{12},\hat{S}\right)$	=	-1.383721	$+56.871881\nu$	$+$	$(+7.198729$	$-3.870998X_{12})$	$\hat{S}$	$+$	$(-25.992190$	$+36.882645X_{12})$	$\hat{S}^2$

The extrapolation to the $m_1 \neq m_2$ regime is done via the replacement

$$b_i^{\dot{A}_{22}^{\rm NQC_{m_1=m_2}}} \to b_i^{\dot{A}_{22}^{\rm NQC_{m_1=m_2}}} + c_i^{\dot{A}_{22}^{\rm NQC_{m_1=m_2}}} X_{12}\,, \quad \text{(D116)}$$

with $i=\{1,2\}$. All coefficients are listed explicitly in Table XXIX.

b. *The* $(3,3)$ *NQC extraction point*

Let us discuss now explicit fits for $\left\{\hat{A}_{33}^{\rm NQC}, \dot{A}_{33}^{\rm NQC}, \omega_{33}^{\rm NQC}, \dot{\omega}_{33}^{\rm NQC}\right\}$. The amplitude $\hat{A}_{33}^{\rm NQC}$ is written as two separate terms as

$$\hat{A}_{33}^{\rm NQC} = \hat{A}_{33}^{\rm NQC_0} X_{12} \hat{A}_{33}^{\rm NQC_{orb}}(\nu) + \hat{A}_{33}^{\rm NQC_S}(\nu,\tilde{a}_{12})\,, \quad \text{(D117)}$$

where $\hat{A}_{33}^{\rm NQC_0}$ is the test-particle value. The non-spinning sector is fitted after factorization of $\hat{A}_{33}^{\rm NQC_0} X_{12}$ with

$$\hat{A}_{33}^{\rm NQC_{orb}}(\nu) = 1 + a_1^{\hat{A}_{33}^{\rm NQC}}\nu + a_2^{\hat{A}_{33}^{\rm NQC}}\nu^2\,. \quad \text{(D118)}$$

The spin-dependent factor $\hat{A}_{33}^{\rm NQC_S}$ is first fitted in the $\nu=0$ limit with

$$\hat{A}_{33}^{\rm NQC_S} = \frac{b_1^{\hat{A}_{33}^{\rm NQC}}\tilde{a}_{12} + b_2^{\hat{A}_{33}^{\rm NQC}}\tilde{a}_{12}^2}{1 + b_3^{\hat{A}_{33}^{\rm NQC}}\tilde{a}_{12}}\,. \quad \text{(D119)}$$

and then extended to the $\nu \neq 0$ regime through

$$b_i^{\hat{A}_{33}^{\rm NQC}} \to \frac{b_i^{\hat{A}_{33}^{\rm NQC}} + c_{i1}^{\hat{A}_{33}^{\rm NQC}}\nu}{1 + c_{i2}^{\hat{A}_{33}^{\rm NQC}}\nu} \text{ with } i=\{1,2,3\}\,. \quad \text{(D120)}$$

The time-derivative of the amplitude $\dot{A}_{33}^{\rm NQC}$ was fitted in two steps. In the first step, one is fitting only equal-mass data (but, crucially, including also data with un-equal spins), as

$$\frac{\dot{A}_{33}^{\rm NQC_{\nu=1/4}}}{10^5} = d_0^{\dot{A}_{33}^{\rm NQC_{\nu=1/4}}} + d_1^{\dot{A}_{33}^{\rm NQC_{\nu=1/4}}}\tilde{a}_{12} + d_2^{\dot{A}_{33}^{\rm NQC_{\nu=1/4}}}\tilde{a}_{12}^2\,. \quad \text{(D121)}$$

The un-equal mass sector is fitted with the same template as $\hat{A}_{33}^{\rm NQC}$ with 3 modifications: (i) X_{12} is not factorized as in (D117); (ii) The spin variable in (D119) is chosen to be $\hat{S}$; (iii) the transformation is only done for $i=2$ in (D120), $c_{1i}^{\hat{A}_{33}^{\rm NQC}} = c_{3i}^{\hat{A}_{33}^{\rm NQC}} = 0$.

Moving now to the NQC frequency $\omega_{33}^{\rm NQC}$, we assume the following factorization

$$\omega_{33}^{\rm NQC} = \omega_{33}^{\rm NQC_0}\omega_{33}^{\rm NQC_{orb}}\omega_{33}^{\rm NQC_S}\,, \quad \text{(D122)}$$

where $\omega_{33}^{\rm NQC_{orb}}$ is fitted to the nonspinning data with a second-order polynomial in ν as

$$\omega_{33}^{\rm NQC_{orb}} = 1 + a_1^{\omega_{33}^{\rm NQC}}\nu + a_2^{\omega_{33}^{\rm NQC}}\nu^2\,. \quad \text{(D123)}$$

Then, $\omega_{33}^{\rm NQC_S}$ if fitted to the test-particle data using

$$\omega_{33}^{\rm NQC_S} = \frac{1 + b_1^{\omega_{33}^{\rm NQC}}\hat{S}}{1 + b_2^{\omega_{33}^{\rm NQC}}\hat{S}}\,. \quad \text{(D124)}$$

Finally, the spin-dependence in $\omega_{33}^{\rm NQC_S}$ incorporates ν-dependent effects as

$$b_i^{\omega_{33}^{\rm NQC}} \to b_i^{\omega_{33}^{\rm NQC}} + c_i^{\omega_{33}^{\rm NQC}}\nu \text{ with } i=\{1,2\}\,. \quad \text{(D125)}$$

Moving finally to the time-derivative of the frequency, $\dot{\omega}_{33}^{\rm NQC}$, it is fitted with the ansatz

$$\dot{\omega}_{33}^{\rm NQC} = \dot{\omega}_{33}^{\rm NQC_0}\dot{\omega}_{33}^{\rm NQC_{orb}} + \dot{\omega}_{33}^{\rm NQC_S}\,, \quad \text{(D126)}$$

where $\dot{\omega}_{33}^{\rm NQC_{orb}}$ is fitted to nonspinning data with

$$\dot{\omega}_{33}^{\rm NQC_{orb}} = 1 + a_1^{\dot{\omega}_{33}^{\rm NQC}}\nu\,. \quad \text{(D127)}$$

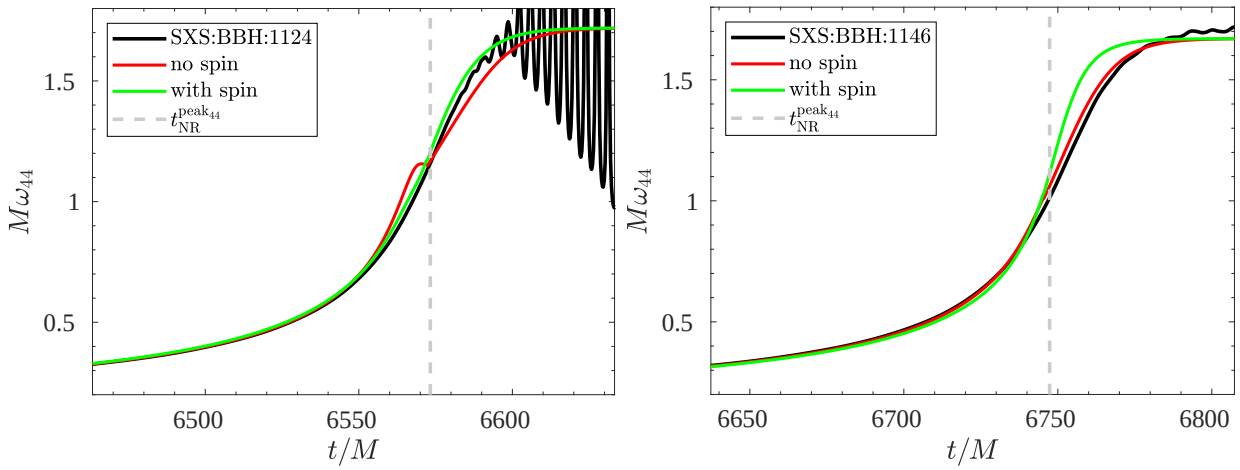

FIG. 22. In this figure we compare the frequency $M\omega_{44}$ for the two NR waveforms (black) SXS:BBH:1124 $(1, 0.998, 0.998)$ (left panel) and SXS:BBH:1146 $(1.5, 0.95, 0.95)$ (right) with the corresponding EOB waveforms, once obtained using the fits of Ref. [30] (right panel) and once with the spin-dependent fits presented in Appenix D 3 (green).

TABLE XXIX. Coefficients of the $(2,2)$ quantities needed to calculate the NQC extraction point. From left to right the columns show $\left\{\hat{A}_{22}^{\rm NQC}, \dot{A}_{22}^{\rm NQC}, \omega_{22}^{\rm NQC}, \dot{\omega}_{22}^{\rm NQC}\right\}$.

$\hat{A}_{22}^{\rm NQC}$			$\dot{A}_{22}^{\rm NQC}$			$\omega_{22}^{\rm NQC}$			$\dot{\omega}_{22}^{\rm NQC}$		
$\hat{A}_{22}^{\rm NQC_0}$	=	0.294773	$\dot{A}_{22}^{\rm NQC_0}/\nu$	=	−0.000243654	$\omega_{22}^{\rm NQC_0}$	=	0.285588	$\dot{\omega}_{22}^{\rm NQC_0}$	=	0.00628027
$a_1^{\hat{A}_{22}^{\rm NQC}}$	=	−0.052697	$a_1^{\dot{A}_{22}^{\rm NQC}}$	=	2.86637	$a_1^{\omega_{22}^{\rm NQC}}$	=	0.91704	$a_1^{\dot{\omega}_{22}^{\rm NQC}}$	=	2.4351
$a_2^{\hat{A}_{22}^{\rm NQC}}$	=	1.6088	$a_2^{\dot{A}_{22}^{\rm NQC}}$	=	−1.3667	$a_2^{\omega_{22}^{\rm NQC}}$	=	1.7912	$a_2^{\dot{\omega}_{22}^{\rm NQC}}$	=	4.4928
$b_1^{\hat{A}_{22}^{{\rm NQC}_{m_1=m_2}}}$	=	−0.705226	$b_1^{\dot{A}_{22}^{{\rm NQC}_{m_1=m_2}}}$	=	0.02679530	$b_1^{\omega_{22}^{{\rm NQC}_{m_1=m_2}}}$	=	−0.46550	$b_1^{\dot{\omega}_{22}^{{\rm NQC}_{m_1=m_2}}}$	=	0.001425242
$b_2^{\hat{A}_{22}^{{\rm NQC}_{m_1=m_2}}}$	=	−0.0953944	$b_2^{\dot{A}_{22}^{{\rm NQC}_{m_1=m_2}}}$	=	−0.0064409	$b_2^{\omega_{22}^{{\rm NQC}_{m_1=m_2}}}$	=	−0.078787	$b_2^{\dot{\omega}_{22}^{{\rm NQC}_{m_1=m_2}}}$	=	−0.00096073
$b_3^{\hat{A}_{22}^{{\rm NQC}_{m_1=m_2}}}$	=	−1.087280				$b_3^{\omega_{22}^{{\rm NQC}_{m_1=m_2}}}$	=	−0.852284			
$c_{11}^{\hat{A}_{22}^{\rm NQC}}$	=	0.009335	$c_1^{\dot{A}_{22}^{\rm NQC}}$	=	−0.015395218	$c_{11}^{\omega_{22}^{\rm NQC}}$	=	−0.338008	$c_1^{\dot{\omega}_{22}^{\rm NQC}}$	=	−0.000063766
$c_{12}^{\hat{A}_{22}^{\rm NQC}}$	=	0.582869	$c_2^{\dot{A}_{22}^{\rm NQC}}$	=	0.008732589	$c_{12}^{\omega_{22}^{\rm NQC}}$	=	1.077812	$c_2^{\dot{\omega}_{22}^{\rm NQC}}$	=	0.000513197
						$c_{21}^{\omega_{22}^{\rm NQC}}$	=	0.0555533			
						$c_{22}^{\omega_{22}^{\rm NQC}}$	=	−0.312861			
$c_{31}^{\hat{A}_{22}^{\rm NQC}}$	=	−0.140747				$c_{31}^{\omega_{22}^{\rm NQC}}$	=	0.289185			
$c_{32}^{\hat{A}_{22}^{\rm NQC}}$	=	0.505807				$c_{32}^{\omega_{22}^{\rm NQC}}$	=	−0.195838			

$\dot{\omega}_{33}^{\rm NQC_S}$ if fitted to the test-particle data with

$$\dot{\omega}_{33}^{\rm NQC_S} = b_1^{\dot{\omega}_{33}^{\rm NQC}} \hat{S} + b_2^{\dot{\omega}_{33}^{\rm NQC}} \hat{S}^2 \ . \tag{D128}$$

The spin dependence in $\dot{\omega}_{33}^{\rm NQC_S}$ is then extrapolated to the comparable mass through

$$b_i^{\dot{\omega}_{33}^{\rm NQC}} \to b_i^{\dot{\omega}_{33}^{\rm NQC}} + c_i^{\dot{\omega}_{33}^{\rm NQC}} \nu \text{ with } i = \{1,2\} \ . \tag{D129}$$

c. *Calculation of NQC quantities from the postpeak analytical waveform*

Let us finally discuss explicitly the computation of the NQC quantities $\left(A_{\ell m}^{\rm NQC}, \omega_{\ell m}^{\rm NQC}, \dot{A}_{\ell m}^{\rm NQC}, \dot{\omega}_{\ell m}^{\rm NQC}\right)$ from the NR-informed analytical description of the postpeak waveform, as defined in Sec. V A of [30], to which we refer the reader for the notation. Although the formulas have to be intended valid multipole by multipole, in the following we drop the (ℓ, m) indexes for clarity. The analytical expression for the amplitude and its time derivative read

TABLE XXX. Coefficients of the $(3,3)$ quantities needed to calculate the NQC extraction point. From left to right the columns show $\left\{\hat{A}_{33}^{\rm NQC}, \dot{A}_{33}^{\rm NQC}, \omega_{33}^{\rm NQC}, \dot{\omega}_{33}^{\rm NQC}\right\}$.

$\hat{A}_{33}^{\rm NQC}$			$\dot{A}_{33}^{\rm NQC}$			$\omega_{33}^{\rm NQC}$			$\dot{\omega}_{33}^{\rm NQC}$		
$\hat{A}_{33}^{\rm NQC_0}$	$=$	0.0512928	$\dot{A}_{33}^{\rm NQC_0}/\nu$	$=$	-3.9568×10^{-4}	$\omega_{33}^{\rm NQC_0}$	$=$	0.476647	$\dot{\omega}_{33}^{\rm NQC_0}$	$=$	0.0110394
$a_1^{\hat{A}_{33}^{\rm NQC}}$	$=$	0.09537	$a_1^{\dot{A}_{33}^{\rm NQC}}$	$=$	1.0985	$a_1^{\omega_{33}^{\rm NQC}}$	$=$	1.0886	$a_1^{\dot{\omega}_{33}^{\rm NQC}}$	$=$	2.7962
$a_2^{\hat{A}_{33}^{\rm NQC}}$	$=$	3.7217	$a_2^{\dot{A}_{33}^{\rm NQC}}$	$=$	-13.458	$a_2^{\omega_{33}^{\rm NQC}}$	$=$	3.0658			
$b_1^{\hat{A}_{33}^{\rm NQC_{\nu=0}}}$	$=$	0.00924494	$b_1^{\dot{A}_{33}^{\rm NQC_{\nu=0}}}$	$=$	1.41504×10^{-4}	$b_1^{\omega_{33}^{\rm NQC_{\nu=0}}}$	$=$	-0.236271	$b_1^{\dot{\omega}_{33}^{\rm NQC_{\nu=0}}}$	$=$	-4.5666×10^{-4}
$b_2^{\hat{A}_{33}^{\rm NQC_{\nu=0}}}$	$=$	-8.7052×10^{-5}	$b_2^{\dot{A}_{33}^{\rm NQC_{\nu=0}}}$	$=$	1.04680×10^{-4}	$b_2^{\omega_{33}^{\rm NQC_{\nu=0}}}$	$=$	-0.582892	$b_2^{\dot{\omega}_{33}^{\rm NQC_{\nu=0}}}$	$=$	-0.00388909
$b_3^{\hat{A}_{33}^{\rm NQC_{\nu=0}}}$	$=$	-0.479669	$b_3^{\dot{A}_{33}^{\rm NQC_{\nu=0}}}$	$=$	-0.422066						
$c_{11}^{\hat{A}_{33}^{\rm NQC}}$	$=$	0.0067063	$c_{21}^{\dot{A}_{33}^{\rm NQC}}$	$=$	-4.671176×10^{-4}	$c_1^{\omega_{33}^{\rm NQC}}$	$=$	-0.085544	$c_1^{\dot{\omega}_{33}^{\rm NQC}}$	$=$	0.0290846
$c_{12}^{\hat{A}_{33}^{\rm NQC}}$	$=$	4.814781	$c_{22}^{\dot{A}_{33}^{\rm NQC}}$	$=$	-4.0270198	$c_2^{\omega_{33}^{\rm NQC}}$	$=$	-0.523365	$c_2^{\dot{\omega}_{33}^{\rm NQC}}$	$=$	0.0087659
$c_{21}^{\hat{A}_{33}^{\rm NQC}}$	$=$	0.0111876	$d_0^{\dot{A}_{33}^{\rm NQC_{\nu=1/4}}}$	$=$	-0.090676						
$c_{22}^{\hat{A}_{33}^{\rm NQC}}$	$=$	-1.079532	$d_1^{\dot{A}_{33}^{\rm NQC_{\nu=1/4}}}$	$=$	-5.1643						
$c_{31}^{\hat{A}_{33}^{\rm NQC}}$	$=$	2.967227	$d_2^{\dot{A}_{33}^{\rm NQC_{\nu=1/4}}}$	$=$	-3.2594						
$c_{32}^{\hat{A}_{33}^{\rm NQC}}$	$=$	-2.571783									

$$A_h/\nu = e^{-\alpha_1 \frac{t-t_{\rm peak}}{M_{\rm BH}}}\left[c_1^A \tanh\left(c_2^A \frac{t-t_{\rm peak}}{M_{\rm BH}} + c_3^A\right) + c_4^A\right], \tag{D130}$$

$$\dot{A}_h/\nu = \frac{c_1^A c_2^A e^{-\alpha_1 \frac{t-t_{\rm peak}}{M_{\rm BH}}} \operatorname{sech}^2\left(c_2^A \frac{t-t_{\rm peak}}{M_{\rm BH}} + c_3^A\right)}{M_{\rm BH}} - \frac{\alpha_1 e^{-\alpha_1 \frac{t-t_{\rm peak}}{M_{\rm BH}}}\left[c_1^A \tanh\left(c_2^A \frac{t-t_{\rm peak}}{M_{\rm BH}} + c_3^A\right) + c_4^A\right]}{M_{\rm BH}}, \tag{D131}$$

while those for the phase and its derivatives read

$$\phi_h = -\omega_1 \frac{t-t_{\rm peak}}{M_{\rm BH}^2} - c_1^\phi \ln\left(\frac{1 + c_3^\phi e^{-c_2^\phi \frac{t-t_{\rm peak}}{M_{\rm BH}}} + c_4^\phi e^{-2c_2^\phi \frac{t-t_{\rm peak}}{M_{\rm BH}}}}{1 + c_3^\phi + c_4^\phi}\right), \tag{D132}$$

$$\omega_h = -\dot{\phi}_h = \frac{\omega_1}{M_{\rm BH}^2} - \frac{c_1^\phi c_2^\phi}{M_{\rm BH}} \frac{c_3^\phi x(t) + 2c_4^\phi x^2(t)}{1 + c_3^\phi x(t) + c_4^\phi x^2(t)}, \tag{D133}$$

$$\dot{\omega}_h = -\ddot{\phi}_h = \frac{c_1^\phi c_2^{\phi 2}}{M_{\rm BH}^2}\left[\frac{c_3^\phi x(t) + 4c_4^\phi x^2(t)}{1 + c_3^\phi x(t) + c_4^\phi x^2(t)} - \left(\frac{c_3^\phi x(t) + 2c_4^\phi x^2(t)}{1 + c_3^\phi x(t) + c_4^\phi x^2(t)}\right)^2\right], \tag{D134}$$

where we introduced

$$x(t) = e^{-c_2^\phi \frac{t-t_{\rm peak}}{M_{\rm BH}}}. \tag{D135}$$

The waveform quantities needed to compute the NQC correction to amplitude and phase are simply obtained by evaluating the above expressions at $t = t_{\ell m}^{\rm NQC} = t_{\ell m}^{\rm peak} + 2$ multipole by multipole.

d. The fitted derivative of the $(\ell, m) = (4, 4)$ amplitude at the NQC extraction point

Unfortunately, we have realized that the accuracy of the derivative obtained with the above template does not always have sufficient accuracy. This is due to insufficient flexibility of the fitting template, that will be modified in future work. To overcome this difficulty, we give here an explicit fit of the amplitude time-derivative that is then used in the main text. The derivative of NQC amplitude is separated in two terms as

$$\dot{A}_{44}^{\rm NQC} = \nu \dot{A}_{44}^{\rm NQC_0} \hat{\dot{A}}_{44}^{\rm orb}(\nu) + \hat{\dot{A}}_{44}^{\rm Spin}(\hat{S}, \nu)\ , \tag{D136}$$

TABLE XXXI. Explicit coefficients of the fit of $\dot{A}_{44}^{\rm NQC}$.

$\dot{A}_{44}^{\rm NQC_0}$	=	-1.52614×10^{-4}
$a_1^{\dot{A}_{44}^{\rm NQC}}$	=	-7.63783
$a_2^{\dot{A}_{44}^{\rm NQC}}$	=	15.8089
$a_3^{\dot{A}_{44}^{\rm NQC}}$	=	-5.88951
$a_4^{\dot{A}_{44}^{\rm NQC}}$	=	11.1555
$b_1^{\dot{A}_{44}^{\rm NQC}}$	=	3.76236×10^{-5}
$b_2^{\dot{A}_{44}^{\rm NQC}}$	=	-0.819379
$c_{11}^{\dot{A}_{44}^{\rm NQC}}$	=	-6.45958×10^{-6}
$c_{12}^{\dot{A}_{44}^{\rm NQC}}$	=	-2.35613
$c_{21}^{\dot{A}_{44}^{\rm NQC}}$	=	-298.678
$c_{22}^{\dot{A}_{44}^{\rm NQC}}$	=	-1063.08

where $\dot{A}_{44}^{\rm NQC_0}$ is the peak amplitude in the test particle limit. The non-spinning behavior is modeled with

$$\hat{\dot{A}}_{44}^{\rm orb}(\nu) = \frac{1 + a_1^{\dot{A}_{44}^{\rm NQC}}\nu + a_2^{\dot{A}_{44}^{\rm NQC}}\nu^2}{1 + a_3^{\dot{A}_{44}^{\rm NQC}}\nu + a_4^{\dot{A}_{44}^{\rm NQC}}\nu^2} \ . \tag{D137}$$

The spin dependence is first fitted to the test-particle limit using

$$\hat{\dot{A}}_{44}^{\rm Spin}(\hat{S}, \nu = 0) = \frac{b_1^{\dot{A}_{44}^{\rm NQC}}\hat{S}}{1 + b_2^{\dot{A}_{44}^{\rm NQC}}\hat{S}} \ , \tag{D138}$$

and then extrapolated to the comparable mass region through

$$b_1^{\dot{A}_{44}^{\rm NQC}} \to \frac{b_1^{\dot{A}_{44}^{\rm NQC}} + c_{11}^{\dot{A}_{44}^{\rm NQC}}\nu}{1 + c_{12}^{\dot{A}_{44}^{\rm NQC}}\nu} \ , \tag{D139}$$

$$b_2^{\dot{A}_{44}^{\rm NQC}} \to \frac{b_2^{\dot{A}_{44}^{\rm NQC}} + c_{21}^{\dot{A}_{44}^{\rm NQC}}\nu}{1 + c_{22}^{\dot{A}_{44}^{\rm NQC}}\nu} \ . \tag{D140}$$

[1] J. Aasi *et al.* (LIGO Scientific), Class. Quant. Grav. **32**, 074001 (2015), arXiv:1411.4547 [gr-qc].
[2] F. Acernese *et al.* (VIRGO), Class. Quant. Grav. **32**, 024001 (2015), arXiv:1408.3978 [gr-qc].
[3] B. P. Abbott *et al.* (Virgo, LIGO Scientific), Phys. Rev. Lett. **116**, 061102 (2016), arXiv:1602.03837 [gr-qc].
[4] B. P. Abbott *et al.* (Virgo, LIGO Scientific), Phys. Rev. Lett. **116**, 241103 (2016), arXiv:1606.04855 [gr-qc].
[5] B. P. Abbott *et al.* (VIRGO, LIGO Scientific), Phys. Rev. Lett. **118**, 221101 (2017), arXiv:1706.01812 [gr-qc].
[6] B. P. Abbott *et al.* (Virgo, LIGO Scientific), Astrophys. J. **851**, L35 (2017), arXiv:1711.05578 [astro-ph.HE].
[7] B. P. Abbott *et al.* (Virgo, LIGO Scientific), Phys. Rev. Lett. **119**, 141101 (2017), arXiv:1709.09660 [gr-qc].
[8] B. P. Abbott *et al.* (LIGO Scientific, Virgo), (2018), arXiv:1811.12907 [astro-ph.HE].
[9] B. P. Abbott *et al.* (Virgo, LIGO Scientific), Phys. Rev. Lett. **119**, 161101 (2017), arXiv:1710.05832 [gr-qc].
[10] B. P. Abbott *et al.* (LIGO Scientific, Virgo), (2020), arXiv:2001.01761 [astro-ph.HE].
[11] R. O'Shaughnessy, B. Farr, E. Ochsner, H.-S. Cho, V. Raymond, C. Kim, and C.-H. Lee, Phys. Rev. **D89**, 102005 (2014), arXiv:1403.0544 [gr-qc].
[12] V. Varma and P. Ajith, Phys. Rev. **D96**, 124024 (2017), arXiv:1612.05608 [gr-qc].
[13] L. London, S. Khan, E. Fauchon-Jones, X. J. Forteza, M. Hannam, S. Husa, C. Kalaghatgi, F. Ohme, and F. Pannarale, Phys. Rev. Lett. **120**, 161102 (2018), arXiv:1708.00404 [gr-qc].
[14] A. K. Mehta, C. K. Mishra, V. Varma, and P. Ajith, Phys. Rev. **D96**, 124010 (2017), arXiv:1708.03501 [gr-qc].
[15] R. Cotesta, A. Buonanno, A. Bohé, A. Taracchini, I. Hinder, and S. Ossokine, Phys. Rev. **D98**, 084028 (2018), arXiv:1803.10701 [gr-qc].
[16] V. Varma, S. E. Field, M. A. Scheel, J. Blackman, L. E. Kidder, and H. P. Pfeiffer, Phys. Rev. **D99**, 064045 (2019), arXiv:1812.07865 [gr-qc].
[17] A. Buonanno and T. Damour, Phys. Rev. **D59**, 084006 (1999), arXiv:gr-qc/9811091.
[18] A. Buonanno and T. Damour, Phys. Rev. **D62**, 064015 (2000), arXiv:gr-qc/0001013.
[19] T. Damour, P. Jaranowski, and G. Schaefer, Phys. Rev. **D62**, 084011 (2000), arXiv:gr-qc/0005034 [gr-qc].
[20] T. Damour, Phys. Rev. **D64**, 124013 (2001), arXiv:gr-qc/0103018.
[21] T. Damour, P. Jaranowski, and G. Schäfer, Phys. Rev. **D91**, 084024 (2015), arXiv:1502.07245 [gr-qc].
[22] A. Bohé *et al.*, Phys. Rev. **D95**, 044028 (2017), arXiv:1611.03703 [gr-qc].
[23] S. Ossokine *et al.*, in preparation, 2019.
[24] A. Nagar *et al.*, Phys. Rev. **D98**, 104052 (2018), arXiv:1806.01772 [gr-qc].
[25] LIGO Scientific Collaboration, "LIGO Algorithm Library - LALSuite," free software (GPL) (2018).
[26] A. Nagar and P. Rettegno, Phys. Rev. **D99**, 021501 (2019), arXiv:1805.03891 [gr-qc].
[27] S. Akcay, S. Bernuzzi, F. Messina, A. Nagar, N. Ortiz, and P. Rettegno, Phys. Rev. **D99**, 044051 (2019), arXiv:1812.02744 [gr-qc].
[28] A. Nagar, F. Messina, P. Rettegno, D. Bini, T. Damour, A. Geralico, S. Akcay, and S. Bernuzzi, Phys. Rev. **D99**, 044007 (2019), arXiv:1812.07923 [gr-qc].
[29] P. Rettegno, F. Martinetti, A. Nagar, D. Bini, G. Riemenschneider, and T. Damour, (2019), arXiv:1911.10818 [gr-qc].
[30] A. Nagar, G. Pratten, G. Riemenschneider, and R. Gamba, (2019), arXiv:1904.09550 [gr-qc].

[31] A. Nagar and A. Shah, Phys. Rev. **D94**, 104017 (2016), arXiv:1606.00207 [gr-qc].

[32] F. Messina, A. Maldarella, and A. Nagar, Phys. Rev. **D97**, 084016 (2018), arXiv:1801.02366 [gr-qc].

[33] T. Damour and A. Nagar, Phys.Rev. **D90**, 044018 (2014), arXiv:1406.6913 [gr-qc].

[34] A. Nagar, T. Damour, C. Reisswig, and D. Pollney, Phys. Rev. **D93**, 044046 (2016), arXiv:1506.08457 [gr-qc].

[35] T. Damour and A. Nagar, Phys.Rev. **D90**, 024054 (2014), arXiv:1406.0401 [gr-qc].

[36] W. Del Pozzo and A. Nagar, Phys. Rev. **D95**, 124034 (2017), arXiv:1606.03952 [gr-qc].

[37] A. Nagar, G. Riemenschneider, and G. Pratten, Phys. Rev. **D96**, 084045 (2017), arXiv:1703.06814 [gr-qc].

[38] T. Damour, B. R. Iyer, and A. Nagar, Phys. Rev. **D79**, 064004 (2009), arXiv:0811.2069 [gr-qc].

[39] Y. Pan, A. Buonanno, R. Fujita, E. Racine, and H. Tagoshi, Phys.Rev. **D83**, 064003 (2011), arXiv:1006.0431 [gr-qc].

[40] A. Nagar, F. Messina, C. Kavanagh, G. Lukes-Gerakopoulos, N. Warburton, S. Bernuzzi, and E. Harms, Phys. Rev. **D100**, 104056 (2019), arXiv:1907.12233 [gr-qc].

[41] T. Damour, A. Nagar, and S. Bernuzzi, Phys.Rev. **D87**, 084035 (2013), arXiv:1212.4357 [gr-qc].

[42] R. Fujita, PTEP **2015**, 033E01 (2015), arXiv:1412.5689 [gr-qc].

[43] D. Shoemaker, https://dcc.ligo.org/cgi-bin/DocDB/ShowDocument?docid=2974.

[44] A. Taracchini, A. Buonanno, G. Khanna, and S. A. Hughes, Phys.Rev. **D90**, 084025 (2014), arXiv:1404.1819 [gr-qc].

[45] E. Harms, S. Bernuzzi, A. Nagar, and A. Zenginoglu, Class.Quant.Grav. **31**, 245004 (2014), arXiv:1406.5983 [gr-qc].

[46] L. T. Buchman, H. P. Pfeiffer, M. A. Scheel, and B. Szilagyi, Phys. Rev. **D86**, 084033 (2012), arXiv:1206.3015 [gr-qc].

[47] T. Chu, H. P. Pfeiffer, and M. A. Scheel, Phys. Rev. **D80**, 124051 (2009), arXiv:0909.1313 [gr-qc].

[48] D. A. Hemberger, G. Lovelace, T. J. Loredo, L. E. Kidder, M. A. Scheel, B. Szilágyi, N. W. Taylor, and S. A. Teukolsky, Phys. Rev. **D88**, 064014 (2013), arXiv:1305.5991 [gr-qc].

[49] M. A. Scheel, M. Giesler, D. A. Hemberger, G. Lovelace, K. Kuper, M. Boyle, B. Szilágyi, and L. E. Kidder, Class. Quant. Grav. **32**, 105009 (2015), arXiv:1412.1803 [gr-qc].

[50] J. Blackman, S. E. Field, C. R. Galley, B. Szilágyi, M. A. Scheel, M. Tiglio, and D. A. Hemberger, Phys. Rev. Lett. **115**, 121102 (2015), arXiv:1502.07758 [gr-qc].

[51] G. Lovelace, M. Boyle, M. A. Scheel, and B. Szilagyi, Class. Quant. Grav. **29**, 045003 (2012), arXiv:1110.2229 [gr-qc].

[52] G. Lovelace, M. Scheel, and B. Szilagyi, Phys.Rev. **D83**, 024010 (2011), arXiv:1010.2777 [gr-qc].

[53] G. Lovelace *et al.*, Class. Quant. Grav. **32**, 065007 (2015), arXiv:1411.7297 [gr-qc].

[54] A. H. Mroue, M. A. Scheel, B. Szilagyi, H. P. Pfeiffer, M. Boyle, *et al.*, Phys.Rev.Lett. **111**, 241104 (2013), arXiv:1304.6077 [gr-qc].

[55] P. Kumar, K. Barkett, S. Bhagwat, N. Afshari, D. A. Brown, G. Lovelace, M. A. Scheel, and B. Szilágyi, Phys. Rev. **D92**, 102001 (2015), arXiv:1507.00103 [gr-qc].

[56] T. Chu, H. Fong, P. Kumar, H. P. Pfeiffer, M. Boyle, D. A. Hemberger, L. E. Kidder, M. A. Scheel, and B. Szilagyi, Class. Quant. Grav. **33**, 165001 (2016), arXiv:1512.06800 [gr-qc].

[57] S. Husa, S. Khan, M. Hannam, M. Pürrer, F. Ohme, X. Jiménez Forteza, and A. Bohé, Phys. Rev. **D93**, 044006 (2016), arXiv:1508.07250 [gr-qc].

[58] S. Khan, S. Husa, M. Hannam, F. Ohme, M. Pürrer, X. Jiménez Forteza, and A. Bohé, Phys. Rev. **D93**, 044007 (2016), arXiv:1508.07253 [gr-qc].

[59] D. Keitel *et al.*, Phys. Rev. **D96**, 024006 (2017), arXiv:1612.09566 [gr-qc].

[60] X. Jiménez-Forteza, D. Keitel, S. Husa, M. Hannam, S. Khan, and M. Pürrer, Phys. Rev. **D95**, 064024 (2017), arXiv:1611.00332 [gr-qc].